Dissertation
submitted to the
Combined Faculties for the Natural Sciences and for
Mathematics
of the Ruperto-Carola University of
Heidelberg, Germany
for the degree of
Doctor of Natural Sciences

presented by
Diplom-Physiker **Peter Daniel Witte**
born in Stuttgart

Oral examination: 16.10.2002

An Electron Target for
Collision Experiments with Trapped Ions

Zusammenfassung

Ein Elektronentarget für Stoßexperimente mit gespeicherten Ionen

Im Rahmen dieser Arbeit wurde ein Experiment zur Untersuchung von Elektronenstößen mit gespeicherten Molekülionen aufgebaut. Hierzu wird ein in einer Falle zwischen elektrostatischen Spiegeln gespeicherter Ionenstrahl mit einer kinetischen Energie von einigen keV im rechten Winkel mit einem niederenergetischen (5-50 eV) Elektronenstrahl gekreuzt. Damit kann zum einen eine Relaxation der inneren Anregungen der Molekülionen als auch ein effizienter Fragmentnachweis gewährleistet werden. Ein weiterer Vorteil des Experimentes besteht darin, daß für die Ionenspeicherung sowie für die Erzeugung und Führung des Elektronenstrahls ausschließlich elektrostatische Felder benutzt werden. Daher besteht keine Beschränkung hinsichtlich der Masse der gespeicherten Ionen. Experimente an schweren Clustern werden zugänglich.
Ausgehend von Simulationsberechnungen wurde ein Elektronentarget zur Erzeugung des erforderlichen Elektronenstrahls gefertigt, welches nach ersten Testmessungen in eine bestehende Ionenfalle am Weizmann Institute of Science eingebaut wurde. Nach Inbetriebnahme und Funktionstests wurden erste Messungen von Elektronenstößen an positiven (Ar^+ und CO^+) sowie negative Ionen (C^-, B^- und C_2^-) vorgenommen, welche die Funktionsfähigkeit dieses neuartigen Experiments belegen.

Abstract

An Electron Target for Collision Experiment with Trapped Ions

An experiment to study electron collisions on stored molecular ions has been built within the framework of this thesis. Ions are stored in a trap with a kinetic energy of several keV between two electrostatic mirrors. The stored ions are crossed at right angle by the low-energy (5-50 eV) electron beam. With this setup, both a relaxation of internal excitation of the molecular ion and an efficient detection of fragments can be achieved. An additional advantage is that the ion trapping field as well as the electron guiding field are electrostatic only, and thus no limitation on the mass of the stored ion is imposed. Experiments on very heavy clusters become accessible.
Based on simulations, an electron target was designed and constructed to provide the necessary electron beam. Upon first test measurements, the electron target was installed into an existing ion trap at the Weizmann Institute of Science. After commissioning and functioning tests, first measurements on electron collision processes were performed for positive (Ar^+ und CO^+) and negative ions (C^-, B^- and C_2^-) that show the operativeness of this new experimental approach.

To Susann

Contents

Chapter 1

Introduction

Ion trapping techniques have long been used to study gas-phase collisions of atomic and molecular particles. The general interest in these processes is motivated by the prominent role of these collisions in various types of plasma environments. Conditions in both naturally occurring and man-made plasmas span a wide range of parameters, from very cold (10K) interstellar clouds to extremely hot ($> 10^6$ K) regions in interstellar atmospheres and fusion devices.

Experimentally probing collision processes contributes not only to the better understanding of plasma environments but also to the fundamental physical concepts behind the dynamics of these reactions.

Trapping and storing of ions provides the basis for experimental studies. During storage, the ensemble can be prepared with known initial states by, for example, allowing for radiative relaxation to the vibrational ground state.

Early experiments on electron-ion collisions used Penning traps [1], where the ions are confined by a static electric quadrupole field in combination with a strong magnetic field. Collisions are induced by guiding an electron beam through the end caps of the trap and along the magnetic field lines onto the trapped ion cloud. Collisions are indirectly detected as an additional loss of trapped ions.

The experimental situation has improved significantly with the application of storage rings to atomic and molecular physics [2, 3, 4]. Direct detection of products has become possible due to the directionality and high kinetic energy of the stored ions. By merging the ion beam collinearly with an electron of the same velocity, very low relative kinetic energies between ion and electron can be achieved at high electron densities and very good energy resolution. These are necessary to reproduce the conditions for dissociative recombination in astrophysical plasmas.

One drawback of the storage rings are the practical limits on the charge-to-mass ratio of the ion imposed by the bending magnets. Heavy molecules can only be stored with very small velocities, increasing ionisation losses and decreasing storage lifetimes.

Electrostatic ion beam traps combine advantages of the two approaches mentioned. Easy detection of reaction products is preserved by the directionality of the ion beam while being a relatively small 'table-top' device. Without magnetic fields used for storing, these devices can be used to store ions of any mass. Due to the low velocities of

the ions in these devices it is extremely difficult to provide a collinear electron beam with the same velocities. Therefore, a crossed electron beam is used that can probe collisions with several eV impact energy.

The goal of this thesis is to present a new tool for electron-ion collision studies by introducing an electron target into an electrostatic ion trap. It will complement storage ring techniques on the heavy molecule side, while it cannot compete on experiments with very small relative energies. An overlap is given with collisions between light molecules and electrons at several eV energies.
In this respect, this work escorts the experiments from the design of the electron target to the installation and test of the electron-ion collision setup with simple, well-known processes. Dissociative excitation or electron detachment cross sections from storage rings can be used to benchmark and establish this approach.
A perspective not yet realised in this thesis is given by experiments on stored, heavy molecules, till now only accessible with single-pass cross beam experiments on hot molecules. Internal excitation can have significant influence on measured cross sections, so for a detailed understanding, well-defined initial conditions are required.

In chapter 2 an introduction to electron-ion interactions is given. Together with a presentation of the electrostatic trap in chapter 3 this sets the basis for the work on the electron beam in chapter 4. The simulation and implementation of the electron target as well as test results are discussed. In chapter 5 the trap installation of the electron target is explained and first observations of the interplay between electron beam and trap documented. First preliminary results on electron-ion interactions are shown for the case of C_2^-. This work concludes with some summarising remarks and an outlook on the perspective of this new tool.
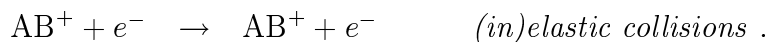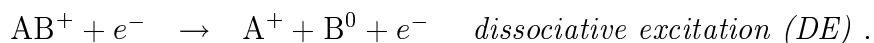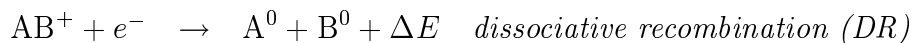
Chapter 2

Electron-Ion Interactions

The fundamental idea for the experimental setup developed within the frame of this work is to probe electron-ion collision processes at energies of about 5 to 50 eV. The approach to use electrostatic ion beam traps closes a gap between storage ring techniques and conventional single-pass or crossed beams experiments. Heavy molecules cannot be stored in magnetic storage rings, whereas in single-pass experiments usually only hot molecules can be studied. To benefit from the advantages of the approach used here, experiments are directed towards heavy molecules.

To set the field for this work and outline possible goals, an introduction to collision processes is given in this chapter. Experimental techniques to achieve these goals are discussed and some important properties introduced.

2.1 Electron collisions with molecular cations

Possible electron-induced collision reactions involving a molecular ion AB^+ can be written as:

$$AB^+ + e^- \quad \rightarrow \quad A^0 + B^0 + \Delta E \quad \textit{dissociative recombination (DR)}$$

$$AB^+ + e^- \quad \rightarrow \quad A^+ + B^0 + e^- \quad \textit{dissociative excitation (DE)} .$$

$$AB^+ + e^- \quad \rightarrow \quad AB^+ + e^- \quad \textit{(in)elastic collisions} .$$

Dissociative recombination (DR) is a process in which a positive molecular ion recombines with an electron and dissociates. The arising neutral fragments may be excited and carry kinetic energy. Dissociative excitation (DE) is a process where an incoming electron excites and dissociates the molecular ion without bing bound to any of the fragments. Pure elastic collisions are generally not of interest as they do not provide information about the internal states and excitation of the ion. Inelastic collisions however vibrationally excite the ion and its interplay with other reaction pathways provides information about the dynamics of the ion.

The reaction processes are well studied so far only for small molecules. As an example
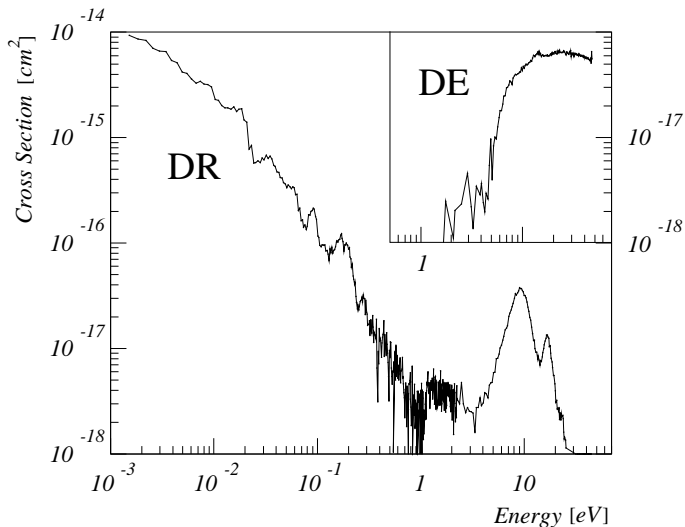
Figure 2.1: *Measurements at the TSR in Heidelberg on electron collisions with HD$^+$ [5]. Cross sections of dissociative recombination (HD$^+$ + e^- → H^0 + D^0) and dissociative excitation (HD$^+$ + e^- → H$^+$ + D^0 + e^-, see inlay).*

for a measurement of electron induced processes, cross sections derived for HD$^+$ are shown in figure 2.1.

Dissociative recombination cross sections are typically decreasing with collision energy. Some resonant features exhibit at energies of a few eV. Cross sections for dissociative excitation generally have onsets at typically a few to tens of eV.

An overview of electron-ion collisions is schematically given in figure 2.2. In the following sections, these processes are discussed in more detail.

2.1.1 Dissociative recombination

Dissociative recombination of a molecular ion AB$^+$ can be written as
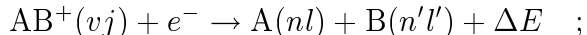
$$AB^+(vj) + e^- \rightarrow A(nl) + B(n'l') + \Delta E \quad ;$$

vj is the initial ro-vibrational state of the molecular ion and nl and $n'l'$ denote the states of the fragments A and B respectively. ΔE is the kinetic energy release, the total kinetic energy carried away by the fragments.

Depending on the electronic configuration of the molecule, two different mechanisms account for dissociative recombination: For molecules that exhibit a curve crossing of a doubly excited electronic state of the neutral molecule with the ground state of the molecular ion, two different paths in the 'crossing mode' can be effective: direct DR, in which an electron is captured into a doubly excited neutral state (di-electronic recombination). Stabilisation by dissociation concludes this purely electronic process. In indirect DR, the incident electron gets captured into an intermediate state (a vibrationally excited state of the neutral Rydberg states) which is then predissociated by the
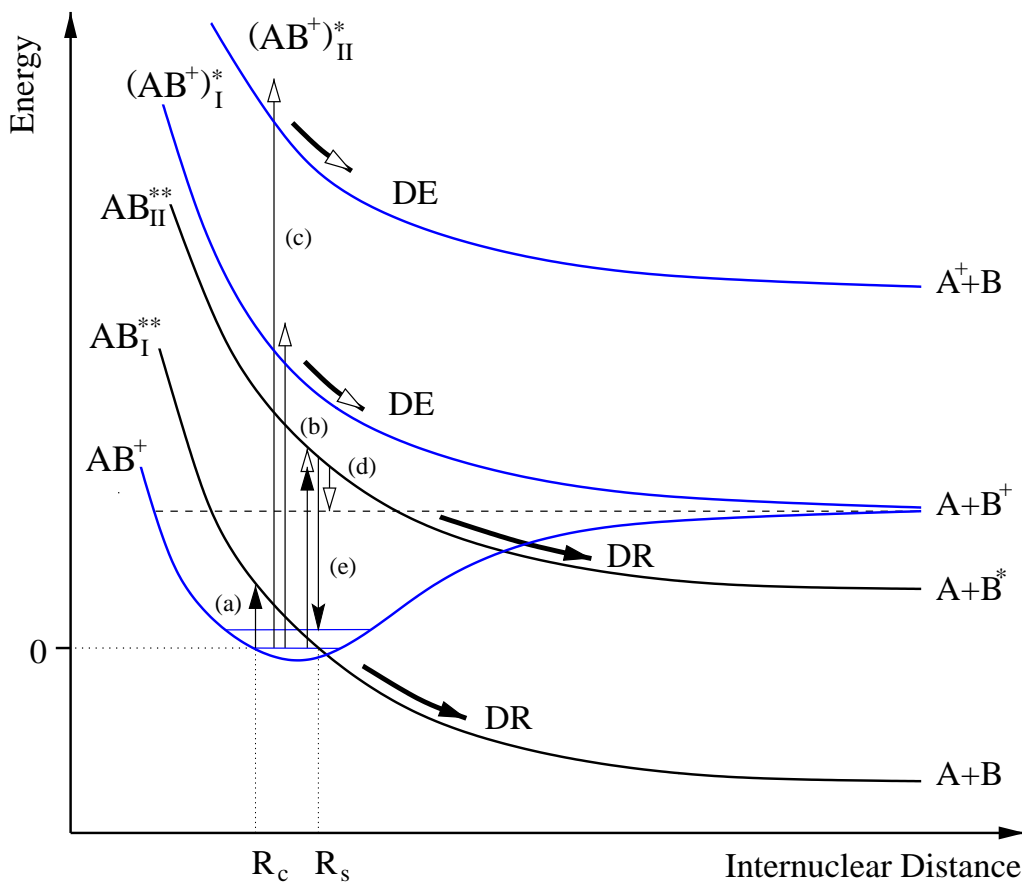
Figure 2.2: *Schematic diagram of potential energy curves for a molecule AB. Overview of direct dissociative recombination (DR, solid arrows) and dissociative excitation (DE, open arrows) processes. An example of an inelastic collision (arrow [e]) is also drawn.*

doubly excited state. This non-Born-Oppenheimer process is resonant because of the discrete energy levels of the intermediate state and competes with the direct process. For molecules without favourable curve-crossing , the DR mechanism in the 'tunneling mode' is explained by a nonadiabatic coupling to one of the neutral Rydberg states at short internuclear distances. For an overview of DR, many aspects are discussed in [6, 7].

DR with curve crossing - the direct mechanism

This process proceeds in two steps, electron capture and stabilisation by dissociation [8]:

$$\mathrm{AB}^+ + e^- \rightarrow \mathrm{AB}^{**} \rightarrow \mathrm{A} + \mathrm{B} + \Delta E \quad .$$
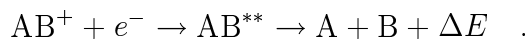
The incident electron excites the ion and is captured in an unoccupied molecular orbital, forming a neutral molecule in a doubly excited repulsive state (arrow [a] in figure 2.2 denotes this transition to the repulsive state $\mathrm{AB}_{\mathrm{I}}^{**}$). To stabilise, the molecule can

either dissociate (leading to DR) or autoionise. Autoionisation, the reverse electron capture process, requires good Franck-Condon overlap of the neutral molecule with energetically accessible vibrational states of the molecular ion. If the molecule survives autoionisation, it has to dissociate.

A classical approach to DR in the configuration interaction picture was given by Bardsley and Biondi [9]. A few considerations and results will be quoted in a brief review to complete this discussion.

Following the two-step nature of the process, the cross section for direct DR is given by

$$\sigma(E) = \sigma_c(E) \cdot P_S(E) \quad .$$

E is the center of mass energy, σ_c the cross section describing the electron capture into the repulsive state, and $P_S(E)$ the probability for this state to dissociate, called the survival factor. This assumption cannot fully be justified, but is useful for a qualitative description of the process [9].

Assuming a classical trajectory $R(t)$ for the dissociating nuclei and using a local autoionisation width $\Gamma(R)$, the survival factor can be written as

$$P_S(E) = \exp\left(-\int \frac{\Gamma(R(t))}{\hbar} dt \right)$$

The integral is evaluated between $t = 0$, when the electron capture occurs at internuclear distance R_c, and the time when the internuclear distance reaches the stabilisation point R_s (see figure 2.2). Here the repulsive capture state goes below the ionic ground state, making autoionisation energetically impossible. It is also clear that with this assumption this expression is only valid for low energies where the autoionisation can only lead to the vibrational ground state of the ion. With increasing energy, additional vibrational states of the molecular ion become energetically accessible from the repulsive AB** state and a more sophisticated expression for the survival factor must exhibit a stepwise decrease [10].

The capture cross section σ_c depends on the capture width $\Gamma_c(R_c)$, the probability of finding the initial ion with this internuclear distance R_c, given by the square of the nuclear wave function $\zeta_i(R_c)$ and also the slope of the final potential energy curve:

$$\sigma_c(E) = \frac{\pi^2 \hbar^2}{2m_e E} \left(\frac{g_n}{g_i} \right) \cdot \Gamma_c \cdot |\zeta_i(R_c)|^2 \cdot \left| \frac{dV_n}{dR} \right|_{R_c}^{-1}$$

g_i and g_n are the multiplicities of the electronic state of the molecular ion and neutral molecule, respectively.

At low energies, when all other factors can be assumed to be nearly constant, the cross section for the direct mechanism scales as

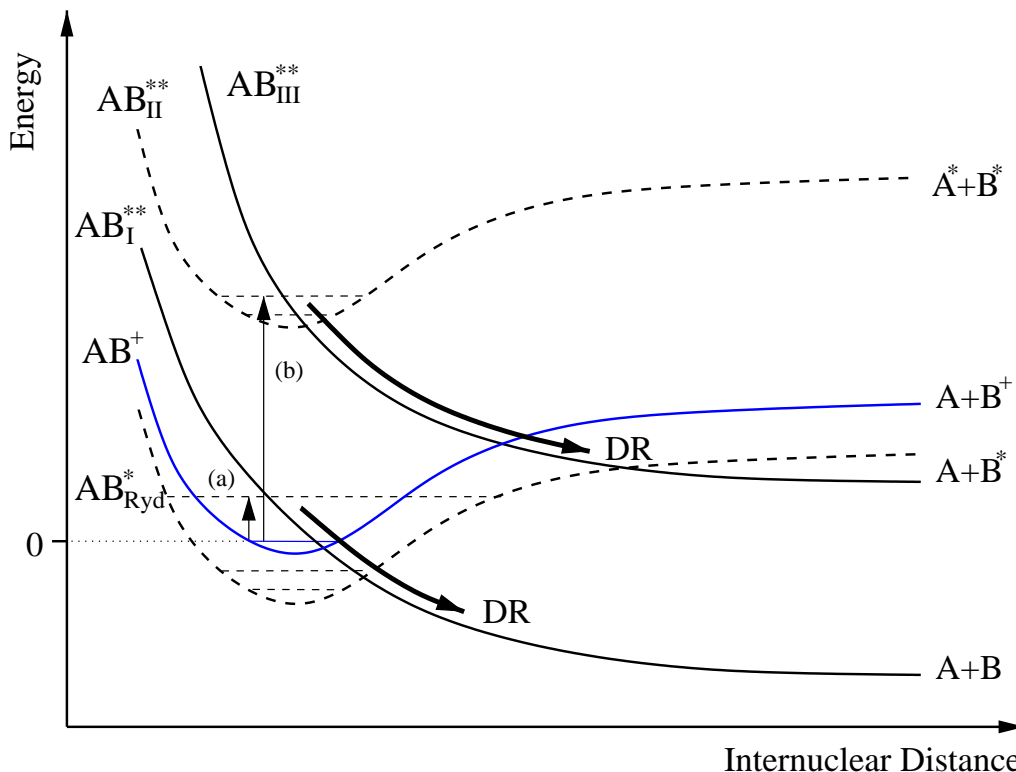$$\sigma(E) \propto E^{-1} \quad .$$

8

Figure 2.3: *Overview of indirect dissociative recombination.*

DR with curve crossing - the indirect mechanism

In contrast to the direct mechanism, the indirect or Rydberg mechanism goes beyond the Born-Oppenheimer (BO) approximation [11]. It is a resonant three step process and can be depicted as

$$AB^+ + e^- \rightarrow AB^*_{Ryd} \rightarrow AB^{**} \rightarrow A + B + \Delta E \quad .$$
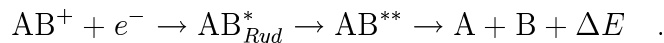
The incident electron does not lead to an excitation of an inner electron of the ion as in direct DR but instead excites the ion core vibrationally in the capture process. This constitutes a breakdown of the BO approximation. The electron is captured into a vibrationally excited Rydberg state of the neutral molecule AB^*_{Ryd} (arrow [a] in figure 2.3). This state, belonging to a series of Rydberg states converging to the ionic state AB^+, serves as an intermediate state, which is then predissociated by a repulsive doubly excited state. Again, as in the direct mechanism, dissociation competes with autoionisation.

Due to the discrete energy spectra of the intermediate Rydberg states, indirect DR is a resonant process and can interfere with direct DR constructively as well as destructively, leading to narrow, so-called window resonances in the DR cross section.

Thus, and ignoring the influence of the direct mechanism, the cross section for indirect DR can be written as a Breit-Wigner type of cross section, adding over all possible

intermediate resonance states s [12]:

$$\sigma(E) = \sum_s \frac{\pi\hbar^2}{2m_e E} \left(\frac{g_s}{2}\right) \frac{\Gamma_{sa}\Gamma_{sd}}{(E - E_s)^2 + \frac{1}{4}\Gamma_s^2}$$

Γ_{sa} and Γ_{sd} are the partial widths against decay by autoionisation and predissociation, respectively, Γ_s is the total width. E_s is the energy of the intermediate state and g_s its multiplicity.

Because this cross section scales in the limit of small Γ_s as

$$\sigma(E) \propto E^{-3} \quad,$$

this mechanism can cause deviation from the E^{-1} scaling expected from the direct mechanism at low energies.

Although for the indirect mechanism a change in nuclear configuration is involved, this path can be as efficient as direct DR. Only a single-electron radiationless transition is involved, whereas in the case of direct DR, a two-electron radiationless transition to the doubly excited neutral state is needed.

The indirect mechanism is of great importance for the DR of HD$^+$ at low energies [13].

DR without curve crossing

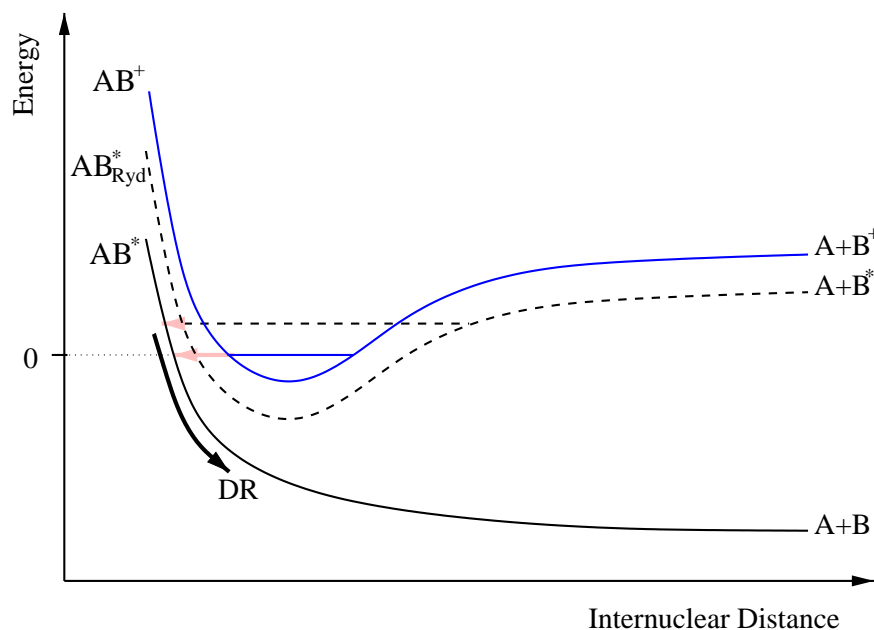Figure 2.4: *Dissociative recombination without curve crossing: Schematic diagram of potential energy curves for a molecule AB.*

As the examples of H$_3^+$ [14] HeH$^+$ [15] and LiH$^+$ [16] show, a favourable curve crossing is not necessary for an appreciable DR cross section. In the direct mechanism and

similarly for the indirect mechanism, the potential energy curve of the doubly excited repulsive state must cross the ionic potential energy curve between the classical turning points of the initial vibrational state.

Without this prerequisite, a tunneling mechanism assists in explaining the high DR cross section for the above mentioned molecular ions. This process can be written as

$$AB^+ + e^- \rightarrow AB^* \rightarrow A + B + \Delta E \quad .$$
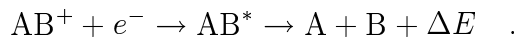
The molecular ion captures the incoming electron and simultaneously tunnels through the potential barrier to a repulsive ionic neutral state at short internuclear distances, see figure 2.4. This tunneling can proceed directly from the ionic ground state or indirectly via neutral Rydberg states.

Because of the tunneling mechanism, this type of DR is expected to be efficient only for hydrogen containing molecules as can be seen from an isotope effect in HeH^+ [17]. As in indirect DR, due to the involvement of only one single-electron radiationless transition despite the necessary change in nuclear configuration this DR mechanism can be very efficient.

DR at high electron energies

At higher collision energies between electron and molecular ion (typically more than 1 eV), the DR process proceeds through neutral Rydberg states belonging to excited ionic states. Similarly to the DR mechanisms described previously, a direct as well as an indirect process can exhibit.

In figures 2.2 and 2.3 the two mechanisms are shown (arrows [b]). In case the Rydberg state the electron is captured in (AB^{**}_{II}) is repulsive, direct DR can occur. Direct DR at high energy leads to broad resonances in the cross section. In case the capture state is a bound state it can be predissociated by a repulsive state (AB^{**}_{III}).

2.1.2 Dissociative excitation

Dissociative Excitation of a molecular ion AB^+ can be written as:
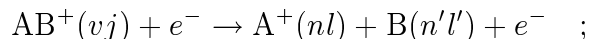
$$AB^+(vj) + e^- \rightarrow A^+(nl) + B(n'l') + e^- \quad ;$$

vj is the initial ro-vibrational state of the molecular ion and nl and $n'l'$ denote the states of the fragments A^+ and B respectively. Excess energy that is not transferred to either internal excitation or kinetic energy of the fragments is taken up by the free electron. DE is closely related to DR at high electron energies. A review of the DE process can be found in [20].

DE - the nonresonant mechanism

In the direct or nonresonant mechanism, a molecular ion is excited by a passing electron into a repulsive ionic state, which subsequently dissociates into one neutral and one

charged atomic fragment (arrow [c] in figure 2.2):

$$AB^+ + e^- \rightarrow (AB^+)^* \rightarrow A^+ + B + e^- \quad .$$
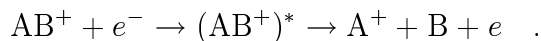
The threshold for this process is given by the vertical excitation energy to the first excited state of AB^+ in the Franck-Condon region. As the electron may carry away possible excess energy, this transition can occur at any internuclear separation for which the electron energy exceeds the excitation energy.

DE - the resonant mechanism

Even below the Franck-Condon threshold for nonresonant DE, another mechanism can contribute to this process. An electron is captured into a doubly excited neutral state which is (within the Franck-Condon region) located above the dissociation limit of AB^+, followed by autoionisation and dissociation:

$$AB^+ + e^- \rightarrow AB^{**} \rightarrow (AB^+)^* \rightarrow A^+ + B + e^- \quad .$$

Since the electron is captured into a bound orbital for which the electron energy must match, this process is resonant. In figure 2.2 a situation is shown where the neutral state (AB_{II}^{**}) autoionises to the vibrational continuum of the ionic ground state (arrow [d]).
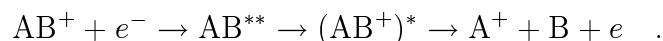This process is closely linked to the direct mechanism in DR. The only difference is whether or not the excited neutral molecule autoionises (leading to DE) or survives autoionisation (leading to DR). The cross section can therefore approximately be written as a product of the capture cross section with a factor P_{AI}, this time describing the probability to autoionise [9]

$$\sigma(E) = \sigma_c(E) \cdot P_{AI}(E) \quad ,$$

with $\sigma_c(E)$ the same expression as in 2.1.1. It has already been mentioned that the resonant mechanism can occur below the threshold of nonresonant DE. Above the threshold for nonresonant DE, the two mechanisms may interfere.

2.1.3   Superelastic and inelastic collisions

Both mechanisms, superelastic collisions (SEC) and inelastic collisions (IC) are related to DE. The processes can be written as

$$AB^+(v) + e^- \rightarrow AB^+(v') + e^- \quad .$$
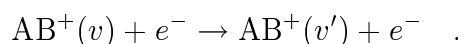
In contrast to the other processes mentioned so far, the molecular ion does not dissociate after the collision but is instead left in a different vibrational state with quantum number $v' < v$ for SEC and $v' > v$ for IC.
SECs form a way of vibrationally cooling stored molecule that do not possess a dipole moment. In this process, a direct vibrational excitation (IC) or de-excitation (SEC)

is needed. These processes are expected to be unimportant due to the usually small Franck-Condon overlap between vibrational states of the same principal quantum number n.

However, measured SEC rate coefficients for H_2 [22, 23] turned out to be much higher than predictions from calculation for the direct process [24]. In [25], an indirect process involving an intermediate neutral state AB^* is discussed:
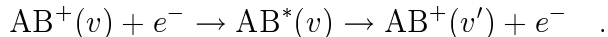
$$AB^+(v) + e^- \rightarrow AB^*(v) \rightarrow AB^+(v') + e^- \quad .$$

The cross section for this process may be written as a product of the capture cross section with a factor $P_{AI_{v'}}$ describing the probability of autoionisation to the initial electronic state, but to a different vibrational quantum number v', without dissociation. Within this model, the following equation holds

$$P_S + P_{AI} + \sum_{v'} P_{AI_{v'}} = 1 \quad \text{for any given electron energy} \quad E \quad ,$$

exemplifying the interplay between the different channels following electron capture: SEC or IC after autoionisation to vibrational levels of the initial electronic state, non-resonant DE after autoionisation to a repulsive ionic state and subsequent dissociation or direct DR after surviving autoionisation and subsequent dissociation.

2.2 Electron collisions with molecular anions

Electron-anion collisions are qualitatively different from electron scattering on neutral or positive molecules as the dominant break up reaction is not dissociation but electron detachment.

The possible reactions involving a molecular anion AB^- can be written as two processes involving detachment:

$$
\begin{array}{rcll}
AB^- + e^- & \rightarrow & AB^0 + 2e^- & \textit{detachment} \\
\\
AB^- + e^- & \rightarrow & A^0 + B^0 + 2e^- & \textit{detachment plus dissociation}
\end{array}
$$
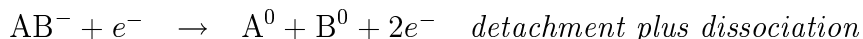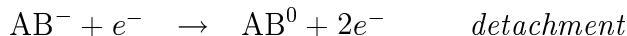
and two dissociative reactions:

$$
\begin{array}{rcll}
AB^- + e^- & \rightarrow & A^- + B^0 + e^- & \textit{dissociation} \\
\\
AB^- + e^- & \rightarrow & A^- + B^+ + 2e^- & \textit{dissociation plus ionisation} .
\end{array}
$$
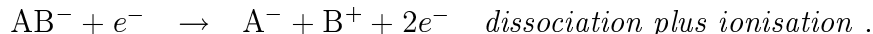
The formation of doubly charged anions (dianions) through electron bombardment and the role of dianionic resonances in electron-anion collisions is another topic of interest [26, 27, 28]. For a schematic overview of these processes see figure 2.5.
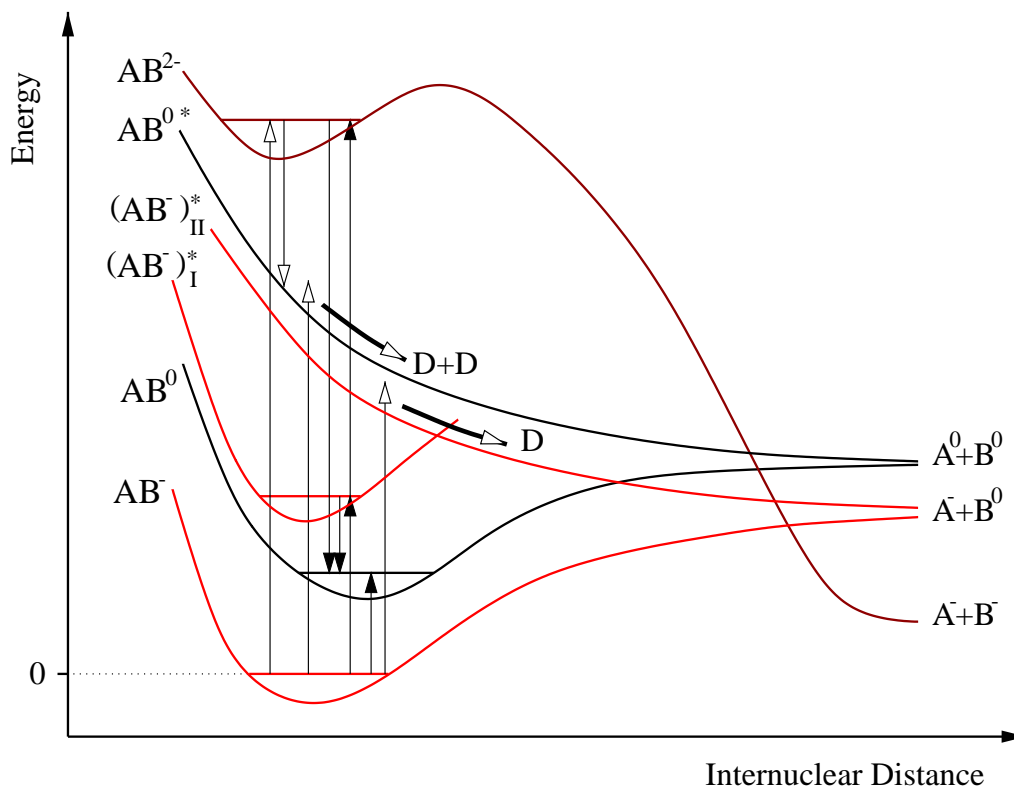
Figure 2.5: *Schematic diagram of potential energy curves for a molecule AB. Possible reaction pathways for detachment (solid arrows), dissociation and detachment plus dissociation (D and D+D, open arrows).*

2.2.1 Detachment

The nonresonant detachment process can proceed as either a one- or a two-step process:

$$\mathrm{AB}^-(vj) + e^- \rightarrow \mathrm{AB}^0(v'j') + 2e^-$$

and

$$\mathrm{AB}^-(vj) + e^- \rightarrow \mathrm{AB}^-(v''j'') + e^- \rightarrow \mathrm{AB}^0(v'j') + 2e^- \quad .$$
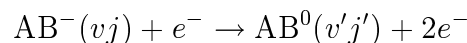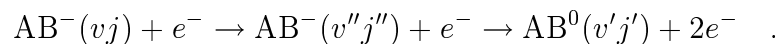
The two-step process proceeds through a resonant state of the anion. This is not expected to give rise to resonant structures in the cross-section however, as the first step, the excitation process, can happen at any incident electron energy above the excitation energy.

The final state of the neutral molecule, $\mathrm{AB}^0(v'j')$, or the intermediate state of the anion, $\mathrm{AB}^-(v''j'')$, may be in the dissociative continuum, resulting to detachment plus dissociation or pure dissociation.

In another type of possible process, the incoming electron is resonantly captured into a dianionic state. This subsequently decays either by simultaneous or sequential emission

of two electrons into a molecular bound state:

$$AB^-(vj) + e^- \rightarrow AB^{2-}(v''j'') \rightarrow AB^0(v'j') + 2e^- \quad .$$
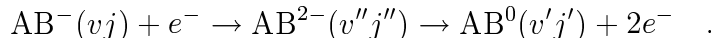
Again, the dianionic state can alternatively proceed via autodetachment to a repulsive molecular ion state, leading to dissociation.

Nonresonant electron detachment is the dominating process for all experimentally studied molecular and atomic systems. The detachment cross section is characterised by an effective threshold of two to three times the electron binding energy of the anion and a smooth energy dependence above threshold. The effective threshold reflects the Coulomb barrier the incoming electron has to overcome to release the bound electron. The similarity in behaviour close to threshold between atomic and molecular anions indicates that detachment proceeds through a similar mechanism for both types of systems.

Several theoretical descriptions explain atomic detachment in classical [29] (both electrons are describes classically), semi-classical [30]-[33] (the incoming electron is described classically and the bound electron quantum mechanically) and full quantum mechanical [34, 35] approximations.

In semi-classical approximations, an impact parameter formalism is used. The cross section is then written as

$$\sigma(E) = 2\pi \int_0^\infty P(E, \rho)\rho \, d\rho \quad ,$$

with ρ the impact parameter and $P(E)$ the reaction probability which is the subject of calculation.

The electron-electron interaction is expanded to first order (dipole approximation), and the reaction is described as an electric field detachment where the electric field is provided by the incoming electron.

All models formulate a condition for detachment that the available energy from the approaching electron must exceed the energetic threshold at some characteristic distance. The long-range Coulomb repulsion distorts the incoming electron and is important in accounting for the effective threshold and the cross section behaviour.

Reaction cross sections can be described in the threshold region below the cross section maximum by

$$\sigma(E) = \sigma_0(1 - \frac{E_{th}}{E}) \quad ,$$

with E_{th} the characteristic threshold energy.

2.2.2 Detachment plus dissociation

Similarities in the shape of the cross section for detachment plus dissociation and pure detachment suggest a similar mechanism for both reactions.

Possible reaction pathways closely linked to the ones given in the previous section are: A vertical transition to a dissociative state of the neutral molecule

$$AB^-(vj) + e^- \rightarrow AB^0(v'j') + 2e^- \quad \text{followed by}$$

$$\mathrm{AB}^0(v'j') \to A^0(nl) + B^0(n'l') + \Delta E$$
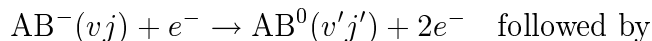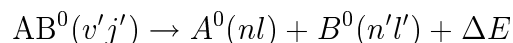
and alternatively, through a resonant state of the anion

$$\mathrm{AB}^-(vj) + e^- \to \mathrm{AB}^-(v''j'') + e^- \to A(nl) + B(n'l') + 2e^- + \Delta E \quad .$$
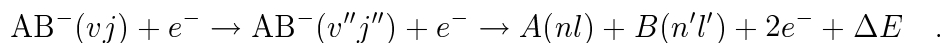
2.2.3 Dissociation

Nonresonant dissociation is likely to proceed through a dissociative state of the negative ion:

$$\mathrm{AB}^-(vj) + e^- \to \mathrm{AB}^-(v'j') + e^- \quad \text{followed by dissociation:}$$
$$\mathrm{AB}^-(v'j') \to \mathrm{A}^-(nl) + \mathrm{B}^0(n'l') + \Delta E$$

Cross sections involving dissociation (either leading to A + B or to A^- + B) are much smaller than for pure detachment, as the typical timescales for autodetachment ($\sim 10^{-15}$ to 10^{-17} s) are generally smaller than that for dissociation ($\sim 10^{-15}$ s).

The formation of a dianionic state can lead to a resonant structure superimposed on the dominating nonresonant background, when autodetachment of the dianion leads to a dissociative ionic state of the molecule. These intermediate states are theoretically and experimentally interesting, as they represent a state with an extreme amount of electron correlation. Atomic dianions are unstable [36] and small molecular dianions are normally unstable as well. The extra electro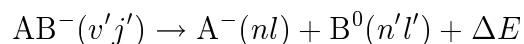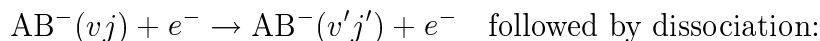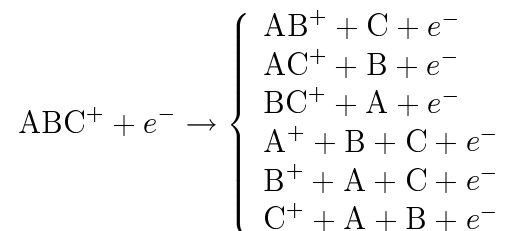n has to be confined in a rather small space; two electrons separated by 1.5 Å give a Coulomb energy of about 10 eV. Only large molecules and clusters are capable of binding two extra electrons.

2.3 Electron collisions with heavy molecules

Of special interest for experiments with the electrostatic trap described in this work are heavy molecules that cannot be stored in storage rings due to the limiting rigidity of the bending magnets. Although ideas for dedicated experiments have to develop in accordance with theoretical calculations, some possible fields of interest are exemplified in this section.

With polyatomic molecules the processes of electron-ion collisions are basically the same. There is, however, an additional degree of freedom related to the different branching ratios. For example, the triatomic molecule ABC^+ can proceed via the following channels in dissociative excitation:

$$\mathrm{ABC}^+ + e^- \to \begin{cases} \mathrm{AB}^+ + \mathrm{C} + e^- \\ \mathrm{AC}^+ + \mathrm{B} + e^- \\ \mathrm{BC}^+ + \mathrm{A} + e^- \\ \mathrm{A}^+ + \mathrm{B} + \mathrm{C} + e^- \\ \mathrm{B}^+ + \mathrm{A} + \mathrm{C} + e^- \\ \mathrm{C}^+ + \mathrm{A} + \mathrm{B} + e^- \end{cases}$$

As can be seen even such a simple system as ABC^+ can lead to a large number of possible reaction channels. The branching ratios of the different channels are related

to the ratios of the autoionisation along the different reaction pathway and also to the internal dynamics of the dissociation.

Clusters and fullerenes

Conglomerations of few (3 to 4) up to several thousand atoms or molecules are generally known as clusters. Owing to the exceptional chemical position of carbon as an element that can form single, double as well as triple bonds, carbon clusters exhibit in a large variety of geometrical structures. C_n molecules can form as chains, rings, and sheets, as well as spheroidal fullerenes [37, 38]. Fullerenes are carbon clusters C_n with exactly twelve pentagons and $\frac{n}{2} - 10$ hexagons.

Carbon clusters are believed to be important in the formation of soot in flames as well as in astrophysics where they might act as building blocks and appear as fragments of carbonaceous materials. Interstellar dust clouds and atmospheres surrounding carbon stars are natural environments where carbon clusters occur [39, 40]. Small carbon clusters are generally believed to be linear, with the transition to monocyclic rings at C_{10} [41]. There is a strong odd-even effect in linear chains, visible in physical properties most sensitive to the electronic states: electron affinity, ionisation potential and dissociation energy. This supports the alternation between singlet and triplet electronic states for odd- and even-numbered linear chains.

The onset of fullerene formation is generally linked to cluster stability which decreases up to $n = 29$ and then abruptly increases [42]. Large fullerenes C_n^{z+} close to $n = 60$ are known to dissociate by evaporation of C_2 for charge states $z \leq 4$ [43].

Interatomic bonds of Carbon clusters are strongly covalent in nature and thus their electron density distribution is structured. Metal clusters on the other hand have a very different electronic structure. Their properties can be described by the free electron model. These clusters thus represent a realisation of a many-electron problem in a spherical square-well potential. A comparison of metal clusters with carbon cluster therefore is of interest with respect to electron-cluster collisions and the role of charge localisation inside the cluster towards subsequent dissociation.

Biomolecules

An extreme regarding heavy molecules are biomolecules. In this section only a small excursion into this field is made with an example of the importance of electron collisions to these type of molecules.

The damaging effects of ionisation radiations in living cells are not caused by the mere direct impact of the primary high-energy quanta. Most of the energy deposited goes into the production of free secondary electrons with energies between 1 to 20 eV. Even at energies below the ionisation threshold, single- and double-strand breaks in DNA can occur [44]. In contrast to DNA strand breaks induced by photons with similar energy where above a certain threshold of typically a few eV hardly any energy dependence up to keV energies is found [45, 46], damage induced by electrons is highly dependent on the kinetic energy of the incident electron, showing resonant features.
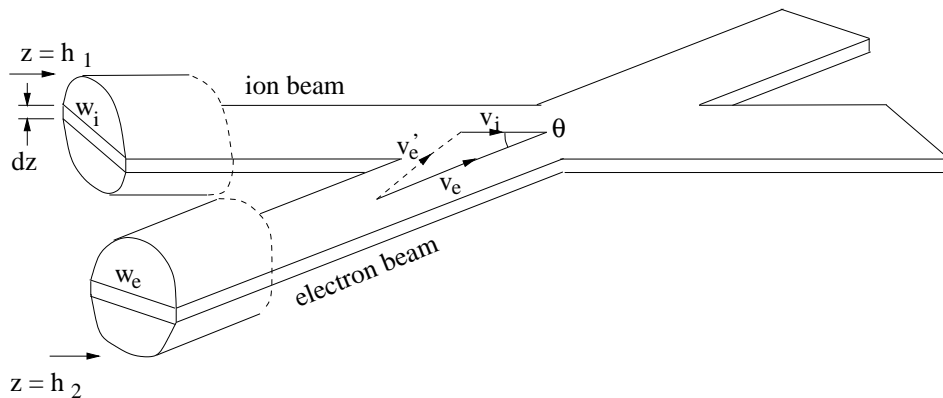
Figure 2.6: *Crossed electron and ion beams.*

It is believed that electron attachment occurs somewhere within the DNA molecule leading to a formation of a resonance state. This state can decay either by electron autodetachment or by dissociation along a certain specific bond. Some fragmentation products can subsequently react with other DNA components, leading to a double-strand break.

This shows the complexity and importance of electron induced processes and reaction dynamics in large molecules. If some of these problems can be tackled with trap devices remains to be seen.

2.4 Determination of collision cross sections

2.4.1 General crossed beams approach

Consider a monoenergetic beam of electrons with velocity v_e colliding with a parallel beam of monoenergetic ions, whose velocity is v_i. The angle of incidence is θ and the volume of interaction V_{int}. The collision rate $R(z)dz$ for single collisions in the element of height dz located at z is

$$R(z)dz = \sigma(E)\rho_e\rho_i v_e' V_{int} = \sigma(E)\rho_e\rho_i v_e' \frac{w_e(z)w_i(z)}{\sin\theta}dz \quad . \tag{2.1}$$

$\sigma(E)$ is the cross section at incident electron energy E corresponding to incident velocity v_e', given by

$$v_e' = \left(v_i^2 + v_e^2 - 2v_i v_e \cos\theta\right)^{1/2} \quad .$$

The electron and ion density, ρ_e and ρ_i, can be expressed in terms of electron and ion current,

$$i_e(z)dz = \rho_e e v_e w_e(z)dz \qquad \text{and} \qquad i_i(z)dz = \rho_i N e v_i w_i(z)dz \quad ,$$

which is passing through an element of height dz and width $w_e(z)$ and $w_i(z)$, respectively. Ne is the ion charge with e being the electronic charge. This leads to an

expression for the collision rate,

$$R(z)dz = \sigma(E)\frac{(v_i^2 + v_e^2 - 2v_iv_e\cos\theta)^{1/2}}{Ne^2v_ev_i\sin\theta}i_e(z)i_i(z)dz \quad . \tag{2.2}$$

The total collision rate R is given by integrating equation 2.1 between the spatial limits of the beams, denoted h_1 and h_2. For intersecting angle $\theta = 90$, the cross section becomes

$$\sigma(E) = Ne^2F\frac{v_iv_e}{(v_i^2 + v_e^2)^{1/2}}\frac{R}{I_iI_e} \quad . \tag{2.3}$$

Here, I_e and I_i denote the total current of ion and electron beams and F is the so-called form factor given by

$$F = \frac{\int_{h_1}^{h_2} i_e(z)dz \int_{h_1}^{h_2} i_i(z)dz}{\int_{h_1}^{h_2} i_ei_i(z)dz} \quad . \tag{2.4}$$

This factor describes the overlap of the two beams. Without knowledge of it, only relative cross sections can be measured. The conventional way of determining the form factor is to use slits, effectively evaluating the integrals by hand. This method is prone to errors because the introduction of the slits may cause focussing effects especially on the electron beam. Additional uncertainties arise from the geometrical arrangement of the shutter with respect to the plane of intersection. Another rather elegant method to overcome these problems is the animated-beam technique discussed later in this chapter.

Collision energy

To determine the collision energy in a collision of an electron with velocity $\vec{v_e}$ and an ion with velocity $\vec{v_i}$ one has to get the electron energy in the ion rest frame.
The electron velocity in the ion rest frame is given by:

$$\vec{v_e}' = \vec{v_e} - \vec{v_i} \quad ,$$

corresponding to an electron energy of

$$E_{coll} = E_e' = \frac{1}{2}m_ev_e'^2 = \frac{1}{2}m_e(v_e^2 + v_i^2 - 2v_ev_i\cos\theta) = E_e + \frac{m_e}{m_i}E_i - 2\sqrt{\frac{m_e}{m_i}}\sqrt{E_eE_i}\cos\theta \quad .$$

where θ is the angle between electron and ion in the lab frame. As $\theta = \frac{\pi}{2}$ in our case, this reduces to

$$E_{coll} = E_e + \frac{m_e}{m_i}E_i \quad . \tag{2.5}$$

In figure 2.7, the difference between collision energy and electron energy is plotted as a function of the ion mass at an ion beam energy of 4.2 keV, a value typically used for the trap experiments. For ions heavier than sodium, less than 0.1 eV has to be added to the electron beam energy to determine the correct collision energy.
Although the interaction electrode is grounded, the potential in the interaction region
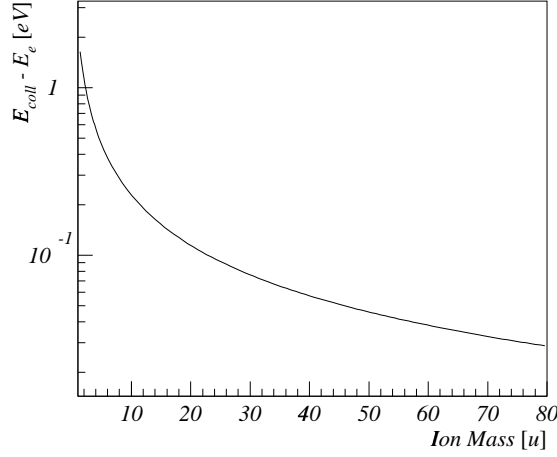
Figure 2.7: *Contribution from the ion motion at 4.2 keV kinetic energy to the collision energy; see equation 2.5.*

differs from ground due to the space charge of the beam and the influence of neighbouring electrodes. The magnitude of this effect can be taken from simulations, which will be presented in section 4.2.3.

The error on the collision energy is given by the Gauss equation for propagation of random error:

$$\Delta E_{coll}{}^2 = \left(\frac{\partial E_{coll}}{\partial E_e} \Delta E_e \right)^2 + \left(\frac{\partial E_{coll}}{\partial E_i} \Delta E_i \right)^2 + \left(\frac{\partial E_{coll}}{\partial E_\theta} \Delta \theta \right)^2 \quad ,$$

with

$$\Delta E(e) = \frac{\partial E_{coll}}{\partial E_e} \Delta E_e = \left[1 - \sqrt{\frac{m_e}{m_i}} \sqrt{\frac{E_i}{E_e}} \cos \theta \right] \Delta E_e \cong \Delta E_e \tag{2.6}$$

$$\Delta E(i) = \frac{\partial E_{coll}}{\partial E_i} \Delta E_i = \left[\frac{m_e}{m_i} - \sqrt{\frac{m_e}{m_i}} \sqrt{\frac{E_e}{E_i}} \cos \theta \right] \Delta E_i \cong \frac{m_e}{m_i} \Delta E_i \tag{2.7}$$

$$\Delta E(\theta) = \frac{\partial E_{coll}}{\partial E_\theta} \Delta \theta = \left[2\sqrt{\frac{m_e}{m_i}} \sqrt{E_i E_e} \sin \theta \right] \Delta \theta \cong \left[2\sqrt{\frac{m_e}{m_i}} \sqrt{E_i E_e} \right] \Delta \theta \quad . \tag{2.8}$$

These error contributions depend on the electron beam properties and are characteristics of the cathode and the electrode arrangement. A more detailed discussion of these points will also follow in section 4.2.3.

Not only the electron-ion collisions, but also collisions of the ions with restgas atoms can lead to products which are identical or give identical signatures in the detector. This background events need to be taken into account when determining a cross-section for a given reaction. Methods to deal with this are the subject of the next section.

2.4.2 Experimental techniques

Beam modulation

When measurements of electron-ion collisions are performed, care needs to be taken to account for the right background to be subtracted from the data. Background counts not associated with the actual collision process under study can have various origins. Although details of the trap and the detector location have not been mentioned so far, the current understanding of possible causes for various background events is already quoted for our distinctive apparatus.

- When neither electron nor ion beam are present, noise counts by detector or electronic noise can arise at a rate $R_{B,det}$.

- When only the ion beam is stored in the trap, background counts arise from neutrals created in collision with restgas atoms exiting the trap. This contribution is expected to be dependent on the restgas pressure and gives rise to the distinctive trapping lifetime of the ion beam. This is the dominating origin of detector counts at a rate $R_{B,i}$.

- When only the electron beam is present, electron-induced noise at a rate $R_{B,e}$ can arise on the detector, probably originating from highly accelerated electrons producing X-ray photons in the trap. See section 5.2.2 for more details on this.

- When both beams are present, apart from the desired signal counts at rate R_s, background counts may arise: The electron beam influences the vacuum by inducing desorption from surfaces hit by the electron beam. This in turn leads to an electron-induced contribution at a rate $R_{B,ei}$ on the pressure-dependent ion beam background.

To distinguish the signal from the background it is desirable to measure each contribution individually. In order to compare different situations conclusively, it is important to do these measurements within short times, as conditions influencing background rates may be subject to change. Beam modulation techniques are commonly applied in these circumstances [47].
The background contribution when both beams are present ($R_{B,ei}$) cannot easily be separated from the signal events which also require both beams. As this combined electron-ion background is arising from an increase in pressure with the electron beam present, an electron beam modulation fast enough to equilibrate pressure conditions can be used to reduce this background component.
In figure 2.8, the scheme employed in the experiments of this work is shown. The ion beam is injected into the trap where it is stored. It undergoes an exponential decay with a typical storage time of a few seconds. After some time the trap is opened and the beam released. Then, some time is waited to measure without an ion beam present before the next injection starts this cycle again. The electron beam is modulated all the time with a fixed frequency, not synchronised with the injection of the ion beam.
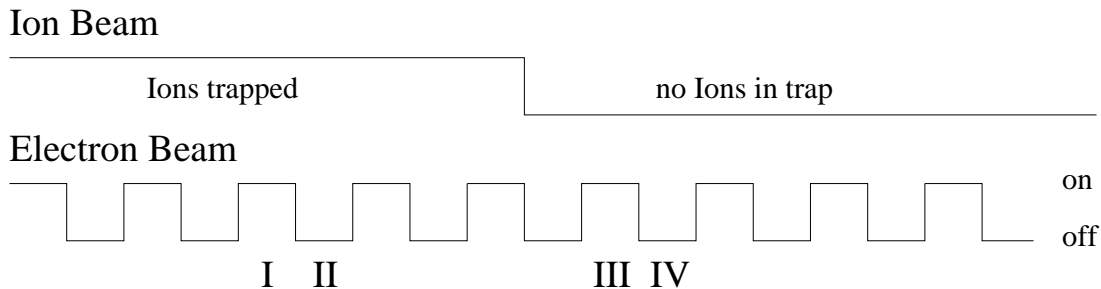
Ion Beam

Figure 2.8: *Modulation principle for trap experiments. One injection cycle is schematically shown. After some time of ion storage to determine the contribution of both beams (intervals I) and the ion beam alone (intervals II), the trap is opened to measure the contribution of electron beam (intervals III) and without any beam (intervals IV).*

This way each point in time after the injection is evenly sampled both with electron beam present and electron beam off.

Expected signal to background and sensitivity of measurements

The nature of the cross section measurement is a comparison between two processes giving rise to neutral rates on the MCP detector. It is therefore important to know in which ratio these rates appear and how this relates to the capabilities of the trap measurements. One can write the two rates in the form

$$R_s = \sigma_s \rho_i \rho_e v'_e V_{int,s}$$

for the signal rate and

$$R_b = \sigma_b \rho_i \rho_b v_i V_{int,b}$$

for the background rate due to restgas collisions. The rates are proportional to the cross section of the process σ, the target density ρ and the interaction volume V_{int}. A first estimate for the expected signal to background ratio can be obtained by determining

$$\frac{R_s}{R_b} = \frac{\sigma_s \rho_e v'_e V_{int,s}}{\sigma_b \rho_b v_i V_{int,b}} = \frac{\sigma_s \rho_e v_e l_e}{\sigma_b \rho_b v_i l_{tr}} \tag{2.9}$$

for typical values encountered in the trap. The background rate is governed by the restgas density of about $\rho_b = 3.2 \cdot 10^6 \text{cm}^{-3}$ at a typical trap pressure of 10^{-10} Torr and originates along the whole trap length l_{tr}. The incident velocity of the ions is in the 10^7cms^{-1} range, for C_2^- at 4200 keV kinetic energy $v_i = 1.5 \cdot 10^7 \text{cms}^{-1}$. For a 10 eV electron beam, the signal rate is proportional to the electron density of about $\rho_e = 4.5 \cdot 10^5 \text{cm}^{-3}$ and the incident velocity $v_e = 1.9 \cdot 10^8 \text{cms}^{-1}$. Neutrals giving rise to the signal rate only originate along the part where an overlap with the electron beam of width $l_e \approx 5$ cm is given. Assuming typical charge transfer reaction cross sections for

the background process of $\sigma_b = 1 \cdot 10^{-15} \text{cm}^2$ and a cross section for a signal producing process of $\sigma_s = 2 \cdot 10^{-16} \text{cm}^2$, the expected ratio becomes

$$\frac{R_s}{R_b} \approx 2.7 \cdot 10^{-2} \quad .$$

This ratio is dependent on the electron beam energy E, as both the electron velocity ($v_e \propto E^{1/2}$) and the electron density ($\rho_e \propto E$) are energy-dependent. With the values given above, and explicitly quoting the cross sections, it can be written as

$$\frac{R_s}{R_b} \approx \frac{\sigma_s}{\sigma_b} 4.2 \cdot 10^{-3} E^{3/2} \quad ; E \quad \text{in eV} \quad . \tag{2.10}$$

$\frac{R_s}{R_b}$ is measured in the trap as a ratio of detector counts originating from the signal and background processes. By summing these counts over the trapping time, large values of counts $N^{\Delta t}$ can be achieved. To assess the capabilities of these measurements, the sensitivity can be estimated. To differentiate a signal, the statistical error has to be smaller than the measured effect:

$$\frac{R_s}{R_b} > \Delta \left(\frac{R_s}{R_b} \right) \sim \frac{1}{\sqrt{N^{\Delta t}}} \quad .$$

Practical limitations regarding measurement times restrict this method from becoming infinitely sensitive. In a run with 500 injection of 2 s each typically $N^{\Delta t} \sim 10^7$ counts are collected. With this, values for the signal to background ratio in the order of 10^{-4} can be measured. Another limitation is the fact that if a combined electron-ion background is present, the measured signal has to be larger than this background:

$$R_S > R_{B,ei} \quad .$$

To enhance the sensitivity of the measurement, the signal to background ratio can be increased by increasing the ratio of the distance where electron-ion collisions are induced to the trap length. This can be done by using a bent trap. This way, only neutrals produced in the section pointing to the detector are recorded, halving the effective trap length. Improving vacuum conditions is another obvious possibility of cutting down the background rate.

Absolute cross section measurements

The animated-beam method [48, 49] provides an elegant method to avoid a separate measurement of the form factor. In short, this method makes measurements of absolute cross sections possible by scanning one beam through the other. This way the integrations in the form factor describing the geometrical overlap of the two beams (see formula 2.4) are implicitly taken into account. The movement has to range from a point where the electron beam is below the ion beam without overlap to a point above the ion beam without overlap. Scanning of the electron beam takes place at a rate of about 0.05 Hz in [48].

Chapter 3

Trapped keV Ion Beams

3.1 Ion trapping and storage techniques

Ion trapping techniques [50] have been used in different ways in the fields of physics and chemistry. Most commonly, ions are stored with very low kinetic energy in the range of a few eV or less by using static or time-dependent electromagnetic fields. The Penning trap [51] with electrostatic quadrupole and magnetostatic fields, the Paul trap or rf trap [52, 53] with time-dependent electric quadrupole and magnetostatic fields, variations of which are the Paul-Straubel trap [54, 55] and rf multipole traps [56], the Kingdon trap with pure electrostatic fields [57] and its continuation, the dynamic Kingdon trap [58] with static and time-dependent electric fields. In these traps, high precision laser spectroscopy, mass measurements and studies of particle dynamics are conducted. Collision studies have been conducted measuring dissociative recombination on ions stored in a Penning trap [1], and ion-neutral collisions in a rf multipole trap [59].
Single collisions can be studied using fast ion beams, as reaction products can easily be detected directly, owing to the well-defined kinetic energy and directionality of these beams. In order to avoid the short interaction times encountered in single-pass experiments, these beams can be stored in heavy-ion storage rings. Here, ions are stored at high kinetic energies (MeV) using a combination of magnetic steering and focussing fields. The main interests at storage rings are studies of interactions between ions and electrons using so-called electron coolers, laser cooling and beam dynamics.

Trapping and storing of ions is important not only to increase interaction times but, above all, to allow for relaxation of the energy initially stored in the vibrational and rotational degrees of freedom. This relaxation allows for some control of the initial ionic state. In low-energy molecular ion reactions with electrons, atoms and other molecules, as well as laser spectroscopy, reaction rates depend strongly on the population of rotational and vibrational states. For ions with permanent dipole moment, the vibrational and rotational energy is radiatively released during storage. Typical timescales for dipole-allowed transitions are milliseconds to seconds for vibrational re-

laxation and seconds to minutes for rotational relaxation.

Storage rings are the method of choice for most electron-ion collision processes [60], yet they suffer one major drawback concerning experiments with heavy molecules. In storage rings, the maximum field attainable in the dipole magnets limits the momentum of the particles that can be stored. The Lorentz force counteracts the centrifugal force:

$$Bqv = \frac{mv^2}{\rho} \quad ,$$

with ρ being the bending radius, B the magnetic induction and q, m and v the charge, mass and velocity of the ion. Using the magnetic rigidity $B\rho$ this can be written as

$$B\rho = \frac{mv}{q} \quad .$$

The magnetic rigidity is limited (at the TSR in Heidelberg it is 1.5 Tm), and thus, to store ions with higher mass-to-charge ratio, the velocity has to be decreased. Unfortunately, the ion loss due to the dominating restgas ionisation process is inversely proportional to the ion energy [61]. For heavy molecular ions storage lifetimes become too small to allow for relaxation of internal excitation.

To overcome this, various electrostatic trapping techniques have been established during the past few years, further completing the methods for experiments on stored ions. The idea of using electrostatic fields only is that trapping and storing are independent of the mass of the ion stored. An electrostatic trap also avoids one of the main drawbacks of the large storage rings, the presence of the guiding magnetic fields. These are in general strong enough to mix magnetic substates from different fine-structure components with the same magnetic quantum number. The ion beams in electrostatic trapping devices have keV energies, so ionisation of the restgas is negligible, the dominating loss processes are charge transfer reactions and collisions with the restgas. Among these electrostatic devices are electrostatic storage rings, the first of which was built in Aarhus, Denmark for 25 keV maximum energy with a circumference of 7.6 m (ELISA [62]). A similar ring was subsequently built at KEK in Japan with 30 keV maximum energy [63]. Another storage ring (50 keV maximum energy) of a different design is in preparation at the IAP in Frankfurt [64].

3.2 Electrostatic Bottle Trap

A different approach was chosen in the development of ion beam traps. Based on the electrostatic bottle trap [65], on which this work was performed, a simpler and more compact design was developed in Stockholm (Conetrap [66]).
In the following sections, the electrostatic bottle trap will be introduced and some relevant details explained.

3.2.1 Principle

The motion of charged particles in electrostatic fields is similar to the propagation of light in a medium where the index of refraction is proportional to the square root of the electric potential. Based on this analogy between ion optics and photon optics, an electrostatic trap for the storage of fast ion beams has been developed [65].
This method of trapping is based on the principle of an optical resonator, where a beam of photons is trapped between two mirrors. These resonators are extensively used in laser sources and their characteristics as well as stability conditions are well known.
The stability condition for trapping a Gaussian beam in a resonator of length L and mirrors with radii of curvature R_1 and R_2 is given by [67]

$$0 \leq (1 - \frac{L}{R_1})(1 - \frac{L}{R_2}) \leq 1 \quad . \tag{3.1}$$

For a symmetric resonator $(R_1 = R_1)$ and using the definition of the focal length $f = R/2$, this condition is equivalent to

$$\frac{L}{4} \leq f \leq \infty \quad . \tag{3.2}$$

Based on this equation and the analogy between ion and photon optics it is possible to trap ions between two mirrors with a focal length larger than a quarter of their separation.
The above condition is related to the transverse confinement of the ions in the trap. Another relation needs to be fulfilled, associated with the longitudinal confinement. This requires a potential barrier in the direction of motion of the ions to be higher than their kinetic energy.

3.2.2 Trap design

These two conditions are met with the design shown schematically in figure 3.1. The longitudinal confinement is achieved by five cylindrically symmetric electrodes, labelled E_1 to E_5, that produce a retarding field. The innermost electrode of this stack (E_5) is grounded, while the outermost electrode (E_1) is set to a potential V_1, which is high enough to stop the ions

$$V_1 > \frac{E_k}{q} \quad ,$$

where E_k is the ion kinetic energy and q their charge. An additional grounded outermost electrode G completes the arrangement to reduce the electric field outside the trap. Transverse confinement is achieved by a separate set of focussing electrodes, consisting of two additional electrodes, labelled Z_1 and Z_2, forming an asymmetric Einzel lens. Electrode Z_1 is at potential V_E, while Z_2 is grounded to provide a field free region in the centre of the trap. This field free region ensures that the ion beam is well defined both in energy and in direction. This is of advantage because it not only allows experiments with a well defined kinematic state, but it also ensures relatively
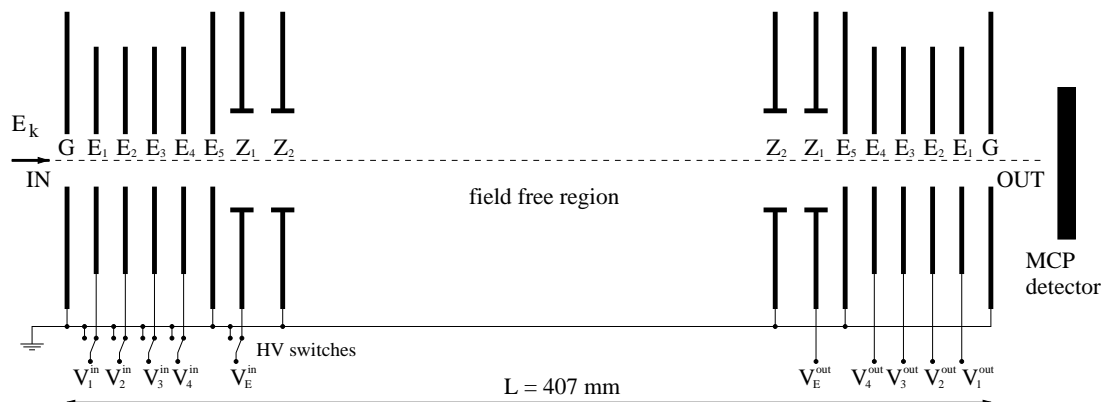
Figure 3.1: *Schematics of the electrostatic ion trap.*

easy detection of reaction products. It is even possible to place detectors inside the trap, as will be shown in section 3.3.

3.2.3   Operation of Electrostatic Bottle Traps

At injection of a monoenergetic, mass-selected ion beam, the entrance mirror electrodes are grounded to allow the beam to enter the trap and be reflected by the exit electrodes. The beam is chopped to match the trap length which usually corresponds to a pulse length of a few μs. As the front of the injected pulse returns to the entrance mirror, the voltages needed for storage are rapidly applied (with a risetime of about 100 ns) to match the values of the exit mirror. From this time on, the ions are trapped until the entrance mirror potentials are switched off and the beam exits the trap. A new injection restarts this cycle.

To investigate the behaviour of the trapped ions, a micro channel plate (MCP) detector located behind the exit mirror outside the trap is used. Neutrals produced inside the trap are unaffected by the mirror voltages and can exit the trap. Those that leave the trap through the exit mirror hit the MCP and produce a signal rate that is proportional to the number of ions in the trap. Another detection device is a cylindrical pickup, where a passing ion bunch induces image charge that can be interpreted as a measurement of the number of ions in the trap.

Important characteristics of the trap thus accessible are the trapping efficiency, the ratio of ions trapped to the number of ions initially injected, and the trapping stability. Theoretical calculations indicate efficiencies of up to 100 %, and measurements show values of the order of many tens of percent [68]. Trapping efficiency and stability is a function of mirror voltage settings and calculations can be used to determine optimal settings. The simulations made in [69] are based on SIMION [70] trajectory calculations as well as models that use the analogy of the trap to an optical resonator.

Beam losses that lead to the exponential decay curves for the MCP signal cannot easily

be simulated. Ions are lost due to collisions either with the residual gas or among the ions themselves.

In collisions with residual gas atoms, charge transfer reactions (electron capture for positive, electron detachment for negative ions) lead to neutral ions, giving rise to a signal on the MCP detector:

$$A^+ + X \rightarrow A + X^+ \quad .$$
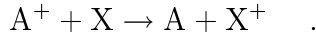
If σ_c denotes the cross section for electron capture for ions moving at velocity v_i and ρ_b the density of the residual gas, the expected lifetime due to this process is given by

$$\tau_c = \frac{1}{\sigma_c \rho v} \quad . \tag{3.3}$$

When comparing different ion species it is important to note that the cross sections for electron capture are more or less in the same range for most of the singly charged ions. The dominant factor affecting the storage lifetime is therefore the velocity v, so that lifetimes are expected to scale as $\sqrt{m}$ with m being the ion mass.

Equation 3.3 is only valid at a given constant velocity. As the ions are slowed down before being reflected in the mirror region, this is not exactly the case here. However, the maximum error between a value obtained using the velocity associated with the injection energy and a correct integration of the above formula using the velocity distribution in the trap and velocity-dependent capture cross sections is 10 % [68]. Cross sections are only weakly dependent on the energy.

Measured lifetimes generally fall short by a factor of 4 - 7 of the values predicted by equation 3.3. This discrepancy can only be explained by other loss processes, of which elastic or inelastic scattering of ions from the residual gas atoms is probably the most important. Owing to the fact that angular scattering is a strong function of the ion velocity, this process could be dominant in the mirror sections, where the ion velocity approaches zero. If the ion is scattered into an unstable orbit, the ion will be lost, not giving rise to a signal on the MCP.

Further ionisation of the trapped ions is negligible at ion energies of a few keV.

A third possible ion-loss process is collisions among stored particles, where one ion is lost if scattered into an unstable orbit. This process is only important in regions of high ion density inside the mirror regions. Its influence is expected to be limited to short storage times, when high ion densities are more likely. This can be verified by injecting beams of different intensities and comparing the decay behaviour.

To quantify scattering processes the angular acceptance of the trap needs to be evaluated. As the acceptance angle changes dramatically depending on the position inside the trap from milliradian in the centre to values almost three orders of magnitude larger at the turning points, a full understanding is not yet achieved [71].

Experimentally, the long-time decay behaviour shows a dependence on the mirror potential settings. For this part of the decay two processes are important: firstly the charge exchange reaction, which is independent on the mirror configuration and the scattering of the ions from the residual gas. The latter process depends on the mirror

electrode settings [68], not only because the cross section depends on the trajectories and thus on the mirror settings, but also the acceptance angle depends on the mirror settings, especially on the Einzel lens potential.

Because of this, the lifetimes are expected to be slightly shorter for the longer bent trap than for the shorter linear trap, for which the optimal settings are also better established.

A typical storage lifetime for the linear trap is 3-4 s for Ar^+ at a pressure of around $5 \cdot 10^{-10}$ Torr.

3.2.4   Scope of past and ongoing experiments

The electrostatic trap described above has been successfully operated for a few years, measuring lifetimes of metastable states of both positive (NO^+[72], Xe^{2+}[73], HeH^+ [74]) and negative ions (He^-[75], Be^- [76], C_n^-, n =2-6 [77]).

Another very promising set of experiments was conducted with this trap as a mass spectrometer [78]. Here the trap acts as a multireflecting time-of-flight mass spectrometer, where ion flight paths are in the range of kilometers. With the help of compensating mirror settings and a recently discovered synchronisation effect [79, 80], very high mass resolution can be achieved.

3.3   The Bent Electrostatic Trap

The trap used for electron-ion collision experiments discussed in this work is an extended version of the electrostatic bottle trap described in the last section. It is schematically shown in figure 3.2. The similarity in the design can be seen with the two mirror sets facing each other, the only difference is a slightly longer trap length (670 mm instead of 407 mm). By introducing an ion-optical deflector in the trap centre can direct the ion beam onto a second set of mirror electrodes located at 33 degrees.

One advantage of storing in this bent mode is a lower background rate on the MCP detector outside the trap as only neutrals created in one half of the trap can hit the detector on the straight section. Additionally, with a detector inside the trap on the bent section, a mass separation of fragments is available and various coincidence measurements are possible where a neutral count on the outer MCP and a specific charged fragment count on the inner MCP is required. It also extends the trapping technology for these kind of traps tremendously.

3.3.1   Trap setup

Vacuum chamber

The whole trap assembly (figure 3.3) is set up on a horizontal mounting plate ('breadboard') inside a large vacuum chamber. The mounting board sits on three stainless steel balls held by the bottom plate of the vacuum chamber. The advantage of this design is that everything connected to the trap optics can be fixed to the breadboard.
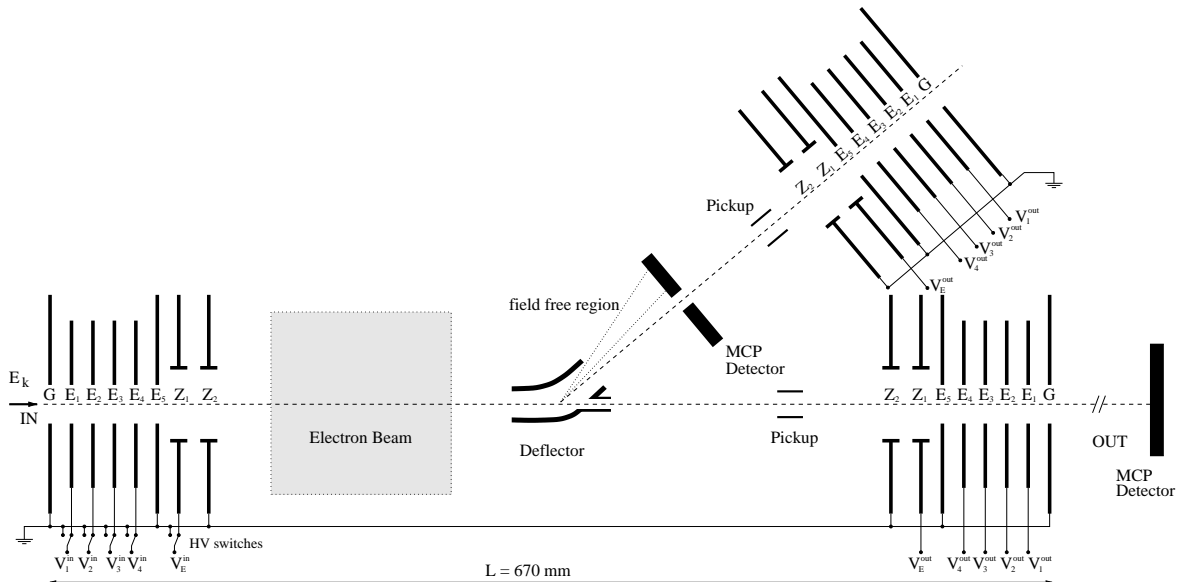
Figure 3.2: *Schematics of the bent electrostatic ion trap. The proposed position for an electron beam is shown in grey. Trajectories for fragments in the deflector are indicated as well as the position of the MCP detector and the pickups.*

This allows for a consistent alignment of the mirror electrodes, the deflector and other trap parts as well as a relatively simple alignment of the whole trap with respect to the ion beam axis.

The vacuum chamber is pumped by a cryopump located below the chamber. This placement underneath the breadboard is detrimental with respect to pumping speed. With the aid of the central hole in the breadboard, about 220 threaded placement holes, 4 holes to connect to the feedthrough flanges underneath as well as the annular gap between the breadboard and the vessel walls a pumping speed of about 700 l/s can still be achieved [81]. Additional cryopumps outside the chamber assist by differential pumping.

The chamber is equipped with a vacuum ion gauge as well as a residual gas analyzer. Heating tapes have been added to the chamber to allow for baking. Viewports can be used to shine in laser beams for experiments on laser-ion interactions. Various additional ports on the vacuum vessel serve as feedthroughs for detectors and other installations. Access to the chamber is via a dome-shaped cover that can be sealed with either rubber or copper wire gaskets.

Trap elements

The electrostatic mirror assembly can be seen in figure 3.4. The mirror electrodes are suspended from a support bracket that is directly screwed onto the breadboard. The stack of electrodes is clamped together between the innermost electrode and the outermost grounded electrode (Z_2 and G in figure 3.2) with ceramic spacer spheres
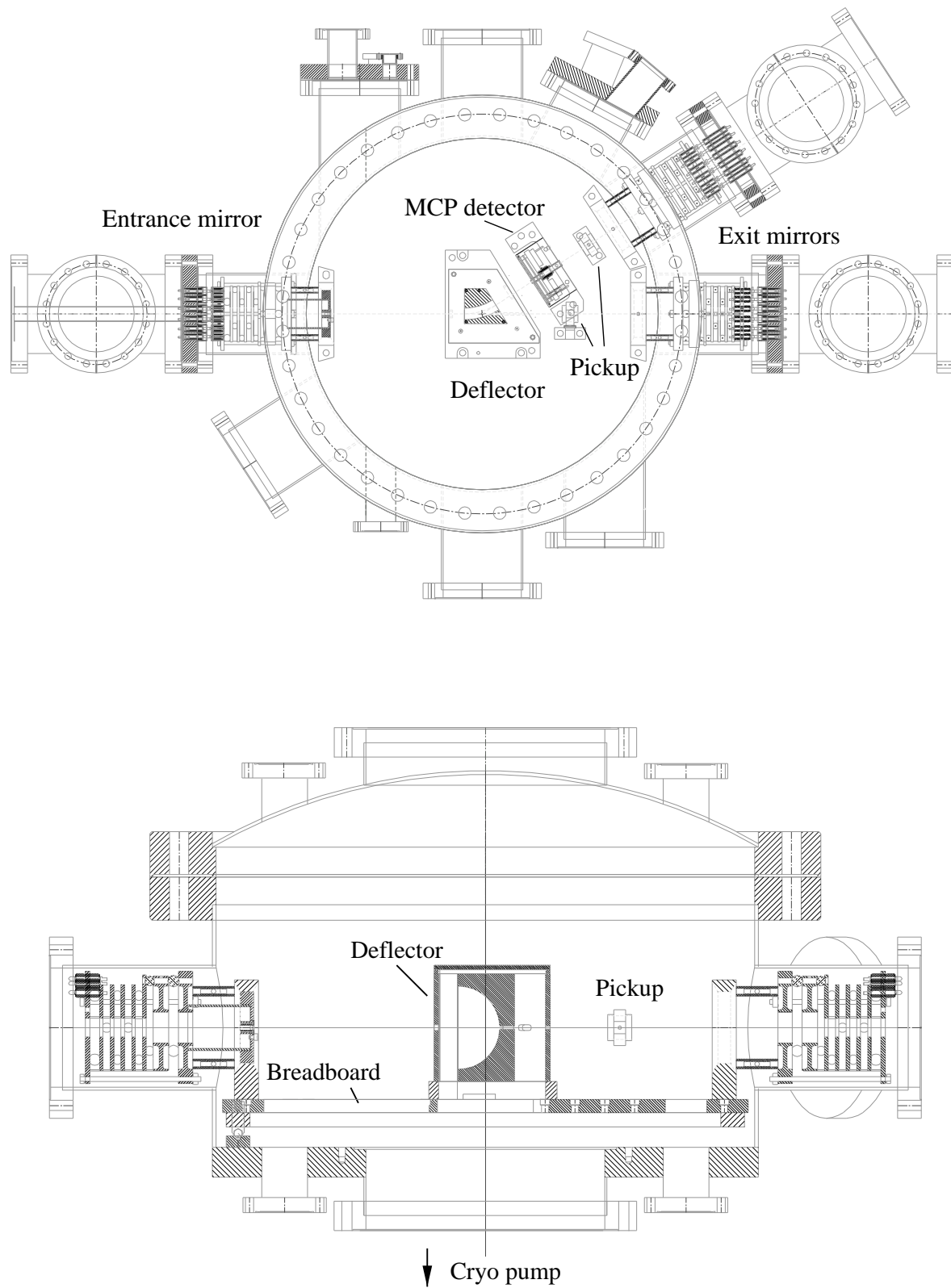
Figure 3.3: *Top and side view of the Bent Electrostatic Trap chamber.*

in between. Potentials are supplied via wires spot-welded to the electrodes and fed through the grounded clamping plate to pins that stick out from the grounded clamping plate. At insertion of the mirror assembly into the trap chamber, these pins connect up to spring-loaded pistons attached to a double-sided conflat flange that couples the trap chamber to a four-way cross through which the wires are brought out of the vacuum. The pins as well as the corresponding pistons are embedded with macor shielding pieces for electrical insulation. These macor pieces are responsible for one of the problems showing up when the electron beam is operated. This will be discussed in more detail in section 5.2.1. The entrance mirror and the two exit mirrors are all made identical.
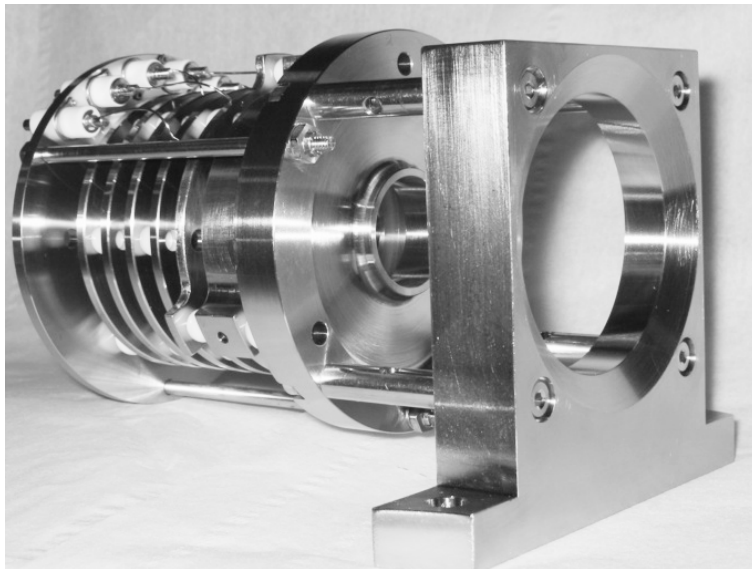

Figure 3.4: *Mirror assembly of the bent electrostatic trap. On the outermost grounded clamping plate to the left the macor pieces insulating the potential pins can be seen.*

Deflector

The optical deflector consists of two suitably shaped plates that deflect the ion beam by 33 degrees and also focus the beam additionally. The deflector is retractable being suspended from a rod coming down through a manipulator equipped feedthrough on the top of the dome cover. The two deflector plates are placed inside a grounded box and clamped between two plates with ceramic spacer spheres in between. The bottom plate retracts into a recess clearance in the base plate and thus aligns the deflector plates when lowered into position. The whole assembly is guided on two rods with linear ball bearings. High voltage can only be applied to the deflector plates with the deflector in *down* position, only then are pins connecting up to spring loaded contacts and disconnecting it from the grounded bottom clamping plate. This ensures no charging is possible when the deflector is retracted in *up* position.

fragment detection

The deflector can be used to detect charged fragments created by electron collisions. Being lighter than the parent ion, these fragments are deflected stronger in the electric field of the deflector. Figure 3.5 shows a SIMION simulation [82] of the relation between fragment mass and deflecting angle. A mass separation of ion fragments is thus possible with a position-sensitive detector after the deflector. Fragments with masses smaller than 65% of the parent mass cannot be detected with the current deflector, as these fragments are deflected so strongly that they start to hit the HV plates. Another restriction presently in place is the aperture in the grounded box that encloses the deflector plates. This restricts the minimum mass that can be detected to about 85% of the parent mass. The latter restriction is relatively easy to lift as it only requires an enlargement of the aperture. The other restriction requires an elaborate modification of the deflector plates.
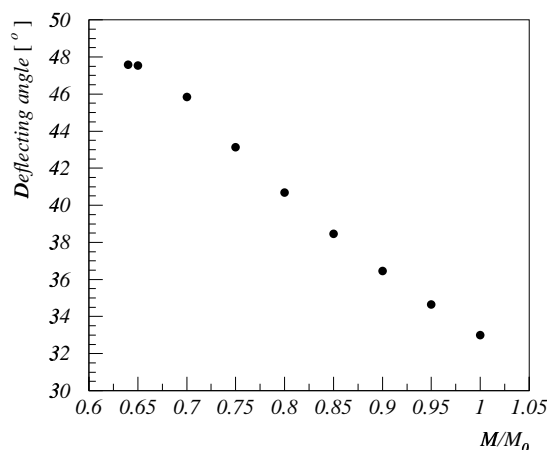

Figure 3.5: *Deflection properties of singly charged fragments with mass M and singly charged parent ion of mass M_0. The kinetic energy is 4.2 keV, the deflector voltages are $V_D = \pm 0.69087$ kV.*

To detect the fragments, a position-sensitive detector has to be brought close to the ion beam axis. Although only on one side of the ion beam, towards larger deflection angles, fragments are expected, a circular detector with central hole was chosen, namely a 40 mm diameter Multi Channel Plate (MCP) detector with a Resistive Anode (RA)[1]. The ion beam passes through the central hole of the detector. This way, any possible distortion by the applied HV at the detector is cylindrically symmetric. This might only add another lens effect to the ion optics that can be corrected for easily. Secondly, this way the sensitive area can be brought much closer to the beam axes. When placing such a detector to one side of the beam as close to the beam axis as possible, the

---

[1] Quantar Technology 3300/2401B

outside margin of insensitive material has to be taken into account. The comparable inside margin around the central hole is much smaller. To minimise the influence of the applied MCP potentials on the ion beam, a grounded drift tube is put inside the central hole. According to [83], another tube on intermediate potential is needed between the grounded inner tube and the MCP plates to increase acceptance around the centre of the detector. Additionally, the whole detector assembly is placed inside a grounded metal box, leaving only the (grounded) detector surface exposed (figure 3.6). Depending on the expected fragment masses, the distance of the detector to the deflector can be varied.
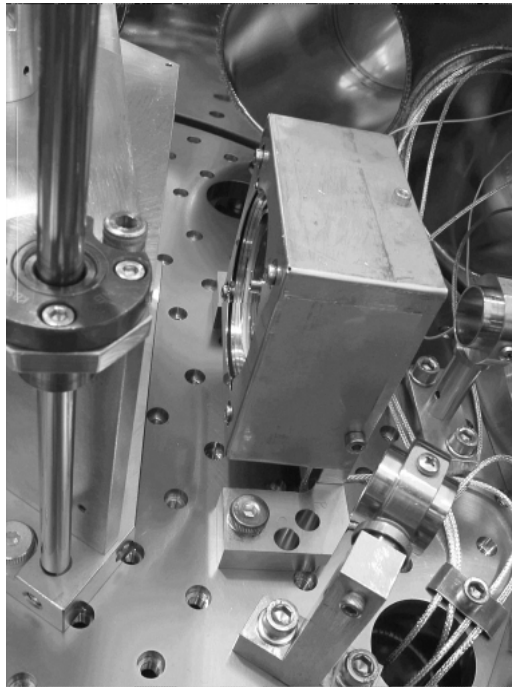

Figure 3.6: *The MCP for fragment detection on the bent section together with the two pickups. The circular hole in the grounded shielding box exposes the detector surface. In the middle, the small grounded drift tube is visible. To the left, the grounded box of the deflector can be seen with on of the guiding rods.*

3.3.2 Operational experience with the bent trap

Storage experiments were performed with a 4.2 keV Ar$^+$ beam of a few tens of nA current at typical trap pressures in the 10^{-10} Torr range.

trapping lifetime

For the bent electrostatic trap the same diagnostic tools as for the linear trap are available: A neutral rate MCP detector outside the trap on the straight section and

pickups inside the trap, located both on the bent and the straight section. In figure 3.7, an example of an MCP signal is shown. Depending on the mirror settings, a
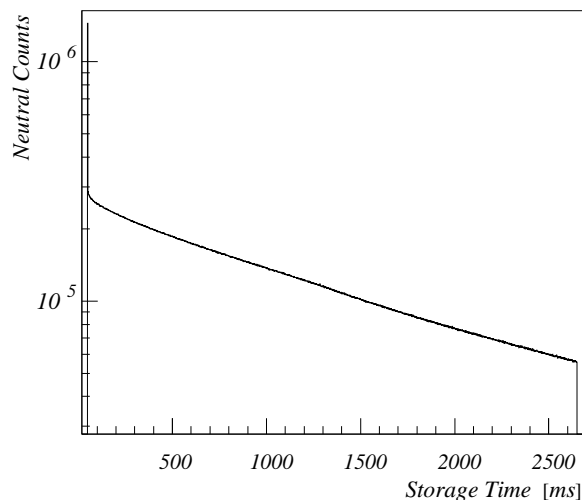

Figure 3.7: *MCP signal coming from the neutral particles leaving the trap through the exit mirror. As the ion beam is injected into the trap, an large pulse arising from the injected ion beam shows up. The stored ions decay exponentially. After some defined time, the entrance mirror potentials are lowered and the beam exits the trap.*

distinctive lifetime and decay characteristic is obtained. At small storage times, a multi-exponential decay might exhibit, as different trap orbits have different decay properties.

With the electron target in place, two pickups are installed close to the exit mirrors. In figure 3.6, the picture of the pickups inside the trap shows their position behind the deflector and the MCP detector on the bent section. With the signal derived from the pickup, trapping can be monitored as well as a parameter proportional to the number of ions in the trap. This will later be used for a normalisation of the measured cross section, as it does not depend on the ion species as the MCP neutral signal, but only on the charge within the ion bunch. Only if the ion beam stays bunched inside the trap, this signal can be obtained. An example of a pickup signal is given in figure 3.8. Each passage of the ion bunch with a width of 1 μs induces charge on the pickup which is amplified and seen as a peak in the waveform. As the pickup is not centred in the trap, the distance between the peaks is not uniform and a double peak spectrum arises. The time for one revolution is about 6 μs for Ar^+ shown here. Usually the ions undergo an exponential decay and the bunch diffuses until the trap is evenly filled. To prevent this debunching, rf bunching techniques can be employed. A small sinusoidal rf signal of matching frequency and about one volt amplitude is applied to the externally grounded electrode E_5. The bunch behaviour can be monitored with the pickup. The diffusion can be seen as an increase in peak width, the decay as a change of the envelope of the peaks for short times when the peak width does not change or more precisely as a
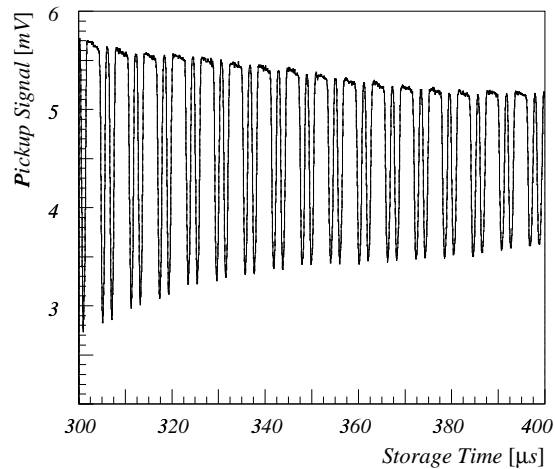
decrease in peak area.

Figure 3.8: *Oscilloscope screenshot of the pickup signal.*

deflector tests

Applying an appropriate positive HV on one deflector plate and corresponding negative HV on the other, the ion beam is deflected onto the exit mirror on the bent section. When switching off the HV, the undeflected ion beam can pass the outside deflector plate through a 3 mm hole and reach the exit mirror on the straight section. It could be shown that when switching the deflector HV fast enough the same ion beam can first be directed onto the bent section, then onto the straight and back on the bent section again without losing trapping. This can be seen in a measurement where three pickups were installed inside the trap, between the entrance mirror and the deflector (pickup 1, instead of the electron beam) and two between the deflector and the exit mirror, one on the straight (pickup 2) and one on the bent section (pickup 3). These tests, shown in figure 3.9, demonstrate the versatility and capability of the trap. Pickup 1 on the top shows pickup signals from the ion bunch throughout the timewindow plotted, pickup 2 on the straight section detects only a residual signal while the deflector potentials are applied and the ions stored on the bent section, where pickup 3 detects them.

status of trap operation

Ion beams can be stored in the bent electrostatic trap and some experiments prior to upgrading it with the electron target have been performed. Its capabilities regarding storage on the bent section have been nicely demonstrated. However, storage lifetimes measured were considerably shorter than those in the linear trap under similar vacuum conditions. Optimisation of trapping conditions by changing the mirror configuration

is a time-consuming process and has not yet been completed for all possible configurations. With the electron target installed, typical lifetimes were initially in the order or slightly below 100 ms. For one configuration, namely storing in straight mode with the deflector up, this value could be increased, up to lifetimes of about 2-3 s, only slightly shorter than expected from linear trap values. The measurements shown in chapter
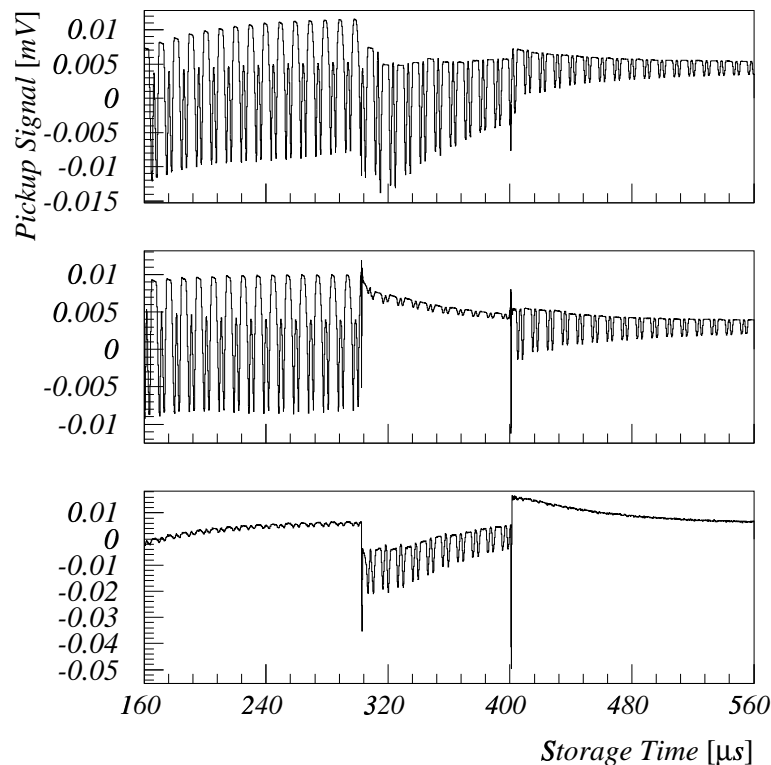
Figure 3.9: *Switching the ion beam from straight mode storage to bent mode storage by rapidly applying deflector HV for some time. Pickup 1 near the entrance mirror (top), pickup 2 on the straight (middle) and pickup 3 on the bent section (bottom).*

5.3 have been performed in this mode. For configurations with the deflector down, requiring a smaller ion beam diameter to clear the apertures in the deflector housing, no optimisation has been performed yet. These conditions are however desirable for reducing the background for electron-ion collisions experiments by using trapping in bent mode and and for a more precise analysis of the electron beam profile as will be explained later. The MCP inside the trap chamber is installed and connected, but has not been operated yet.

Chapter 4

Sheet Electron Beam

In this chapter, the design and setup of a sheet electron beam serving as an electron target for crossed beams experiments inside the bent electrostatic trap are presented. The requirements imposed on the design considerations by the trap environment are discussed and the means chosen to comply with the given framework presented. Simulations based on these ideas are described in the following section, together with a brief overview on their mechanical implementation.

This chapter concludes with a presentation of results obtained in tests of the electron target in stand-alone operation.

4.1 Basic considerations

Building a electron-ion collision experiment in the above mentioned trap environment needs several constraints and requirements to be met. With the goal of studying electron-ion collisions at collision energies of a few eV to several tens of eV, a crossed beams experiment is the simplest and most straightforward solution.

Constraints and requirements

The electron beam has to be installed inside the trap, within the field free region. The natural position of such an interaction is between the entrance mirror and the deflector, in order to use the trap in both bent and straight mode. This imposes geometrical constraints on the dimensions of the electron target, while the overlap of the ion beam with the electron beam should be as large as possible to ensure the best possible signal-to-noise ratio.

Another important consideration is to ensure that the trap vacuum level remains more or less unaffected by the operation of the electron beam. An increase in pressure would increase the background level on the detector outside the trap chamber due to a higher restgas collision rate, and also decrease the lifetime of the stored beam. This could mean that relaxation of internal excitation cannot be achieved, making experimental results difficult to analyze.

The advantages of using only electrostatic fields for trapping have been already mentioned. In order not to loose this advantages, the electron beam has to do without the help of magnetic fields. Magnetic fields in beam direction are widely used to guide the electron beam. Because of electrostatic repulsion, a beam of electrons diverges if their charge density is not negligible. With a magnetic field in beam direction, the transverse velocity of the electrons leads to a cyclotron motion and as a result of this the electrons are spiralling around the magnetic field lines.
A magnetically confined beam requires a considerable magnetic field which would affect the ion storage.

Altogether there should be no adverse effect on the ion trapping, be it due to pressure increase or any residual field created by the installed electrodes.

Design solutions

Critical in fulfilling the above mentioned requirements is the type of cathode used. Based on the experience gained at the TSR electron cooler in Heidelberg, where thermionic emission from a dispenser cathode is used in UHV conditions [84], a dispenser cathode was chosen.
These cathodes [85] use dipole surface layers which create a local electric field to decrease the work function for the thermionic emission of the electrons. They essentially consist of a porous metal matrix (usually tungsten) interspersed uniformly with the emitting material. The matrix acts as a reservoir for the emitting material or impregnant from which it can diffuse to the surface to maintain the active layer. The most commonly used impregnant is the mix 5 BaO: 3 CaO: 2 Al_2O_3, simply referred to as 532. Overcoating the cathode with certain metals can significantly reduce the work function of the emitting surface. Although these coating metals have higher work functions values than tungsten, the overall work function of the emitting surface, consisting of a barium and oxygen layer onto the coating metal as a substrate is less than that of a comparable tungsten surface. Common coating materials are osmium-ruthenium (the so-called M type), iridium and scandium oxide (X type). The thickness of the sputter-coated layer is typically 300-500 nm. The advantage of an M type cathode is a lower operation temperature than that of a standard dispenser cathode for the same current density.
Current densities that can be achieved for a type 532 M cathode at zero field emission are typically between 12 to 16 A/cm^2 at 1050°C [86]. For our application only negligible current densities are needed, below 1 mA/cm^2 for the envisaged beam energy range.
The temperature-dependency of the work function is described as $1.43 + 4.4 \cdot 10^{-4} \times T$ eV, temperature T in Kelvin [87], or 2.02 eV at an operation temperature of 1050°C. The cathode assembly (type 53280, M coated) used for this work was manufactured by HeatWave[1]. It has a non-inductive (bifilar) wound heater and only non-magnetic materials are used to ensure minimal distortion of the electron beam. The heater is

---

[1]http://www.cathode.com/

electrically insulated from the rest of the cathode structure up to a breakdown voltage of about $20 - 30$ V.

AC heating is required for filament and insulation lifetime increase. With DC heating, electrolysis occurs between the heater wire and the heater cavity with the insulating material in between, leading to breakdown. With the closer spacing of the wires of a bifilar heater, AC heating is mandatory, unless the cathode is specifically designed for compliance with DC heating.

The emitting surface is concave (see figure 4.1) to facilitate the interplay of initial over-focussing of the beam and coulomb repulsion by space charge needed when no magnetic guiding field is present. See also beam simulations in the next section.
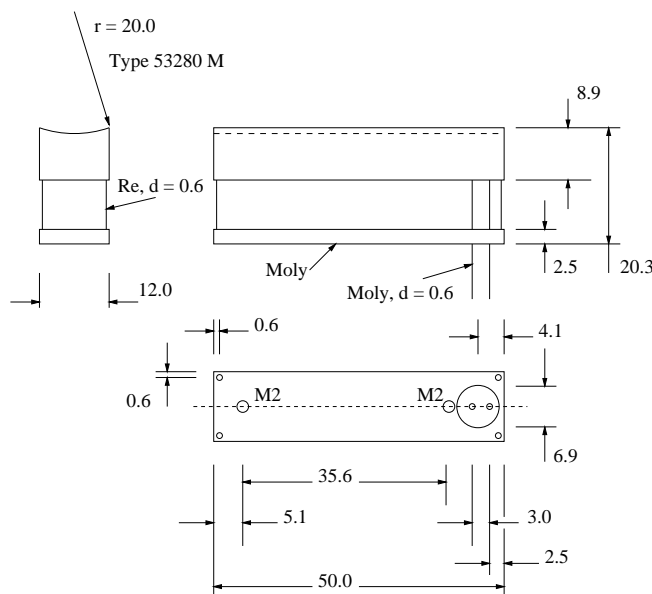

Figure 4.1: *technical drawing of cathode assembly, dimensions in mm.*

Because of the relatively large dimensions of the cathode assembly in our application, considerable care has to be taken to ensure minimal heat dissipation into the trap chamber. A copper cooling block is placed around the cathode assembly, leaving only the emission surface exposed. Additional heat shields made from molybdenum are placed between the cathode and the cooling block. Estimated unshielded power dissipation using Stefan-Boltzmann's Law is in the order of 500 W at an operating temperature of 1050°C, whereas when shielded, the calculated value matches the actual power dissipation of about 150 W.

4.2   Simulations

In this chapter, the principles of thermionic emission will briefly be discussed to a level necessary for a more detailed understanding of the basis of the simulations.

The simulations were performed making use of two software codes, SLAC [88] and MAFIA 4 [89]. The initially used SLAC Electron Optics Program was used for 2D calculation of the geometry, later on also for different collector types. As it can only handle 2D calculations in the version which was at hand, subsequent simulations were performed using the space charge limited emission macros available within MAFIA 4. With this 3D simulation tool, the behaviour of the electron beam in the horizontal plane was optimised. Additionally, the influence of misadjusted electrode potentials as well as the effect of the earth magnetic field was investigated.

Both codes use an iterative procedure to solve for the correct space charge effect. They start with a given magnetic and electric field configuration based on the geometry and the potentials specified and calculate trajectories for electrons in a first cycle. These results are then used to deposit charge appropriately along the trajectories for the next cycle until convergence is reached in the following iterative process.

Basics of thermionic emission

The Richardson-Dushman Equation is the fundamental equation of thermionic emission and describes the current density j emitted from a uniform metal surface at a given temperature T [90]:

$$j = A(1 - r)T^2 e^{-e\Phi_{eff}/kT} \quad , \tag{4.1}$$

where the constant A is given by $A = \frac{4\pi mk^2 e}{h^3} = 120$ A/cm^{2}K^2. The coefficient r describes the probability of electrons crossing the potential barrier at the metal surface being reflected when the electric field outside the surface is zero. Φ_{eff} is the effective electronic work function and defined such that the amount of work needed to remove an electron inside the material to a position outside is e Φ_{eff}. It depends slightly on temperature and the electric field at the surface (figure 4.2). For temperatures used for thermal emission, the dependence is governed by the exponential factor.

In a real cathode-anode arrangement with a positive anode potential U with respect to the cathode the current follows equation 4.1 only up to a certain critical temperature. With higher temperatures, the current stays constant. This can be readily explained with the existence of space charge. Electrons travelling from the cathode to the anode shield the electric field from electrons just being emitted from the cathode. At the critical temperature, the field at the cathode is totally screened. The number of electrons emitted from the cathode equals the positive charge on the anode. With even higher temperature, more electrons are emitted and the charge between the cathode and the anode is larger than the positive charge on the anode, space charge arises. This gives rise to a retarding potential for the electrons emitted from the cathode which not only have to overcome the work function Φ_{eff}, but also this space charge potential V_m. Electrons with insufficient kinetic energy cannot overcome V_m and contribute to the space charge potential. In equilibrium, there is a potential minimum, the virtual
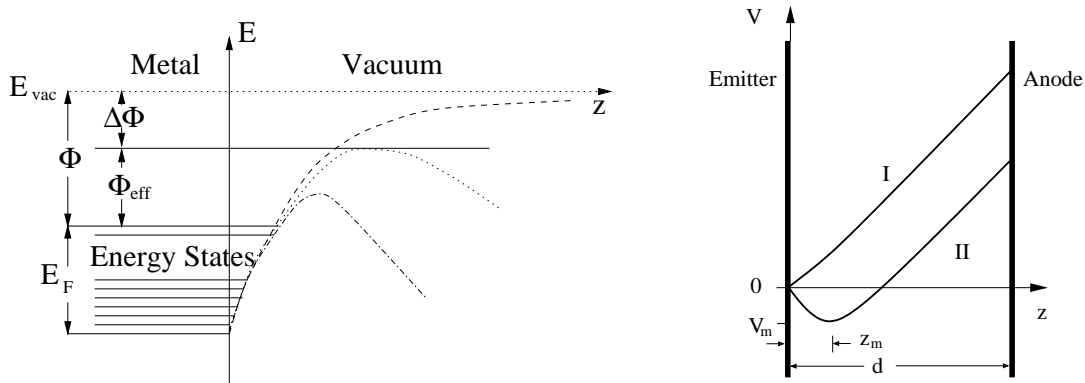
Figure 4.2: *left: simplified energy model of a metal-vacuum boundary. The effect of an external field on the effective potential barrier Φ_{eff} can be seen. right: potential between cathode and anode for temperature-limited regime (I) and space charge-limited regime (II).*

cathode, an electron cloud which is being fed by the cathode, and from which electrons are extracted to the anode (see figure 4.2, right). A few μm is a typical dimension for the distance of this electron cloud to the cathode surface. The advantage of this electron cloud is that surface imperfections like patches with different work function are smeared out by electron-electron interactions in the cloud and thus do not influence the beam homogeneity. Another reason why electron guns are operated in this space charge limited regime is the fact that the current density is not or at least less sensitive to variations in cathode temperature than in the current-limited regime where the Richardson Equation holds.

In the case of a planar cathode-anode geometry, the Child-Langmuir Equation describes the space charge limited current density [91]

$$ j = \frac{4\varepsilon_0}{9}\sqrt{\frac{2e}{m}}\frac{V^{3/2}}{(z-z_m)^2} \quad . \tag{4.2} $$

Here, V is given by the difference of the applied cathode-anode potential U and the space charge potential V_m. To extend the applicability of the Child-Langmuir Equation to other geometries, it is often written as [92]

$$ I = PU^{3/2} \quad , \tag{4.3} $$

where the current I and the applied voltage V are linked with the factor P, called the perveance. This parameter depends on the geometry, in particular it is proportional to the cathode surface area and contains the cathode-to-anode distance ($P \sim 1/z^2$). It is generally given in units of 10^{-6} A/V$^{3/2}$, or 1 μPerv.

It is necessary to understand from the scaling laws in space charge flow without applied magnetic field that the trajectories of the electrons do not change with electron energy.

For a more general view on scaling laws beyond the special case shown here, see [93]. This behaviour was used doing the actual calculation of the trajectories and also simplifies the operation of the electron target, so a short proof will be given here.
The equation of motion when $\vec{B}$ - fields can be neglected is given by

$$\frac{d^2\vec{x}}{dt^2} = -\eta\vec{E} \quad .$$

If the new potentials scale as $\Phi_n = \mu\Phi$, the electric field $\vec{E}$ scales accordingly: $\vec{E}_n = \mu\vec{E}$. The equation of motion for the scaled problem can be written as

$$\frac{d^2\vec{x}}{dt^2} = -\mu\eta\vec{E} \quad .$$

If $\vec{x} = \vec{f}(t)$ solves the initial equation of motion, the scaled potential problem is solved by $\vec{x} = \vec{f}(\sqrt{\mu}t)$. These are the same trajectories, executed $\sqrt{\mu}$ times as fast.
To see that the above statement about the scaling of the $\vec{E}$ - Field holds, break the field into components arising from the electrodes and the space charge of the electron beam: $\vec{E} = \vec{E}^e + \vec{E}^{sc}$.
For the electrode part of the field, $\vec{E}$, the scaling is obvious from the definition of the electrostatic potential $\vec{E} = -\nabla\Phi$

$$\vec{E}_n^e = \mu\vec{E}^e \quad .$$

For the space charge part of the field recall the properties of space charge flow: The current density scales $\vec{j} \propto \mu^{3/2}$. Together with the electron velocity scaling $\vec{v} \propto \mu^{1/2}$, this gives a scaling of $n \propto \mu$ for the charge density n, given by $n = \frac{\vec{j}}{e\vec{v}}$ and similarly a scaling of $\rho \propto \mu$ for the charge density ρ, given by the volume integral over the current density times the charge carried, $\rho = q\int_V n\,dV$. Finally it follows from Maxwell Equation $\nabla\vec{E} = 4\pi\rho$ that indeed

$$\vec{E}_n^{sc} = \mu\vec{E}^{sc} \quad .$$

This fact simplifies the operation of the electron target. To adjust the electron energy, the applied potentials are simply scaled by a factor given by the ratio of desired to previous electron beam energy.

4.2.1 Principle of operation

The SLAC simulation in figure 4.3 is used to exemplify the considerations leading to the final electrode design. The arrangement is symmetric with respect to the horizontal plane, so each electrode function is achieved by a pair of electrodes.
The general idea mirrors in the geometry of the cathode. Without magnetic confinement by applying a field parallel to the electron beam direction, the electrons diverge quite rapidly due to their mutual repulsive coulomb force. To overcome this, electrons are starting from a curved cathode which would lead to an overfocussing if repulsion was not present. If the right amount of repulsion comes into play, the interplay between charge repulsion and initial overfocussing can lead to a balancing of effects and a nice
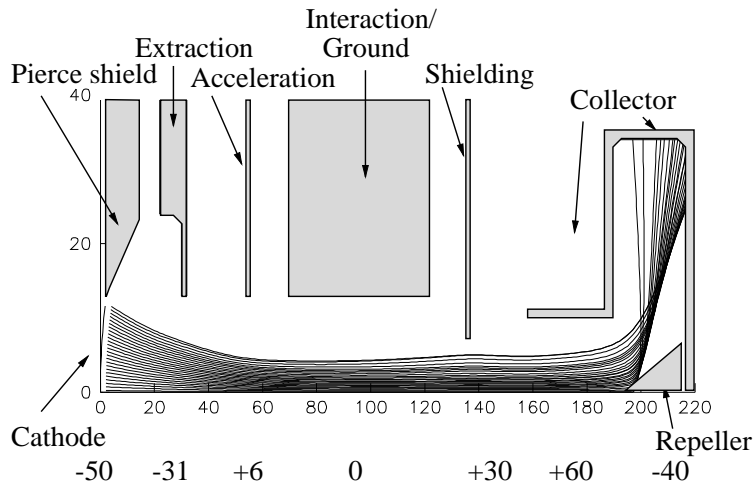
Figure 4.3: *SLAC Simulation with the final collector geometry; the actual shape of the electrodes is superimposed on the plot. Units on the axis correspond to 0.5 mm. In the bottom row, the potential values used for this simulation are given in Volts.*

neckshape form arises.

It is known that appropriate *shields* around the cathode make the equipotential lines become parallel to the cathode surface with space charge forming a virtual cathode. The angle of the shield to achieve this for a planar cathode-anode geometry is known as the Pierce angle, at 67.5 degrees [93]. In our application with the curved cathode a modified angle of 35.5 degrees was found in simulations to be optimal. (This angle corresponds to an angle of about 68 degrees against the cathode's normal at the border, close to the Pierce value.) To ensure a smooth transition of the equipotential lines at all edges similar shields have been installed to the sides of the cathode also. These side shields simply extend the cathode surface but can be biased with respect to the cathode for fine-tuning. The starting condition of the electrons at the edge of the cathode surface can be modified depending on the offset of shield and cathode. The amount of repulsion depends on the charge density $n = \frac{\vec{j}}{e\vec{v}}$. The current density $\vec{j}$ is controlled by the first pair of electrodes following the cathode, the extraction electrodes. On the other hand, the charge density also depends on the energy (velocity) of the electrons. Thus, to achieve a desired charge density, the position of the extraction electrodes with respect to the cathode (governing the perveance and thus the current density) has to be chosen carefully if these electrodes also define the electron energy. In order not to constraint oneself at too early a stage and also to ensure versatility later, the extraction and acceleration of the electrons from the cathode is attributed to different electrodes. The *extraction electrodes* govern the amount of current density drawn from the cathode and the acceleration electrodes define the beam energy. The *acceleration electrodes* serve two purposes: Firstly, they accelerate the electron beam towards the final energy which is defined by the potential difference between the cathode and the interaction region. Having this electrodes on a slightly positive potential ensures a smooth tran-

45

sition from the accelerating field to the uniform quasi-field free drift region between the following interaction electrodes. Secondly, it can be seen from MAFIA simulations described in the next section that making them narrower than the other electrodes confines the beam in y direction.

The interaction region where the electrons eventually impinge on the ion beam coming in perpendicular to the electrons' direction is located between the *interaction electrodes*. These electrodes are sitting on ground potential and are broad enough to ensure uniformity of potential over the interaction volume.

For first test measurements, a very simple electrode arrangement was used. Only the collector followed the interaction electrodes. This situation can be seen in figure 4.11 and also in the MAFIA 4 simulation plots. After initial testing of this setup, this arrangement was changed: it turned out to be preferable (less leakage current) to postaccelerate the electrons after the interaction region towards the collector.

This postacceleration is achieved mainly with the *collector*. The *shielding electrodes* ensure that this accelerating field does not spill into the interaction region. The special shape of the collector and the the *repeller* serves the purpose to annihilate the electrons is such a way that the amount of secondary electrons backtracking into the interaction region is minimised.

4.2.2   3D simulations with MAFIA 4

To assess the behaviour of the electron beam in the horizontal plane simulations with MAFIA 4 were performed. The deviation of the electron impact angle from the designed $90°$ should be minimised. Such a deviation arises when the coulomb repulsion from the beam space charge is not counterbalanced. With counteracting fields this can be achieved, as can be seen in figure 4.4.

By making the acceleration electrodes narrower than the other electrodes, equipotential lines become curved at the beam edges. The more positive the potential on the acceleration electrodes, the more pronounced this effect shows up. This focussing effect of the acceleration electrode can be seen from figures 4.5. As the electrons move perpendicular to the equipotential lines shown in these figures, it can be seen that initially, the electron trajectories diverge in y direction. An offset on the side shields (separated by short lines from the cathode, but on the same potential in the simulations) would improve the initial divergence by making the equipotential lines parallel to the surface. At some distance from the cathode, the equipotential lines become convex, forcing the electron trajectories inwards. Note also that the electrodes are wider in y than the electron beam to ensure well defined fields over the whole beam volume.

By adjusting electrode potentials in such a way that the electron beam starts hitting the electrodes, a prediction about the overall stability of the beam shape against variations and misadjustment can be made. One motivation was to use the onset of leakage current upon hitting certain electrodes to verify the simulations. Experimentally, this proved to be not successful, probably more due to other factors governing the leakage current and masking the desired effect (see section 4.3.3) than due to deficiencies in
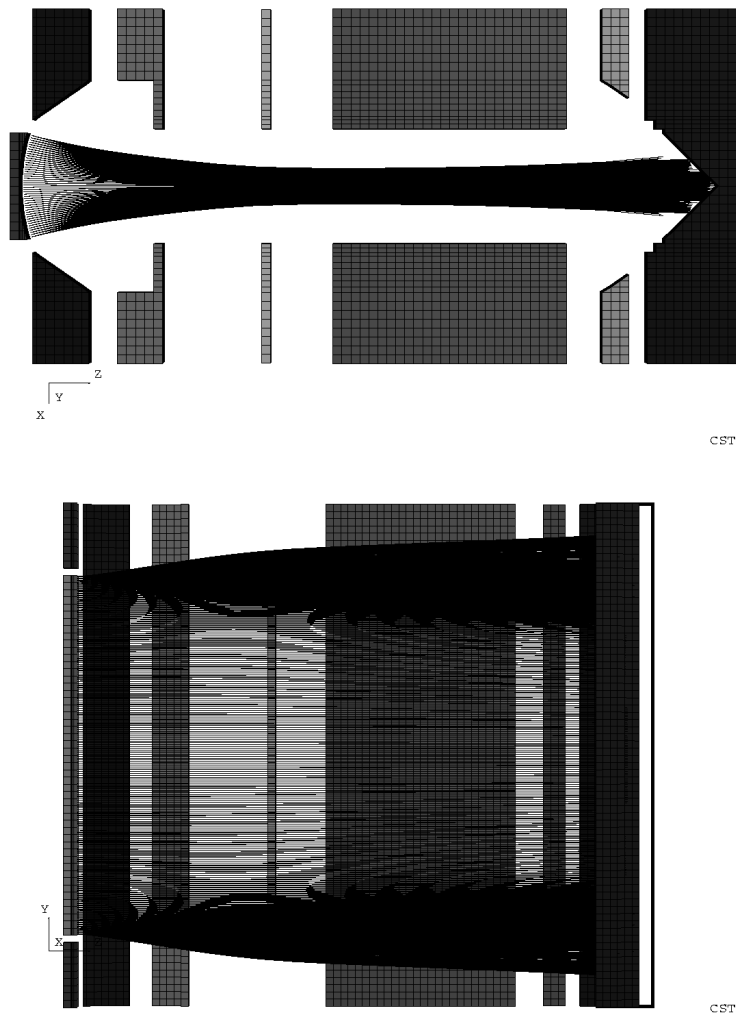
Figure 4.4: *MAFIA 4 simulation giving the electron trajectories with a simple collector geometry. On the top a side view is shown, on the bottom a top view with the electrodes on the top of the beam removed. In both plots, the cathode is to the left. In order to reduce calculation time (MAFIA 4 uses time steps to track the trajectories), the potentials were scaled by a factor of 1000 with respect to the 50 eV 'standard' and shifted to be all positive.*
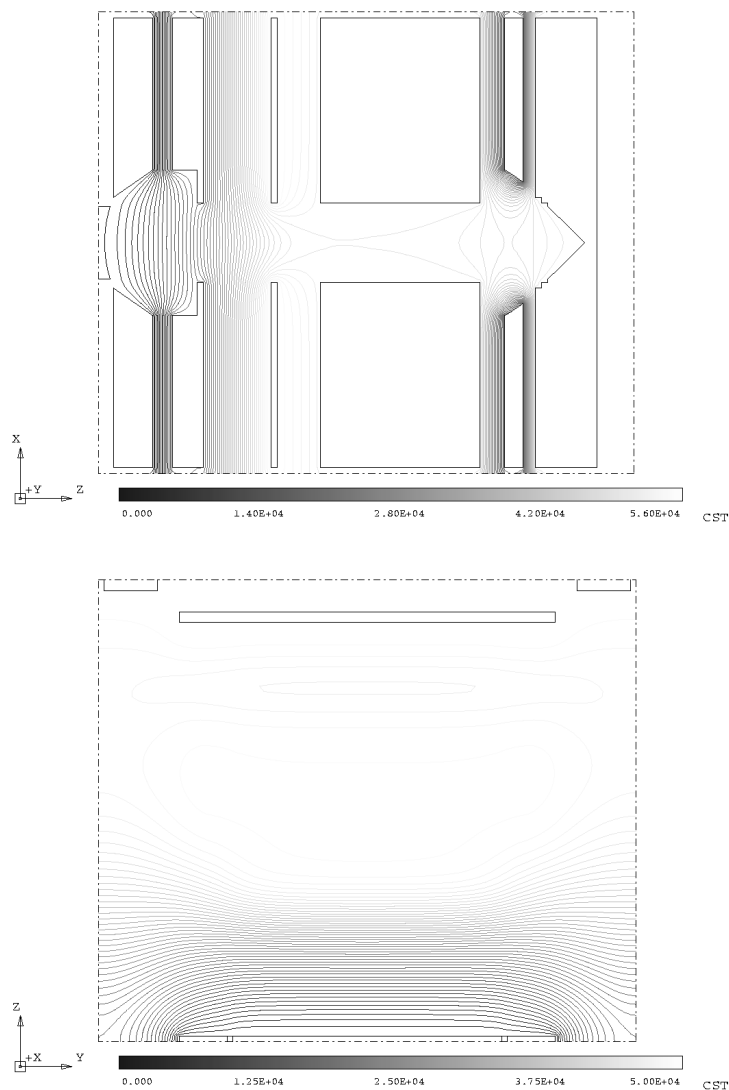
Figure 4.5: *MAFIA 4 simulation giving the Equipotential lines with a simple collector geometry. On the top, a vertical cut through the centre of the electron target with the cathode to the left is given, on the bottom, a horizontal cut through the centre is shown. Here, the cathode with the side shields (separated by a small gap) can be seen on the bottom. Both are on the same potential and the effect of the virtual cathode can clearly be seen: the equipotential lines bulge above the surface of the cathode.*

the simulations.

Of these series of simulations, the one in figure 4.6 nicely illustrates the role of the extraction electrode. This is worth emphasising as this shows the general principle of balancing space charge repulsion and overfocussing. With this electrode, the amount
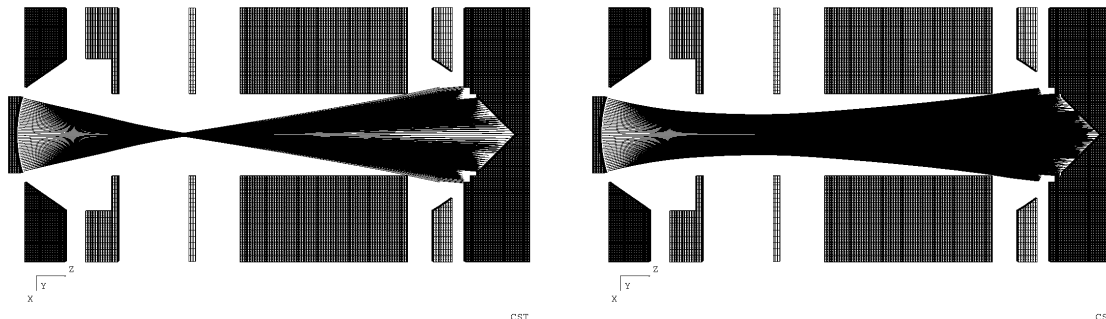

Figure 4.6: *MAFIA 4 Simulation showing the effect of varying the Extraction Electrode potential. On the left, the extracting potential is -42.5 V; only little current is drawn from the cathode. On the right, the extracting potential is -22.3 V, lot of current is drawn resulting in a diverging beam.*

of current is controlled and subsequently, the balance between space charge repulsion of the electrons and the overfocussing initial trajectories. With too little current, the overfocussing leads to electrons starting from above the centreplane to cross this plane in a focal point and impinging on the lower interaction electrode (see figure on the left). With too much current, the electrons repel each other immediately so that electrons starting from the upper part of the cathode eventually hit the upper interaction electrode (see figure on the right). The range of possible values in which the interaction electrode is not hit provides some idea of the stability of the settings, although the beam profile of course changes tremendously for different settings. The calculated range was: $-22.3V$ to $-42.5V$ with $-31V$ being the optimal setting.

The effect of the earth magnetic field can be significant at low electron energies (figure 4.7). Depending on the orientation of the electron beam, the effect is more or less dramatic. With the horizontal field component being in electron beam direction the electron beam is actually confined favourably. With the horizontal field component and the electron beam direction perpendicular to each other, the deflection is maximal. On the testbench in Heidelberg, the electron direction was north-south, so the influence of the earth magnetic field is minimised.

The earth magnetic field is given by [94]

$$\vec{B} = B_0(\cos\Phi, 2\sin\Phi) \quad ,$$

where Φ is the magnetic latitude , $B_0 = 3.1 \cdot 10^{-5}$ T. The first component of this vector gives the horizontal component pointing to magnetic north, the second the vertical

component. The magnetic latitude for Heidelberg is 49°, for the Weizmann Institute in Rehovot 31.9°. On the basis of the simulations for which in figure 4.7 examples are given, a compensation of the earth magnetic field seems to be advisable. See section 4.3.5 later in the chapter.
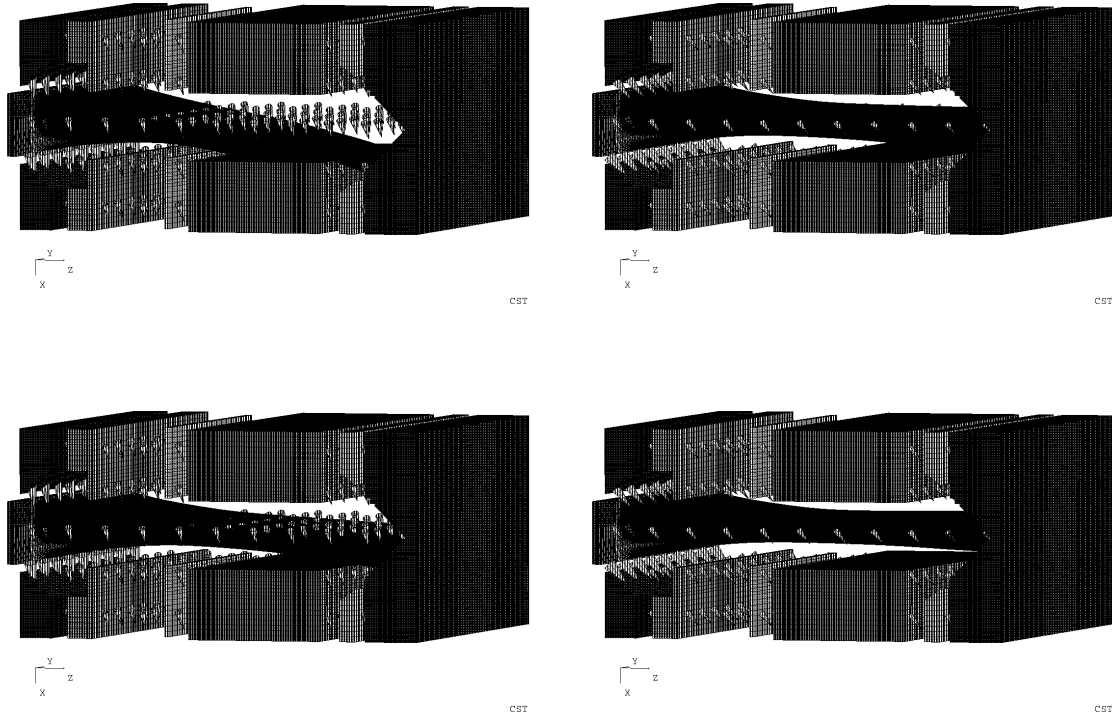

Figure 4.7: *MAFIA 4 Simulation showing the effect of the earth magnetic field on a 5 eV (top) and a 50 eV electron beam (bottom). On the left the orientation of the horizontal field component is in y direction, on the right in z direction. For the simulations, the magnetic latitude of Rehovot, IL has been used.*

4.2.3 Collision energy and expected resolution

The residual field in the interaction region due to the space charge of the beam and the influence of neighbouring electrodes can be simulated. In figure 4.8 the difference between the true electron energy and the potential applied at the cathode is shown for a 50 eV beam. This effect is dependent on the electrode settings, most notably the electrodes close to the interaction region, the acceleration and the shielding electrode. The magnitude can be as high as 0.85 eV, resulting in electrons with true energy of 49.15 eV at a cathode setting of -50 V.

50

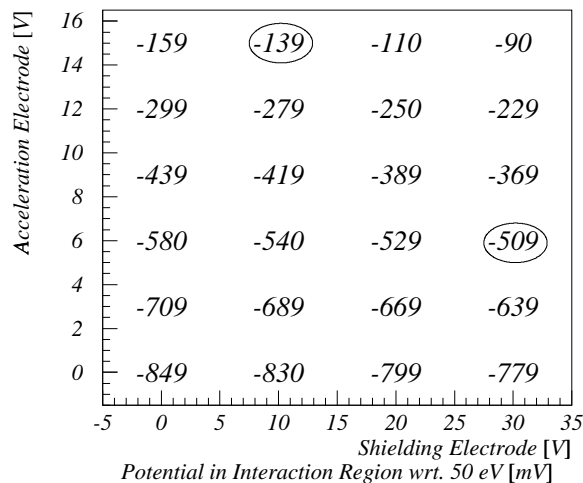*Potential in Interaction Region wrt. 50 eV [mV]*

Figure 4.8: *Potentials in the interaction region. The difference is shown to the applied 50 volts. These values scale with electron energy. The settings marked with circles refer to potentials used in experiments.*

The error contributions on the collision energy introduced in section 2.4 can also be assessed with simulations. The error on the electron energy, ΔE_e, is primarily given by the cathode temperature, kT, corresponding to about 0.1 eV. Another contribution is from the inhomogeneity of the potential in the interaction volume. This can be estimated from simulations and scales with electron energy. It is dependent on the exact potential settings, especially of the acceleration and shielding electrodes. In figure 4.9 this inhomogeneity is characterised by the standard deviation for the potential in the interaction region. An unweighted value was obtained for a 3 mm ion beam. For the plots in figure 4.10 the error ΔE_e is computed from

$$\Delta E_e{}^2 = (0.1\text{eV})^2 + \left(2.2 \cdot 10^{-3}\ E_e\right)^2 \quad ,$$

using the value for a shielding potential of 10 V and acceleration potential of 15 V from figure 4.9. The error on the ion energy, ΔE_i is governed by the source conditions and the acceptance of the beamline and is estimated to be about 4 eV.

The error on the angle of electrons with respect to the ion beam direction is taken from MAFIA 4 simulations and estimated to be about 2°. Only an angle against the normal plane of the ion beam direction matters.

In figure 4.10, the error contributions are shown individually and combined as a function of ion mass. The contribution of the ion beam energy is negligible, dominating is the error caused by the electron beam energy and the electron impact angle. Both of these error contributions depend on the electron beam energy. The dependence on the electrode settings can be immediately seen for the case of $\Delta E(e)$, the error in electron beam energy, from figure 4.9. It depends mainly on the settings of the acceleration and the shielding electrode. For the case of $\Delta E(\theta)$ the dependence stems from the correlation between the acceleration electrode potential and the impact angle θ. As already
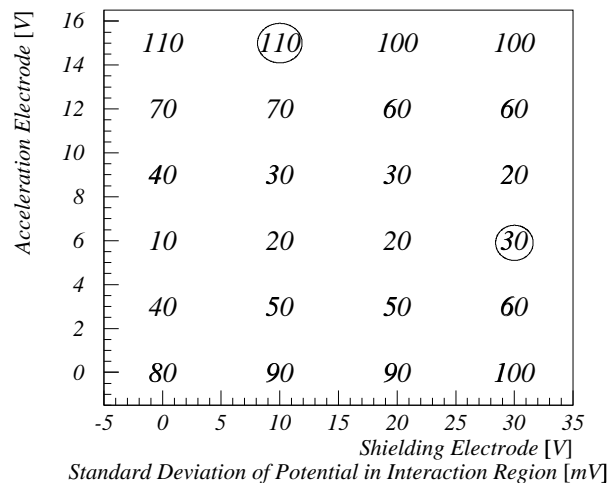
51

Figure 4.9: *Standard deviation of the potential in the interaction region for a 50 eV beam. These values scale with electron energy. The settings marked with circles refer to potentials used in experiments.*

shown in figure 4.5, the acceleration electrode provides a distortion of the electric field that helps counteracting the repulsion of the electron beam in horizontal direction. Due to the limited availability of the MAFIA 4 code, no simulations were performed to study the influence of different potential settings on the impact angle. With standard potential settings regarding extraction and shields governing the electron density, 6 V need to be applied to the acceleration electrode for a 50 eV electron beam. Setting the acceleration electrode more positive leads to a stronger focussing effect; with less positive potential, the repulsion dominates. When applying different potential settings to extract higher current values at the same electron beam energy, a higher potential value is needed at the acceleration electrode. In first order, the repulsion should be proportional to the electron density. At a given energy, this means that the acceleration potential should scale with the current drawn.

4.2.4 Mechanical implementation

The mechanical parts of the electron target were manufactured in the workshop of the Max-Planck-Institute for nuclear physics in Heidelberg. For the suspension of the electrodes, ceramic rods are used which are held in a frame made of titanium (see figure 4.11). The electrodes are electroeroded from titanium. Special care needs to be taken to choose materials that can be used near a working dispenser cathode without degrading their emission properties. From the list of favourable materials given in [95], none could be chosen because of unjustified high costs or difficult or even impossible processing and machining involved. Titanium was chosen because of its rather high melting point and the fact that it has almost identical temperature expansion coeffi-
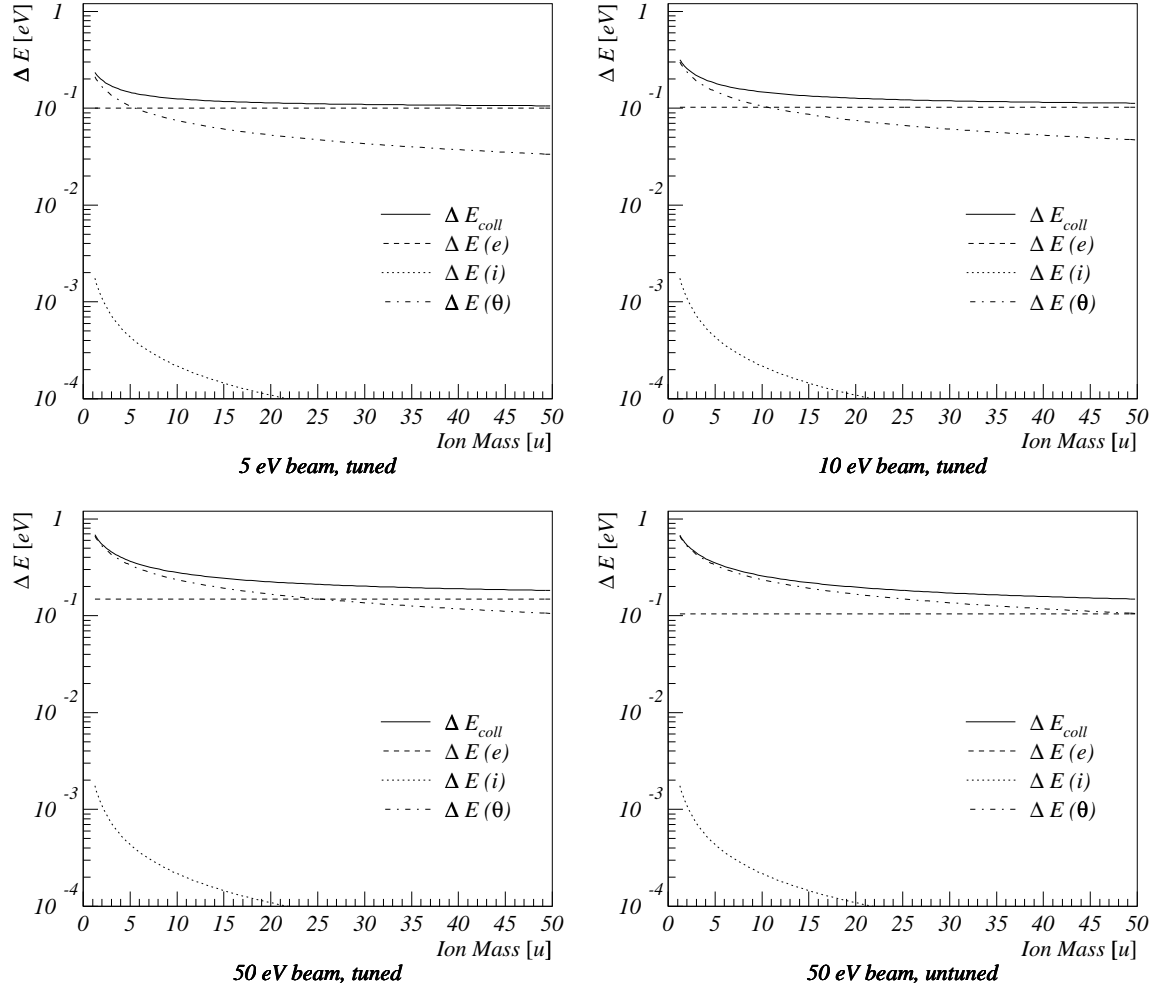
Figure 4.10: *Error contribution from the electron beam energy $\Delta E(e)$, the ion beam energy $\Delta E(i)$ and the angle of electrons with respect to the ion beam axis $\Delta E(\theta)$. The total error on the collision energy ΔE_{coll} is also shown. The dependence on the electron beam energy can be inferred from the three plots at 5, 10 and 50 eV. All these are computed with 'tuned' electrode potential, where there is a higher variation of potential inside the interaction volume. As a comparison, a calculation for a 50 eV beam is also shown with 'untuned' electrode settings.*
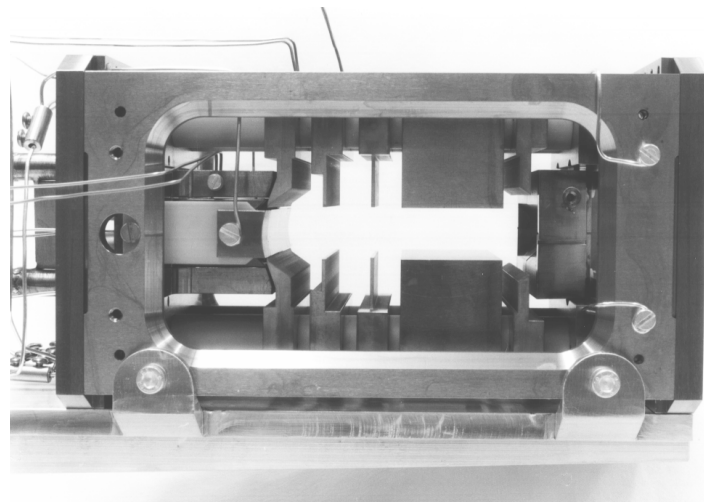
Figure 4.11: *The electron target with the first version of the collector before the first tests.*

cient as the ceramic used. Thus, thermal stress when operating the cathode can be minimised. For the less critical collector, stainless steel is used for ease of manufacturing. All materials are chosen to be UHV-compatible and non-magnetic.

The design allows for flexibility in later changing electrode position and shape by simply stringing up the electrodes and matching ceramic spacers differently on the suspended ceramic rods held by the frame.

4.3 Test results and experience gained in stand-alone operation

In figure 4.12 the electron target can be seen mounted on an 8" flange with all the necessary feedthroughs: cooling water, electrode potentials, cathode heating power and thermocouples. This arrangement is placed onto a vacuum test chamber for stand-alone testing of the electron target.

Viewports allowed monitoring of the cathode temperature with an optical pyrometer, while the temperature of the cooling block and two electrodes was measured with thermocouples. All electrodes were connected to power supplies via a resistor, such that the current on the lead could be controlled. The cathode was heated with a floating variable transformer, making use of the water pipes and one high power feedthrough as input and output lines. Magnetic correction coils were added around the chamber to compensate the earth field.

After the initial activation by slowly increasing the cathode temperature while monitoring the vacuum level, a temperature to power calibration was performed. With applied
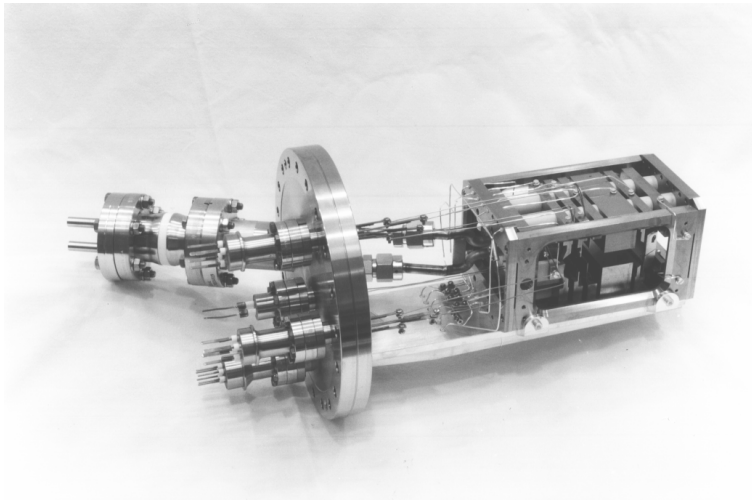
Figure 4.12: *Setup with electron target on test chamber installation.*

potentials, current was seen, although considerable leakage current was observed on several electrodes. The effect of varying the simulated electrode potential values on the leakage currents was investigated, trying to minimise these. With the help of the magnetic correction coils, the influence of the magnetic field on the electron beam's performance was tested.

Results of these tests are presented and discussed in the next sections.

4.3.1 Power - cathode temperature calibration

For these measurements, an optical pyrometer with a tungsten filament was used. The temperature derived from the pyrometer is calibrated for tungsten. Although the cathode is mainly made from tungsten, the spectral characteristics are modified by the coating material, in our case of an M type cathode osmium and ruthenium. With the spectral emissivity known, the actual temperature of the cathode can be deducted from the measured apparent value.

As a rule of thumb, the spectral emissivity of an M type cathode is roughly 0.05 higher than uncoated cathodes. Published data indicates the spectral emissivity of porous tungsten is $\epsilon = 0.46$ (compared to 0.43 of non-porous material) and that impregnated cathodes are 0.52. (both measured at 650 nm). This would lead to a value of about 0.57 for an M type cathode [96].

Using the Kirchoff law, the spectral emission is given by [94]

$$R = \epsilon \, R_b = \epsilon \, \frac{8\pi h \nu^3}{c^3} \, e^{-h\nu/kT}$$

with R_b the emission of a black body. If a body of actual temperature T is measured with a pyrometer to be of temperature T', the actual temperature can be derived if

the spectral emissivity ϵ is known:

$$R = \epsilon \, \frac{8\pi h\nu^3}{c^3} \, e^{-h\nu/kT} = \frac{8\pi h\nu^3}{c^3} \, e^{-h\nu/kT'} \quad ,$$

or

$$\frac{1}{T} - \frac{1}{T'} = \frac{k}{hc}\lambda \ln \epsilon \quad .$$

If a tungsten filament pyrometer is used that is calibrated for tungsten, then the actual temperature of a body with known spectral emissivity ϵ can be calculated from

$$\frac{1}{T} - \frac{1}{T'} = \frac{k}{hc}\lambda \ln \frac{\epsilon}{\epsilon_W} \quad ,$$

with ϵ_W the spectral emissivity of tungsten.
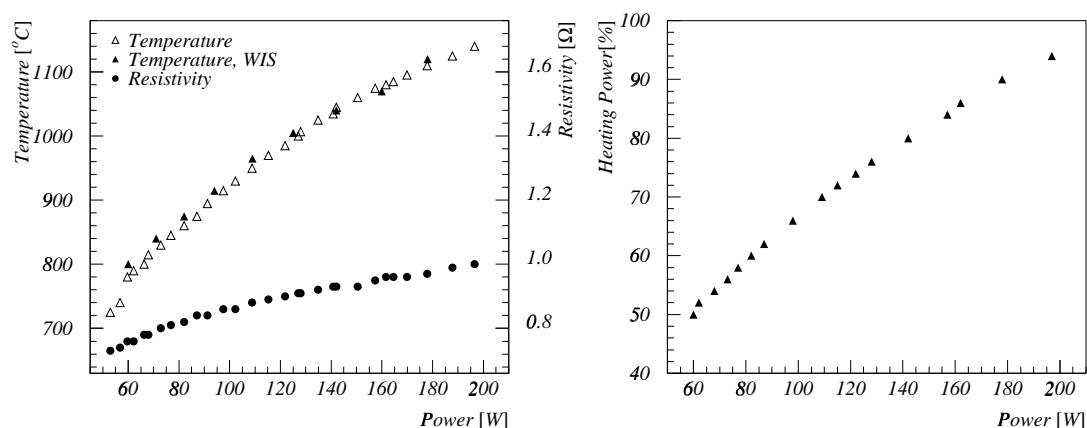
Figure 4.13: *Measured cathode temperature versus heating power. Values measured in Heidelberg (open triangles) and at the Weizmann Institute (closed triangles) match quite nicely. The resistivity of the cathode circuit is also drawn. On the left, the heating power as marked on the variac versus actual heating power in Watt is shown.*

With these considerations, measured values in the range of 600 to 1200°C are about 1 to 2 % too high. Compared with the reading accuracy of about ± 5°C, and no need for very accurate values for our purposes, no correction is applied in the diagrams in figures 4.13.

At a cathode temperature of 1050°C, the titanium electrodes acquire a temperature of about 270°C. The cooling block, fed with water at about 16°C and a pressure of 4 bar does not change its temperature.

4.3.2   Perveance measurement

Not only is the perveance an important characteristic of an electron beam device, it also provides another comparison between simulations and experiment. In figure 4.14

the measurement is shown, together with two fits according to equation 4.3. The cathode current yields nice agreement with a 3/2 power law and a perveance of 1.34 μP. The current collected behind the interaction region at the shielding electrode and the collector ('effective collector current') does not exhibit this dependence. Especially at small electron energies there is a significant difference between cathode current and effective collector current. Measurements were taken with the simulated potential values and shield offsets to minimise the leakage current.
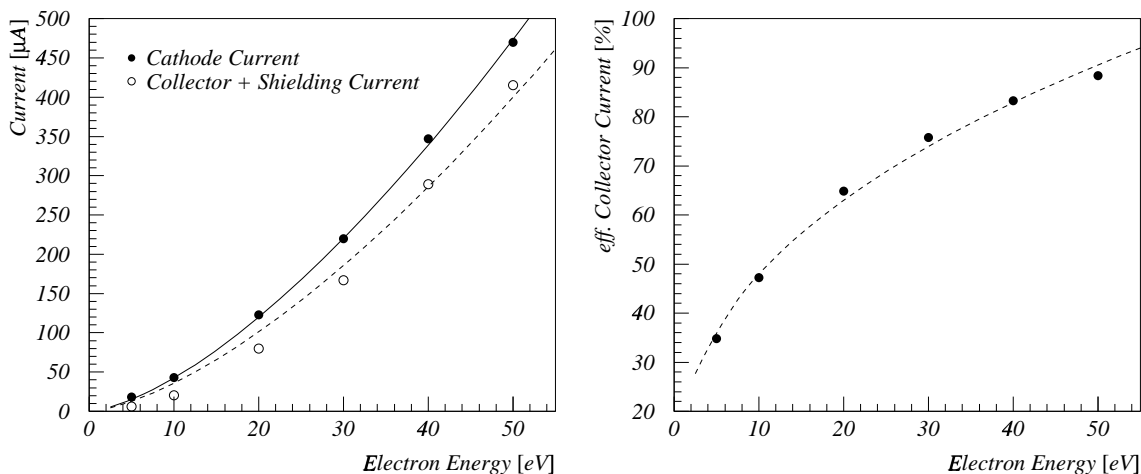

Figure 4.14: *left: perveance measurement. Data points for the cathode current are nicely fitted with a 3/2 power law, resulting in a perveance of 1.34 μP. Data for the effective collector current do not follow the dashed fit, shown for comparison; the calculated perveance here is 1.13 μP. right: effective collector current in percent of the cathode current. The dashed line corresponds to an analytical approximation used later in section 5.3.4*

The fact that the leakage current does not scale in the same way as the cathode current already gives an indication that the origin of the leakage current is in a way not directly connected with the primary electron beam but rather an unwanted, 'secondary' effect. Simulated values for the perveance are 1.32 μP from the MAFIA 4 calculation and 1.34 μP from SLAC, in good agreement with the measurement.

4.3.3 Current yield and current distribution

The electrode potential settings from simulations are used as starting points for the following measurements. The aim is to see the dependencies of the leakage current and possibly reduce it. In prior measurements it showed that further accelerating the electron beam after the interaction region improves the leakage current situation. This lead to the construction of a different electrode arrangement in the collector region. For this, the following values are taken as standard simulation values for a 50 eV beam:

Cathode	Extraction	Acceleration	Interaction	Shielding	Collector	Repeller
-50	-31	+6	0	+30	+60	0

Both types of *shields*, pierce and side, are offset for these measurements to values that suppress leakage currents on these shields. A comprehensive discussion of the correct shield offset is outlined later in this section. For the following measurements, each electrode potential is varied while the values of the rest is kept at the simulated value. The most critical electrode potential is the potential of the *extraction electrode*. As can be seen from figure 4.15, applying more negative potential reduces the potential difference with respect to the cathode and therefore results in less current drawn. With less current, the ratio of current collected on the collector improves.

The effect of varying the *acceleration potential* is less pronounced (figure 4.15, right). There is no change in total current expected as the first electrode should solely govern
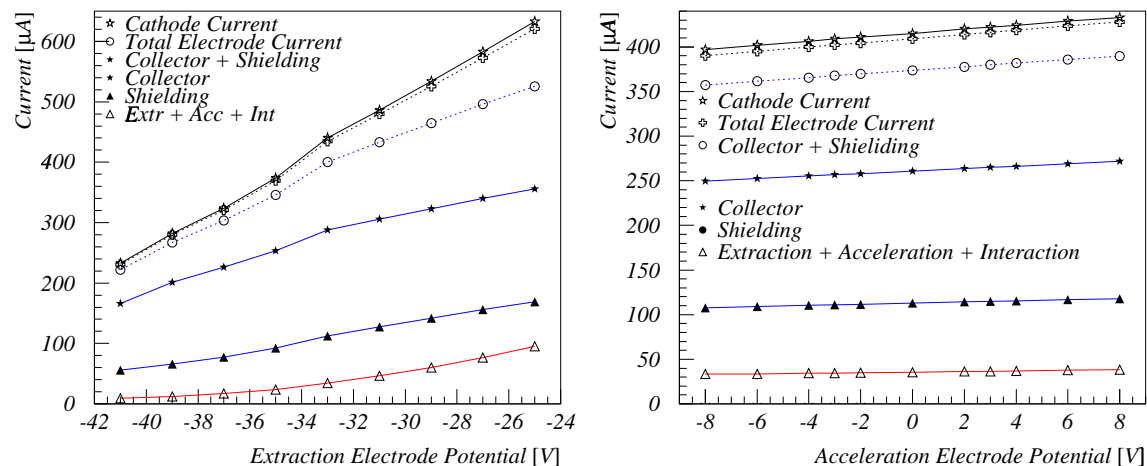

Figure 4.15: *left: effect of varying the extraction potential. right: Effect of varying the acceleration potential. It has to be noted that with this measurements, the shield offsets were different from the optimal values, therefore here, less total current is drawn.*

the extraction properties. The small variation is due to the spilling of the potential into the volume between the extraction electrode and the cathode. Overall, a change in the acceleration potential does not play an important role for the leakage currents; the ratios stay almost constant throughout the range observed. However, as this electrode is used to shape the beam horizontally it is still important to have this electrode at the correct setting. However, the correct setting cannot be determined by looking at the leakage currents.

One important point can be made when looking at the distribution of leakage currents more closely (figure 4.16). A small change in the potential of the acceleration electrode changes the distribution of leakage current between the interaction electrode (on ground potential) and the acceleration electrode. If the acceleration electrode is negative, the interaction electrode sees the leakage current whereas when increasing the potential to more positive values, the acceleration electrode sees it. Such an effect can only be
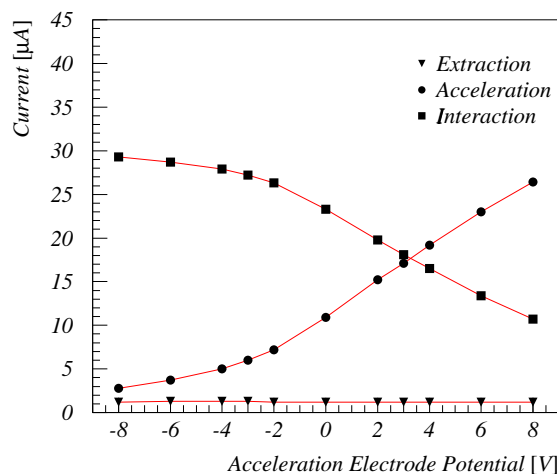
Figure 4.16: *Detail of leakage current distribution. A very minor change in potential by only a few Volts changes the distribution of leakage current between adjacent electrodes.*

explained by slow electrons in the vicinity of both electrodes. Electrons from the beam, which have almost the full kinetic energy in this region are not affected in such a strong way.

The potential of the *interaction electrode* is put to ground potential and need not be varied. The difference between ground potential and the cathode potential gives the electron beam energy, which can be chosen freely.

Applying a positive potential behind the interaction region on the *shielding electrode* and/or the *collector* reduces the leakage currents. Even though for potential uniformity inside the interaction region, a slightly negative shielding potential is optimal, it can be seen from the measurements in figure 4.17 that a positive potential is needed for good results. Because of this, the intersection with the ion beam, where the residual fields should be minimal, had to be shifted closer to the cathode side of the interaction electrode than originally anticipated. Similar to the observation with the acceleration electrode explained above it can be seen that putting the shielding electrode 5 V more positive than the interaction electrode shifts leakage current from the interaction to the shielding electrode. This suggests that between the two electrodes, electrons of a few electron volts exist which are affected by potential changes in this range.

The variation of the *collector* and *repeller* potentials can be seen in figure 4.18. Applying positive potential to the collector improves the leakage currents, whereas the potential of the repeller has only very limited, regional importance. Only when on very negative potential, the repeller shows no current. When becoming more positive, the repeller shows current of opposite sign to the other electrodes, being a source of electrons. This indicates that at these beam energies secondary electron emission from the repeller exceeds the amount of primary electrons impinging on the surface. As will be shown later in this section, the yield of secondary electron emission can indeed exceed unity considering the angle of impact on the repeller prism and the energies
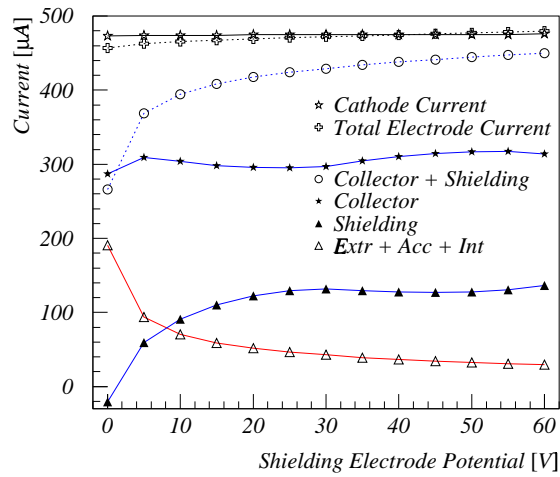
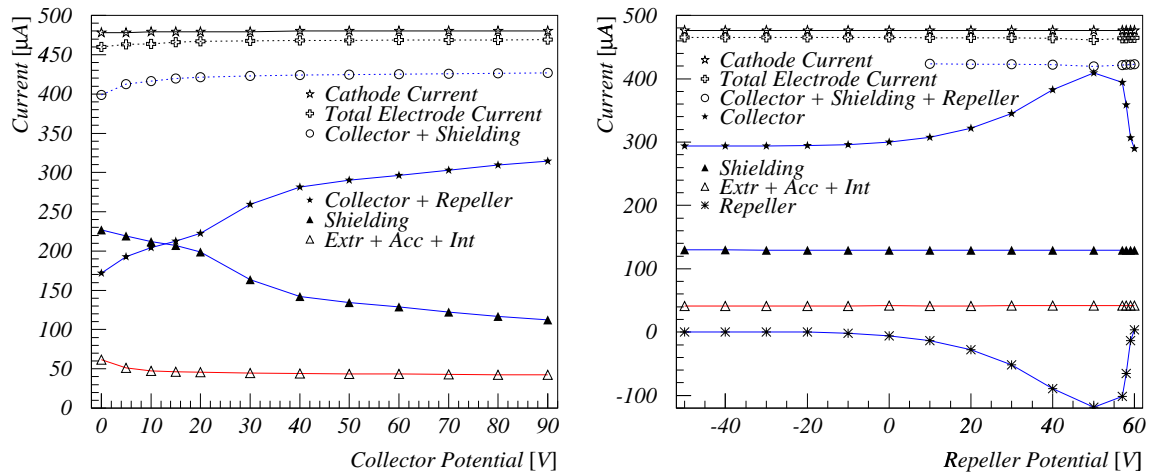Figure 4.17: *Effect of varying the shielding potential.*

Figure 4.18: *a) left: effect of varying the collector potential b) right: effect of varying the repeller potential.*

involved. At a repeller potential of 50 eV, the electron beam hits the collector at a kinetic energy of 100 eV. The reason why at a repeller potential of 60 eV no current is seen is because the neighbouring collector is on the same potential and does not sweep the electrons away from the repeller. Negative current can even be seen on other electrodes, although less pronounced. (The variation of shielding potential in figure 4.17 shows negative shielding electrode current at small potentials applied.)

Leakage current

The remaining problem and main uncertainty lies in the occurrence and origin of the leakage current seen in the test measurements.

A discrepancy between the simulation and the actual beam size and appearance can be ruled out, as the results of two independent simulation codes agree quite nicely.

Stray magnetic or electric fields also constitute a possible cause of concern. The effect of these fields can be considerable, as seen from the compensation coil measurements shown in the next section. The test chamber in Heidelberg is equipped with StarCell ion pumps which produce a field much smaller than the earth field at the position of the electron beam. Only the inhomogeneity of the fringe field could be held liable for any significant disturbance. The fact that the same leakage currents exhibit in the trap chamber in Israel, where no ion pumps are used rule out negative influences of stray fields to a large extend.

As already hinted at during the discussion of the electrode potential settings, a likely explanation can be derived with the help of secondary electron emission from surfaces struck by the beam.

First of all, the amount of secondary electrons created in the trap can be quite significant. In figure 4.19, taken from [97] the yield is plotted for several metals, normalised to a maximum yield $\delta_{max} = 1$ at energy $E_{P(\delta_{max})} = 1$. The inlay shows the characteristic yield as a function of the energy of the primary electrons. From this figure as well as from data quoted in [97], $\delta_{max} = 1.3$, $E_{P(\delta_{max})} = 400$ eV, $E_P^I = 120$ eV and $E_P^{II} = 1400$ eV for iron [98, 99] and $\delta_{max} = 0.9$, $E_{P(\delta_{max})} = 280$ eV for titanium [100], a yield of about 1 can be estimated for the collector with a 50 eV beam, when the impact energy on the collector is 110 eV, less for the titanium electrodes. Note that these data are measured for normal impact of the primary electrons. With the primary electron beam striking at an angle, the yield can increase significantly. No data for iron and titanium is given in [97], yet an increase by about a factor of two is possible. This is sufficient to explain the current of opposite sign on the repeller in some special cases, indicating a yield larger than 1.

The energy range of the secondary electrons extends up to the energy of the primary electron beam. Usually a sharp maximum exhibits at the energy of the primary beam due to elastically scattered primary electrons. With lower energies, inelastically scattered primary electrons contribute, at lower energies also emitted, truly 'secondary' electrons, that usually dominate the overall yield. For simplicity, all electrons returning from the surface will be called secondary electrons regardless of their origin and creation.
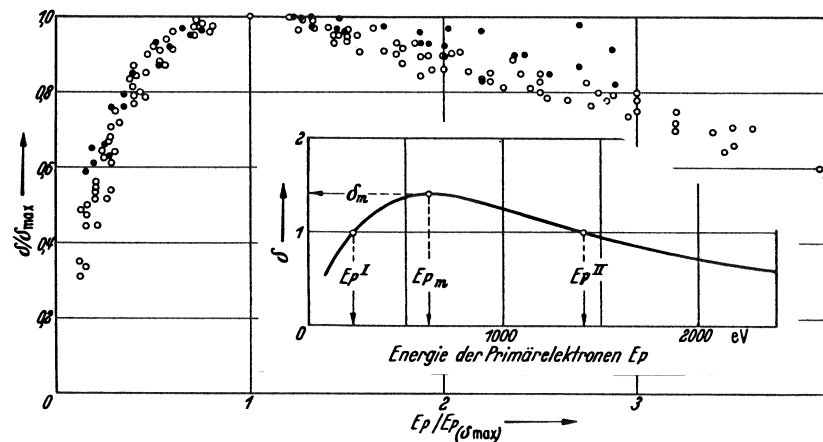
Figure 4.19: *Secondary electron yield normalised to a maximum yield $\delta_{max} = 1$ at energy $E_{P(\delta_{max})} = 1$. Combined data for 14 different metals taken from [97]. Inlay: yield as a function of primary electron energy; definition of parameters.*

Electrons originating at the collector with energies up to the primary beam energy can backtrack towards the cathode. On the way they will loose energy and finally either turn around to the collector again or bump into one of the electrodes on the way. The latter is more likely as not only do the secondary electrons lack the defined directionality of the accelerated primary electrons, but also does the space charge of the beam repel them easily towards the electrodes at those low energies.

The measurement shown in figure 4.16 is clear evidence for the existence of low energy electrons in the region between the acceleration and interaction electrodes. Secondary electrons can explain this observation.

Ionisation of restgas atoms or molecules could also contribute to the leakage current. Electrons created in these reactions get repelled to the electrodes, ions can be trapped in the space charge potential similar to an electron beam ion trap. This could ultimately lead to a breakdown of the balance of charge repulsion and overfocussing needed for the beam guidance.

At the current densities found in this setup ($< 1\text{mA/cm}^2$), this effect is not expected to be dramatic.

With secondary electrons being the most likely reason for the occurrence of leakage currents, one can conclude that the electron target is working properly. It has to be taken into account however that an unknown amount of slow electrons are also present in the interaction region where the ion beam traverses.

4.3.4 Work function correction and cathode bias

When dealing with low energy electrons, electrode potentials need to be carefully corrected for differences in work function of different types of materials. In our application with all electrodes made from titanium, the cathode needs to be put at an offset. This
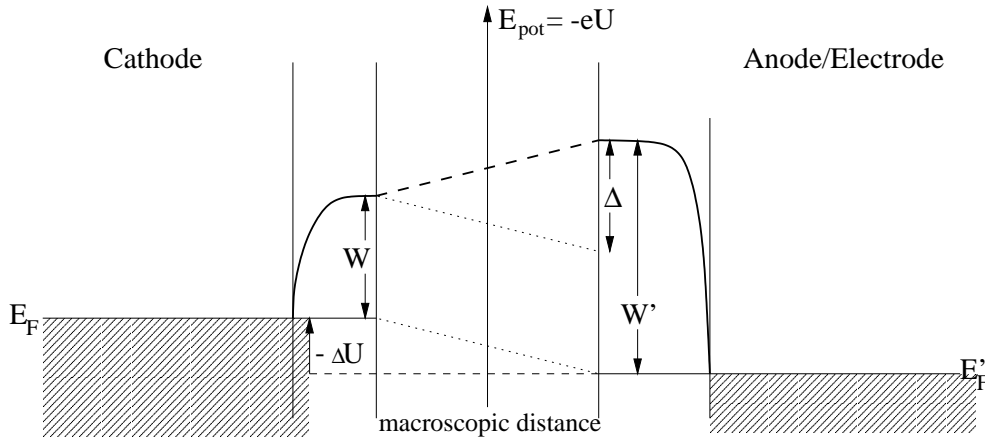
Figure 4.20: *Simplified model of two connected metals with different work function. With a negative bias applied to the cathode, the Fermi energies shift and the potential difference between the cathode and anode decreases.*

correction is most critical with respect to the field forming shields because of their proximity to the cathode surface.

In figure 4.20, the situation of two connected metals is shown. If two metals are connected, their fermi energies equal. With no additional potentials applied, an electron emitted from the cathode sees a potential barrier towards electrodes with higher work function.

Theoretical values for the work function are 4.5 eV for the titanium electrodes [101] and about 2 eV for the cathode at operating temperature. Thus the cathode needs to be biased about 2.5 V *negative* with respect to the other electrode values. An applied potential shifts the fermi level and a current will start to flow when both vacuum energy levels are equal.

Due to the Maxwellian distribution this onset starts even earlier, as some electrons in the high-energy tail of the distribution will have enough energy to overcome a certain barrier.

Experimentally, the situation shown in figure 4.21 is seen. Here, the cathode is held at -50 V (dashed line) and each type of shield is varied individually. The onset of current is seen when the cathode is about 2 V *positive*. Using the theoretical work function values, this would correspond to a barrier of about 4.5 eV! Also shown is the potential where the onset of current is expected from the above theoretical considerations.

This measured onset of current cannot be explained by the high-energy tail in the electron energy distribution: To estimate the current seen due to high-energy electrons that can overcome a certain barrier, the following formula is used [94]:

$$f(W_0) = \frac{A_{W_0}}{A_{tot}} = \frac{2}{\sqrt{\pi}} \sqrt{\frac{W_0}{kT}} \, e^{-W_0/kT} \quad .$$

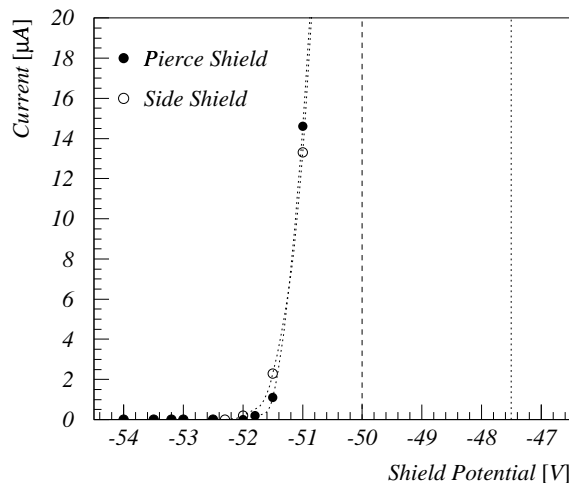Here, A_{W_0} denotes the amount of electrons above a certain threshold energy W_0, while

63

Figure 4.21: *Measurement of leakage current on the shields as a function of shield potential. The cathode is held at -50 V. Current starts to set in when the cathode is about 2 V more positive than the shields. From theoretical values of the work function, the onset is expected at a shield potential value of about -47.5 V, where the cathode is 2.5 V positive.*

A_{tot} is the total amount of electrons of a Maxwellian distribution corresponding to temperature T.

At an operating temperature of 1050°C, $kT \sim 100$ meV, the cathode can provide a current density of up to 10 A/cm^2 [86]. For the cathode used, a relative fraction of electrons $f(\text{W=2eV})$ are able to provide about 50 A current.

This current is generated by electrons with energies exceeding the work function of the cathode. Of these, the ratio of electrons with energies high enough to overcome an additional barrier Δ is given by $f(W_0 + \Delta)/f(W_0)$.

In our case with a cathode work function of 2 eV and a barrier towards the shield of 3.5 eV (work function difference plus additional bias, the situation of a shield setting to -51 V in figure 4.21), this ratio is about 10^{-15}, thus a combined current on the shields of about 0.05 pA is expected. The measurement provides about 30μA.

Another discrepancy can be anticipated from the strong effect shown in the simulation of figure 4.22. When using the cathode at about 2.5 V positive with respect to the shields to avoid leakage currents, the barrier between cathode and shield is nominally 5 eV. The negative shield constricts the emission to the centre of the cathode surface; the perveance of this arrangement and thus the current is about a factor of three smaller than in the ideal case. However, measuring the perveance with this setting to avoid leakage currents (cathode 2.5 V positive) yields a value that nicely matches the perveance simulated.

A possible explanation for this is that the work function difference is not as big as nominally expected. Without any work function difference, electrons with energies exceeding 3 eV can give rise to a current for the above mentioned setting (cathode
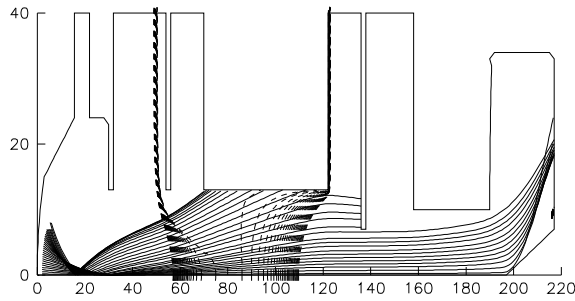
Figure 4.22: *In this extreme simulation, the cathode is set 5 V more positive than the shield.*

at -50 V, shield at -51 V). In an ideal geometrical situation, where all electrons go to the shield rather than get extracted to other electrodes, this current can be as high as 2.5 mA. As the work function difference increases, this value gets rapidly smaller and smaller, with 1 eV work function difference this value is 0.2 μA, with 2.5 eV the above mentioned 0.05 pA. The current measured in this situation of about 30 μA could well be described.

An additional bias not taken into account can have the same effect as a different work function. Thermo voltages can attribute only to a very small degree towards an additional bias. A smaller work function difference may arise if the cathode has a higher work function due to imperfect activation. As the activation cycle was performed according to recommendations by the manufacturer and the cathode has been operated for some time, a dramatic deviation from the theoretical work function is not expected. A lower work function of the shields can be explained by the fact that a layer of barium oxide has formed evaporatively from the cathode. Dispenser cathodes are known to release barium oxide and other impregnants. This layer could lower the work function of the shield electrodes similarly to the cathode's.

The correct bias is not only necessary for a proper realisation of the simulated beam characteristics but also for the determination of the true collision energy. With the problems mentioned above it seems that at this stage of test measurements no concluding answer can be given. The importance of a correctly adjusted difference in potential between the pierce shield and the cathode can be seen in figure 4.23. The series of plots show the cathode at a potential from 0.5 V positive to 0.5 V negative with respect to the pierce shield. The beam shape changes dramatically.

It can be seen that over a range of 1 V potential difference between cathode and shield, the beam height in the interaction region changes dramatically. In figure 4.24 the beam height is shown as a function of bias between pierce shield and cathode. The beam height also depends on the extraction electrode potential, albeit less pronounced. As this can counterbalance the effect on the beam height by the pierce shield setting, a measurement of the beam height can therefore not be used to explicitly determine the correct bias.

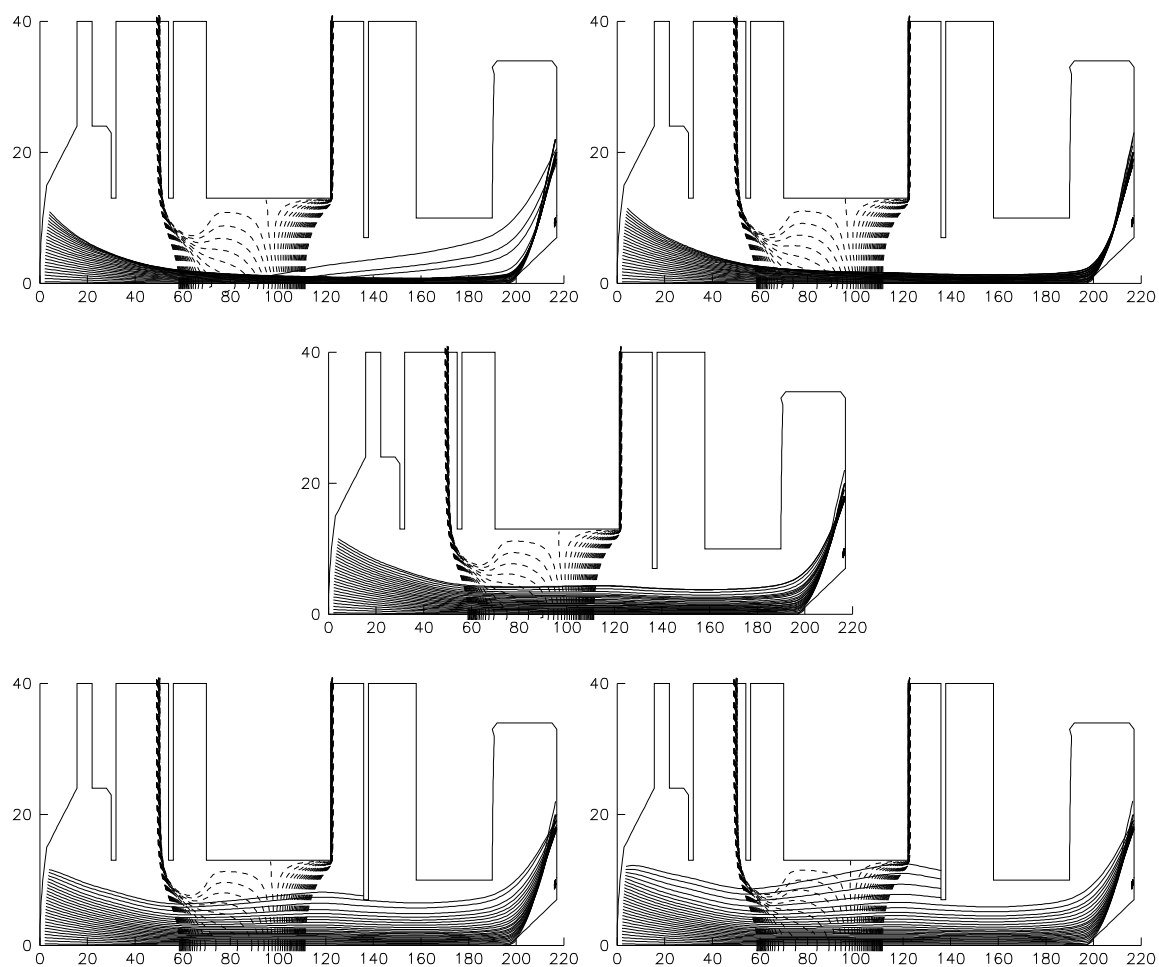With the electron target installed in the ion trap a possibility to measure the beam

Figure 4.23: *Effect of potential difference between cathode and Pierce shield. This series of plots starts with the cathode being 0.5 V and 0.25 V more positive (top), equal potentials (centre), cathode 0.25 V more negative and 0.5 V more negative (bottom). A possible reason for a potential difference could be not properly corrected work function differences of cathode and Pierce shield.*
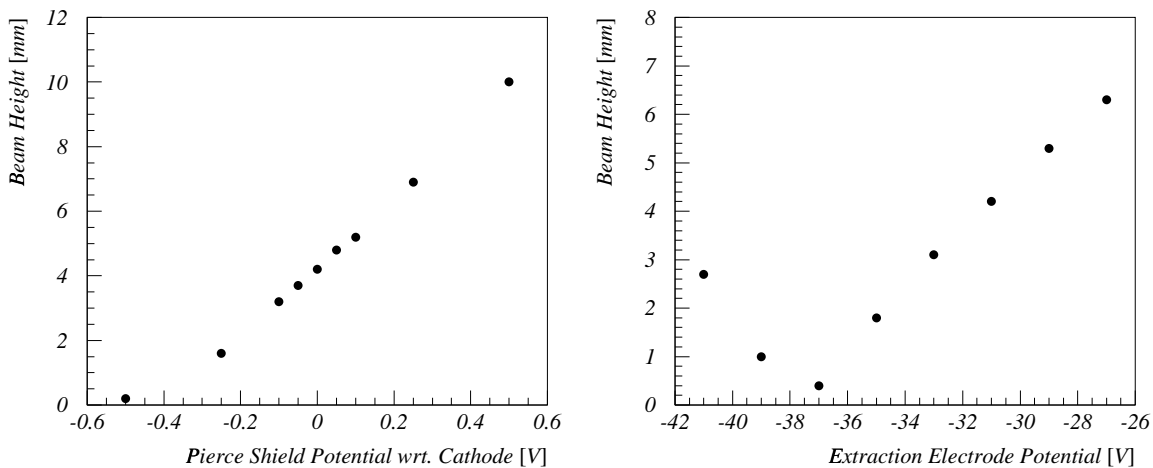
Figure 4.24: *Results from SLAC simulations showing the beam height at the position of the ion beam as a function of bias between pierce shield and cathode with extraction at -31 V (left) and as a function of extraction potential for a 50 eV beam with shields on cathode potential (right).*

height becomes accessible by scanning the electron beam through the ion beam. It is desirable however to see the influence of potential differences and possibly use this knowledge to establish the best values.

In figure 4.25, a series of simulation is summarised and the effect on two accessible parameters is shown. Each two-digit number in the matrix represents the result of one simulation in units of 0.1 mm and 0.1 μP, respectively. Only the settings with acceptable beam profile are plotted; with too little extraction (more negative extraction electrode potential), overfocussing occurs while the other extreme is too much coulomb repulsion due to too much extraction, resulting in the beam hitting the shielding electrode.

Setting the shield more negative than the cathode additionally focusses the electron beam. This effect, also seen in figure 4.23, can be counterbalanced by setting a higher extraction potential difference. A smaller beam height and a higher perveance results. For each shield to cathode difference, that is for each row in figure 4.25, the beam profile can be analysed in the interaction region, where the ion beam passes through the electron beam. Moving from left to right, towards more extraction, the electron trajectories are first at an angle towards the centreplane, and slowly change to an angle away from the center plane. The setting where the transition occurs is marked with a circle.

It is not known, however, how the potential of cathode and shield, once balanced, relate to the potential of the other electrodes. To determine the correct collision energy, the threshold of a known cross section must be used to compare to the measured data.
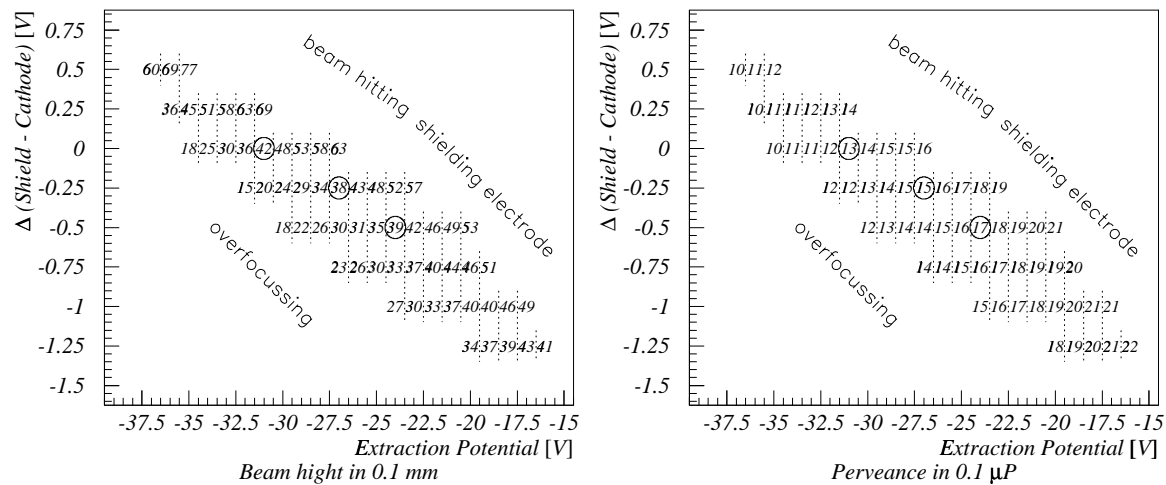
Figure 4.25: *Alternative potential settings and their effect on the beam height and perveance. Potential values are for a 50 eV electron beam.*

4.3.5 Influence of magnetic field correction

To study the influence of external magnetic fields and the necessity to compensate for it, correction coils have been added to the testbench. In figure 4.26 the results of varying the magnetic field in all directions are shown.

A very symmetric situation can be seen when applying a *field in horizontal direction*, moving the beam up and down. With zero correction, the 50 eV beam is centred in vertical direction, and about 90% of the current is seen on the collector and the shielding electrode. With an applied field of about 1 G (corresponding to an applied coil current of about 3.3 A), the current is increasingly seen on the interaction and especially on the acceleration electrode. From simulations it is expected to see most of the current on the interaction electrode at around 1 G. With stronger magnetic field, the acceleration electrode is expected to get most. In the measurements the acceleration electrode dominates in leakage current over the interaction electrode throughout the whole scan. One possible explanation why so much current is seen on the acceleration electrode comes in with the possible occurrence of secondary electrons. Slow electrons produced in this process are swept away by the most positive electrode nearby. In principle, this would be the acceleration electrode to the cathode side and the shielding electrode towards the collector. Depending on where the beam strikes the interaction electrode, one or the other gets to see more of the leakage current. With high field, the acceleration electrode is hit directly. Because of the direction of the electron beam on the test setup in Heidelberg being north-south, the horizontal component of the earth field is in ion beam direction and does not deflect the beam up or down; this explains the symmetric distribution about the origin.

A less symmetric situation arises when deflecting the beam in horizontal direction by adding a *vertical magnetic field*. At coil currents between about -4 A and 8 A, only
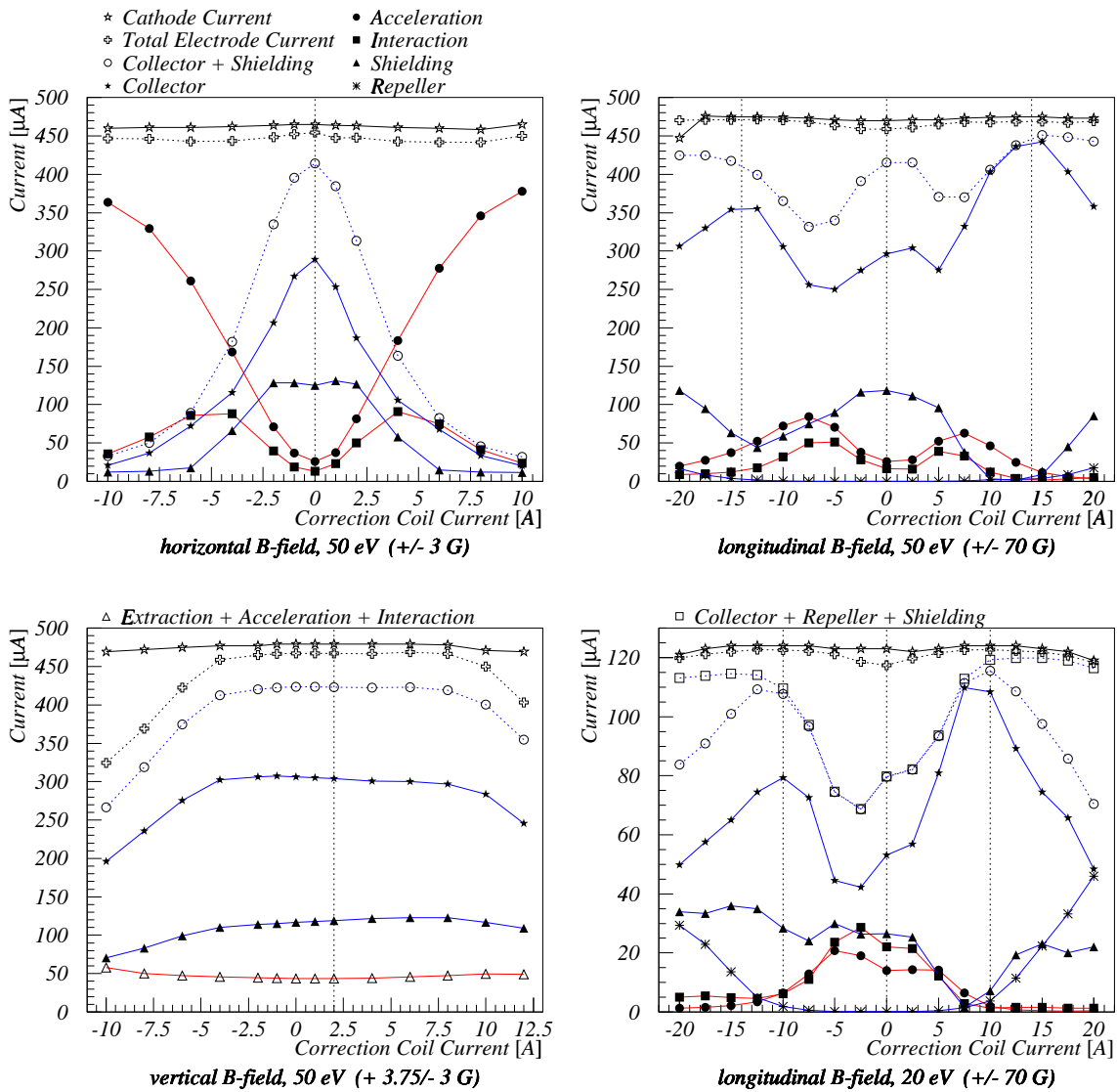
Figure 4.26: *Effect of applying magnetic fields; measurements in Heidelberg: the orientation of the magnetic field, the beam energy and the range of the abscissa in Gauss is given below each plot.*

little change is observed in the leakage currents. Within these boundaries, the beam still hits the collector. As the currents are outside these values, missing current is observed. The centre of the plateau is at about a current of 2 A which suggests that a field of about 0.6 G is present and needs to be corrected for. This value compares well with expectation from the vertical component of the earth field of about 0.5 G for Heidelberg with a geographic latitude $\Phi = 49°$.

Applying a *magnetic field in longitudinal direction* confines the electron beam, a fact that is commonly used in electron gun devices. With a 50 eV beam it can be seen that without an applied field the leakage current situation is quite good. With a 20 eV beam however, the situation is less good, only an applied field leads to a significant portion of the current to be seen on the collector. The fact that from about ± 12 A onwards the electrons start to hit the repeller prism is a clear indication how the electrons are forced to follow the magnetic field lines. In this regime the beam profile is not expected to exhibit the shape known from the simulations. The leakage current seen on the shielding electrode and the repeller results from directly scraping the electron beam. For both electron beam energies, the collector current exhibits a periodic behaviour, for 50 eV with maxima at about -14, 0 and +14 A coil current, less pronounced for the 20 eV beam, where no pronounced maximum is found around the origin besides the two maxima at ±10 A. An explanation for this could be the helicoidal motion of the electrons in the magnetic field. The lead of the helicoidal motion, also called the cyclotron length, of 50 eV electrons in a field corresponding to 14 A coil current is 3.6 cm, for 20 eV electrons and 10 A current 2.7 cm. This is in the correct range as the distance from the middle of the interaction region to the collector is 3.1 cm. The periodic behaviour could thus be interpreted that with zero current, the beam hits the collector, with rising coil current, the helicoidal motion shifts the beam away from the collector centre until, at the maxima, one full circulation of this helicoidal motion is accomplished.

In comparison, measurements at the setup in Israel are shown in figure 4.27. Here, the orientation of the electron beam axis is at an angle of 45° to north-south, therefore also a horizontal magnetic field is needed for compensation. Due to the geographic latitude of about 32°, roughly 0.3 G is needed in horizontal as well as in vertical direction, corresponding to about 4 A coil current. This matches nicely the offset seen in both magnetic field scans in figure 4.27. An interesting effect can be seen when performing these measurements with the deflector in down position, see figure 4.28: steering the beam horizontally with a vertical field bounces the beam off the deflector housing. After a decrease in collector and shielding electrode current when applying more and more current of negative polarity similar to the situation in figure 4.27, these currents start to increase again. The side wall of the deflector housing is only about 3 mm from the electron target frame, so the most likely explanation is that the electrons are reflected from this vertical surface back onto the collector.

A few comments should be added regarding the necessity to compensate the magnetic field, the behaviour of the electron beam at low energies and the possibility to use longitudinal fields to guide the beam. From the tests performed the necessity to com-
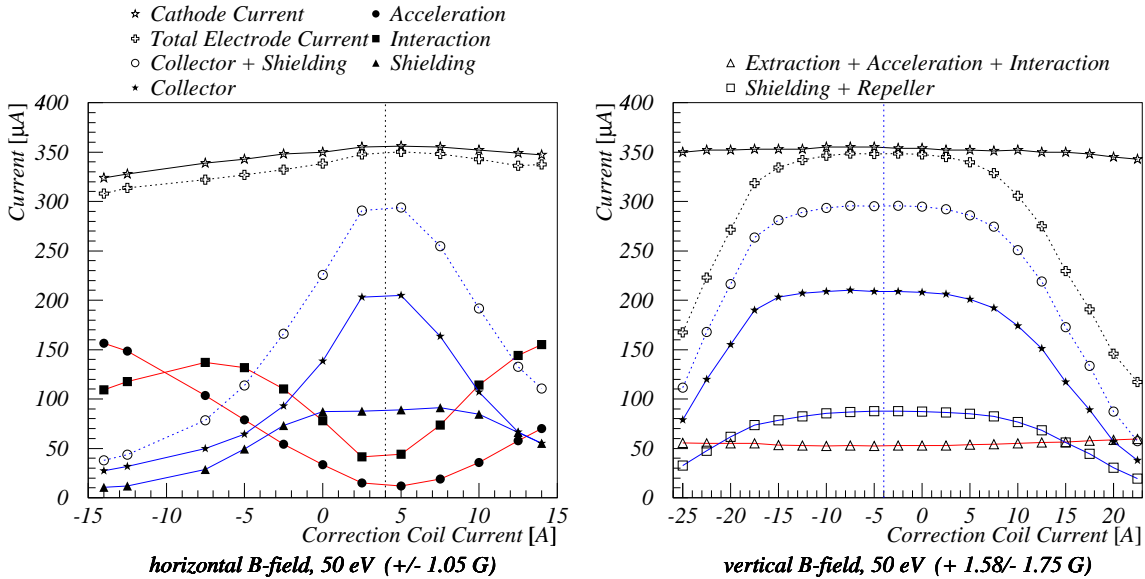
Figure 4.27: *Effect of applying magnetic fields, measurements in Israel: the orientation of the magnetic field, the beam energy and the range of the abscissa in Gauss is given below each plot.*
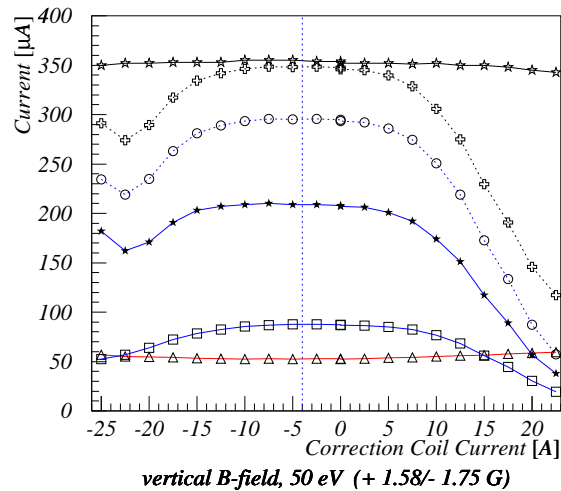

Figure 4.28: *An interesting effect when applying a magnetic field in vertical direction, steering the beam horizontally: This measurement was done with the deflector in down position. At large currents of negative polarity, an increase in current on the shielding electrode and the collector can be detected. This can be attributed to the beam bouncing off the deflector housing which is quite close to the frame of the electron target.*

pensate the effect of the earth magnetic field can clearly be deducted. Measurements of the required magnetic correction field compare well with predictions from simulations. Compensation is especially critical for low electron beam energies, as can be seen from the measurements at 20 eV. Simulations show that with adverse orientation of the electron beam, the earth magnetic field can make a 5 eV beam completely hit the interaction electrode; see figure 4.7. With correction of the fields, the residual stray magnetic field measured with a teslameter was more than a factor of 10 less than the earth field. The situation of a 5 eV electron beam in this residual field scales to a 500 eV beam in the earth field. Simulations showed no effect of the earth field on an electron beam of this energy. With properly corrected magnetic fields, the behaviour of the electron beam at low energies should not fundamentally differ from faster beams. Introducing a longitudinal field to confine the electron beam does not help in our case as it is not compatible with the approach of using the balancing effect of space charge repulsion and overfocussing to form the beam, where the electrons start with a significant angle against the magnetic field lines. Using an beam designated for magnetic guidance of the electrons leads to problems with the beam storage as deflections of the ions due to the magnetic field comparable to acceptance angles encountered in the trap appear already at magnetic fields of a few tens of Gauss.

4.3.6 A first beam profile measurement

The measurements and tests as presented up to now cannot completely confirm the correctness of the simulations. The non-vanishing leakage current at all settings could be due to a much wider beam scraping the electrodes. Although there are indications in the details that show that the leakage current is caused by slower electrons and not the beam electrons a different approach to verify this assumption is desirable. Imaging the electrons and thus measuring a beam profile is the obvious choice, although technically very challenging at these electron energies.

In magic eye tubes of radio receivers from the late 30's to the early 60's materials were used that luminesce on impact of electrons in the energy range of usually between 100-300 eV. There is one material however, manganese activated zincorthosilicate or Willemit, that gives luminescence light from about 10 eV onwards [102].

In an attempt to utilise this material to detect slow electrons, thin blocks of titanium were complimentary coated by Leuchtstoffwerk Heidelberg, a company which was founded on the discovery of this particular material. Since then they have moved towards other fluorescence light applications, so little is known about the properties of the material used. (with respect to grain size, layer thickness, spectral properties and energy dependence).

This block was then placed standing on the interaction electrode, towards the collector end, facing the cathode. Through the viewport, its surface could be monitored.

It turned out to be very much a single shot experiment with the luminescence screen dying rather quickly, probably due to heat and electron bombardment. To minimise exposure, the electron beam was chopped off by default. Still, the lifetime was maybe 20-30 minutes only. With the help of specially selected filters matching the emission
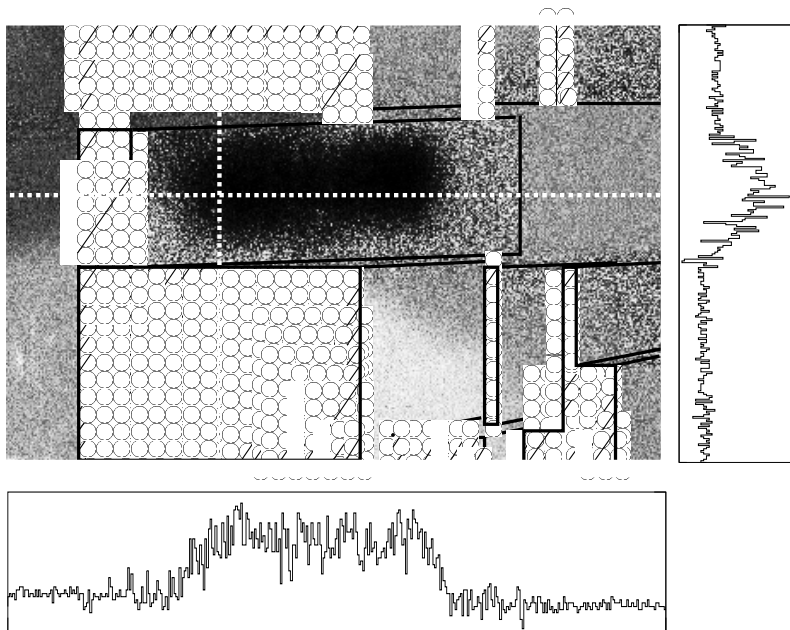
Figure 4.29: *CCD image of the fluorescence screen; beam profile measurement of a 50 eV electron beam. To guide the eye and to show the geometry, the edges of the electrodes are traced. The view is at an angle, towards the collector, which cannot be seen; the cathode is to the right, outside the picture frame. The screen can be seen sitting on the interaction electrode. To the right, the acceleration and extraction electrode can be seen. Also included are dotted lines which correspond to the cuts shown to the side and on the bottom.*

properties as given by [102] to cut down the overpowering background from the bright cathode the beam profile in figure 4.29 was observed with a peltier-cooled ccd camera. This image was taken towards the end of the screen lifetime, where starting from the middle and moving towards the sides, the screen gradually extinguished. Earlier, un-recorded images looked much more even without the necking in the middle of the spot. Still, with the limited data at hand, some conclusions can be drawn: The beam centres nicely between the interaction electrodes, being clear off the electrodes itself. From the cuts in figure 4.29 and the dimensions of the screen, the dimensions of the beam can be roughly estimated. A very rough FWHM measurement gives a beam of 50 mm width and 7.5 mm height. This numbers should be treated with caution, as it is known that with magic eye tubes, charge built-up can occur if the transverse conductivity of the luminescence layer is not big enough. This can ultimately lead to so-called voltage spots on the screen. In our case, charge built-up can lead to a local distortion in electric field in front of the screen, not necessarily completely repulsive in nature. A much larger beam spot can result.

4.4 Summary and conclusions from stand-alone operation

An electron target with a sheet beam has been built based on agreeing simulations from two different software codes. An electrode arrangement with a convex dispenser cathode is used that confines the electron beam without the help of longitudinal magnetic fields.

In first tests, the measured perveance describing the current yield at different electron energies, compares well with simulated values. The current collected after the interaction region where the ion beam is planned to pass through the electron beam, however, is less than the current coming from the cathode. Leakage currents constitute a significant fraction of the cathode current, especially at low electron beam energies. A conclusive assumption of the nature of this leakage current has been found in secondary electrons originating at the collector with energies high enough to allow for backtracking towards the cathode. Losing kinetic energy on the way, these decelerated electrons finally end up on the electrodes, giving rise to an observable leakage current. Evidence for this assumption of slow electrons ultimately leading to these currents could be found by changes in the leakage current distribution caused by changes in the potential of specific electrodes. These changes of only a few eV are not expected to have a dramatic effect on the shape of the electron beam, but do indeed influence slow stray electrons in the vicinity of the electrodes concerned. Another indication that there is no underlying conceptual error in the simulated behaviour of the electron beam could be found with first attempts of measuring a beam profile. These result in an electron beam well centred between the electrodes. A final answer to this question can be found in electron-ion collision experiments. Once a thin ion beam can be efficiently stored, this beam can be nicely used to determine beam profiles and a measurement of known cross sections can be used to infer which fraction of the electron current does partake in ion collisions.

The effect of the earth magnetic field has been simulated and a necessity for correction especially at low electron energies could therefore be anticipated. Measurements of current distribution with applied magnetic correction fields agree nicely with those expectations. A direct measurement of the residual field verifies good compensation that enables the beam to be operated at low electron energies without difficulties.

One problem remains the uncertainty about the correct cathode bias with respect to the electrodes due to an expected difference in work function. This offset is especially critical between the cathode and the surrounding shields. The offset used for these tests and the onset and magnitude of the leakage current on these shields does not agree with theoretical expectations. A possible reason could be the speculative reduction of the shields' work function by the formation of a dipole layer similar to the cathode's due to cathode outgassing. A more detailed analysis of the shield leakage current behaviour at smaller cathode temperatures might improve the understanding. Additionally, with meaningful beam profile measurements available, a comparison with given simulation results for different bias conditions is possible.

Chapter 5

Electron Beam and Ion Trap

Upon completion of the above mentioned test measurements, the electron target was moved to Israel and installed in the beamline at the Weizmann Institute.

After completion of the more complicated electron target support, the schedule for the initial tests was to first confirm the measurements from the test setup and then check the compatibility of the electron target with the ion trap.

The immediate problem turned out to be the ion beam storage. With the electron beam operating, it was no longer possible to store an ion beam. In the following sections, the reasons for these difficulties will be exposed and the remedies found will be explained. Then, first measurements of electron-ion collisions will be presented as a proof of principle.

Stand-alone tests without an ion beam stored in the trap chamber confirm previous results from Heidelberg.

5.1 Electron target installation in trap

For use with the electron target where with the hot cathode outgassing of the electrodes close to the cathode surface occurs, additional pumping elements are introduced into the vacuum chamber. Two getter modules of type WP 750[1] are placed to the side of the electron target, between the entrance mirror support bracket and the frame of the electron target. This ensures good pumping capabilities due to close proximity to the hot surfaces.

The support for the electron target is placed on the breadboard and can be seen in figures 5.1 and 5.2. The electron beam has to be mounted in a way to make a scanning of the electron beam through the ion beam possible. This is not only important for an optimisation of the ideal overlap of the two beams but also to allow for a later implementation of the animated-beam method [48, 49] for a stored ion beam.

The movable mounting makes the task of supporting the electron target with the necessary potentials for 9 electrodes, high power heating for the cathode and cooling

---

[1]manufacturer: SAES Getters

water quite complicated. The movement of the electron target is achieved in a similar way as the deflector is made retractable: linear ball bearings guide the electron target on 4 ground stainless steel rods. These ball bearings sit on a bracket from which the electron target is suspended. The two water tubes for the in- and outflow are
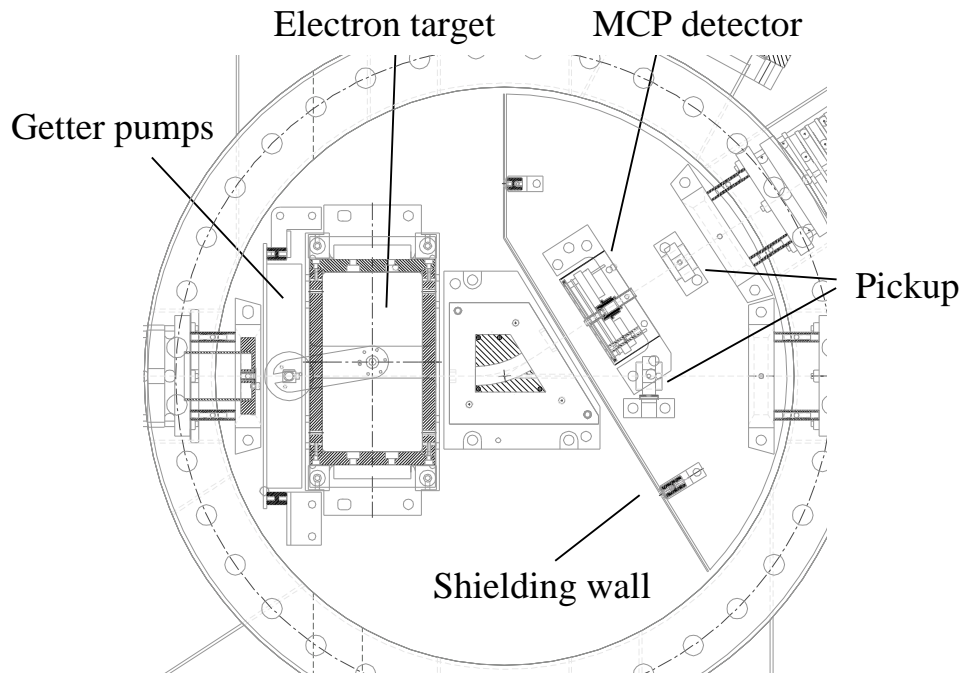

Figure 5.1: *Electron target installation in the Bent Electrostatic Trap, top view. Also visible are the getter modules between the electron target frame (hatched area) and the entrance mirror support. The shielding wall dividing the chamber is also drawn.*

arranged concentrically and lowered through a a $2\frac{3}{4}$" feedthrough on the cover of the trap chamber. As these tubes provide the potential for the cathode, the connection to the support bracket has to be made electrically insulated. A linear manipulator makes these support rods retractable. The wires for the electrode potentials and the heating power run alongside the water tubes, also electrically insulated. They are fed through 3 mini conflat wire feedthroughs arranged perpendicularly to the water tubes on a double-sided conflat. A ceramic break serves as an insulator between the actual water line feedthrough flange on the very top of the arrangement and the rest of the grounded trap chamber.

Details of the installation can be seen in the pictures of figure 5.3. In the top row, the electron target is installed in the trap. The rods can be seen that guide the movement of the electron target and the deflector, respectively. The deflector plates are hidden inside the grounded shielding. On the right, the apertures for the ion beam storage on the straight and on the bent section can be spotted. In the second row, the insulated

Manipulator

Cooling water connections

Electrical connections

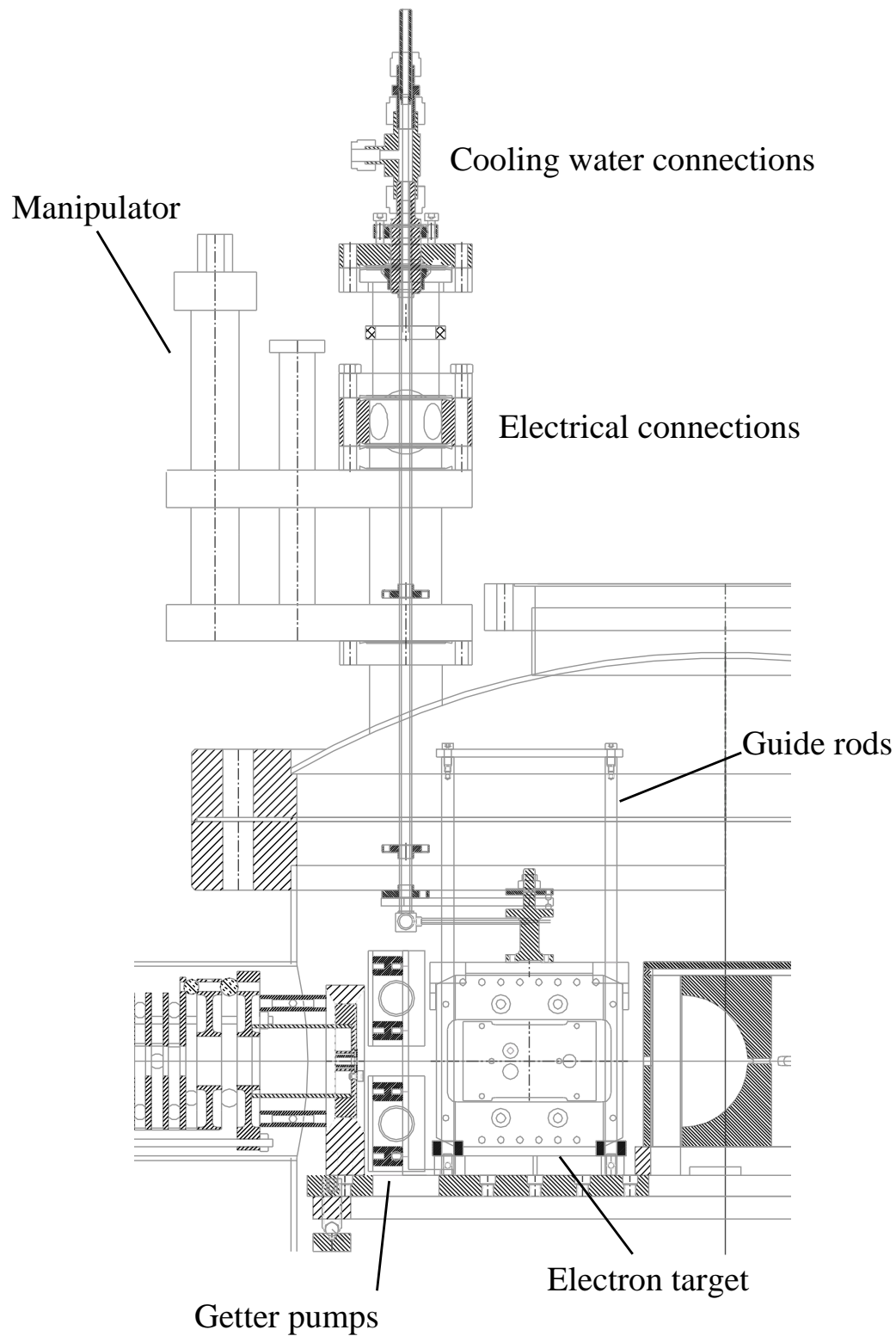Guide rods

Electron target

Getter pumps

Figure 5.2: *Side view of the electron target installation showing the feedthrough arrangement.*
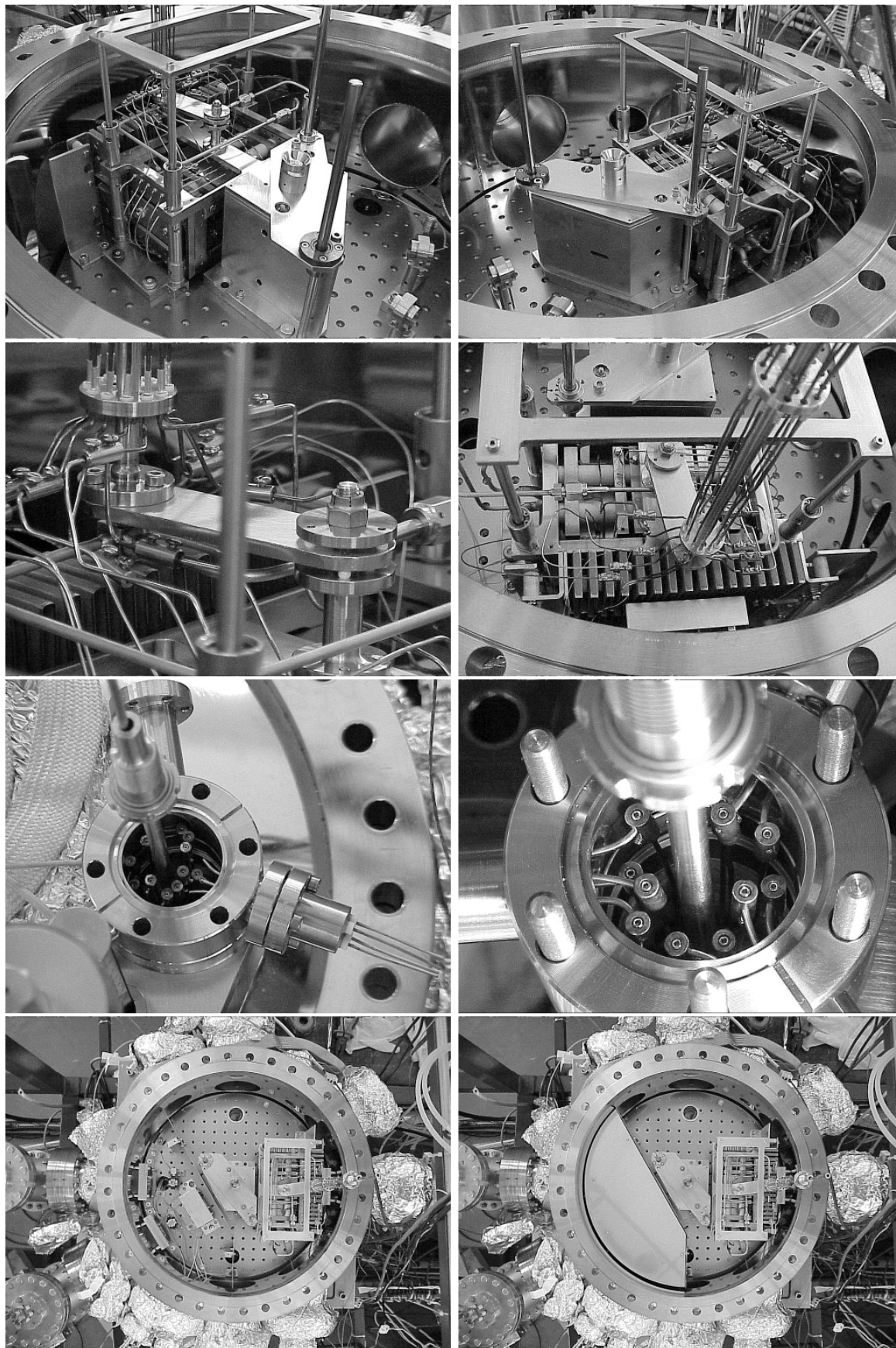
Figure 5.3: *Pictures of the electron target installation in the trap chamber.*

lever that connects the supporting water tubes to the support bracket is visible. Note also the proximity between the electron target and the getter module on one side and the deflector on the other side. In the picture on the right, the wiring alongside the water tubes is pointed out. These wires end above the manipulator and are joint with mini conflat feedthroughs by custom-made connectors, see third row of pictures. On the very bottom, the final state of the trap installation is shown. The MCP is mounted on the bent section and the shielding wall and cover is assembled. These shielding devices were added as results of first tests of the electron target in the trap environment, see section 5.2.2.

5.2   First observations

The first objective was to examine the effect of the electron target in operation on a stored ion beam, regardless of the ion species. For ease of operation, a 4.2 keV Ar^+ ion beam was used for these measurements.

The pure installation of the electron target together with the getter modules did not change the trapping condition for an ion beam. Storage of an ion beam when the electron target was not operated (cathode cold and no electrode potentials applied) turned out to be the same as before.

Lifetimes in the bent electrostatic trap were considerably shorter than in the linear trap under the same vacuum conditions. Mirror settings still needed to be optimised. Two major influences of the electrons could be found. Ion storage was undermined by charging of insulating macor[2] pieces inside the entrance mirror assembly and outside the trap. Secondly, electrons accelerated up to keV energies produced photon-induced background counts on the MCP detector outside the trap.

5.2.1   Insulator charging

It turned out to be impossible to store an ion beam when the electron target was operated. Several influences associated with the electron target could possibly account for this finding. In order to extract electrons, potentials need to be applied at the electron target electrodes which might have an influence on the stored ion beam. Heating the cathode also changes the environment, consequential outgassing might affect the ion beam. Then, electrons originating from the cathode might affect the ion beam stronger than anticipated from known cross sections. The influence of all these factors on the ion beam might be directly affecting the ions in the beam or change the storage conditions, indirectly affecting the ions. To specify the ultimate cause, the following series of test were made:

- cathode cold, no electron target potentials applied: no adverse effect on ion trapping. This indicates the installation does not affect the field configuration for trapping.

---

[2]Macor, machinable glass ceramic, registered trademark

- cathode cold, potentials applied: still trapping of ions, some effect on stored ions due to the residual field of electron target potentials, can be counteracted by slightly changing these potential values, see later in this section (5.2.3)

- cathode hot, no potentials applied: No influence on trapping conditions due to the heating. The vacuum level changes, especially when no bakeout of the chamber has been performed, and so does the lifetime, but the trapping still persists.

- cathode hot, potentials applied. As soon as electrons are extracted from the cathode, the trapping vanishes. Taking down the potentials again does *not* bring the trapping back.

Once the trapping condition was destroyed, it could only be restored by directing an unchopped ion beam into the chamber for several trapping cycles, without switching the entrance mirrors.

To see if the ions, the electrons or the interplay of the two are responsible for this behaviour, a similar set of tests was made where the ion beam was blocked before the chamber prior to applying electrode potentials and extracting electrons. In this case, the ions were put on a faraday cup in front of the deflecting magnet, then the electrode potentials applied. Before directing the ion beam back into the trap chamber, the electron target potentials were taken down again.

- cathode hot, potentials applied and entrance mirror switching while ion beam on cup. Again, the same as before: trapping is lost as soon as electrons are extracted. For restoring the trapping condition, the procedure mentioned had to be employed.

- cathode hot, potentials applied and entrance mirror *not* switching while ion beam on cup. No change in trapping condition, as soon as the ion beam is directed back into the chamber and the usual switching cycle applied, the ions are stored.

The same results were obtained regardless of the position of the electron target and the deflector. These results indicate a problem associated with the electrons and the entrance mirror potentials. The independence on the electron target position (in down position the ion beam is passing between the interaction electrodes and in up position the ion beam passes beneath the electron target) excludes charging of a badly connected part of the electron target itself as a possible reason for the problems seen. The independence on the deflector position rules out charging on the exit mirror side of the trap as a source of concern. The deflector in down position acts as an aperture for the injected beam, which is usually wider than the stored beam. Thus, a significant portion of the beam does not penetrate into the exit side of the trap which makes de-charging by the unchopped beam of parts on this side extremely unlikely.

SIMION simulations then performed showed that the residual field of the mirror electrodes, albeit small, can attract very slow electrons from the electron target region towards the positive high voltages on the mirror electrodes. These electrons are then trapped around the outermost high voltage electrode ($E1$). The outer turning point is
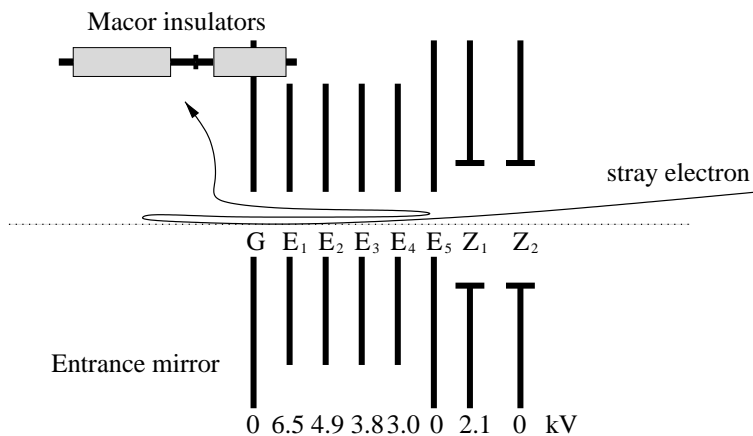
Figure 5.4: *Schematic drawing of the possible trajectory of a stray electron being attracted by the positive high voltage on the entrance mirror electrodes. Typical potential values are indicated in kV.*

several centimetres outside the mirror stack. Eventually the electrons are lost and hit the electrodes, the beam pipe and the macor pieces. See figure 5.4 for an illustration of this.

This hypothesis could be confirmed by experiments when the entrance mirror electrodes were switched individually. The ions were put on the cup, the mirror potentials prepared for the new switching scheme, the electron target operated for some time, the original switching scheme restored and the ion beam guided into the trap chamber again.

- As before, when no potentials are applied, trapping is conserved, with all potential switching, trapping is lost. The transition could be attributed to the two outermost electrodes, nominally on 6.5 kV and 4.875 kV respectively. As soon as these potentials were applied, trapping was lost.

This compares nicely to the results from simulation, as only in cases where these electrode potentials are applied, electron trajectories go beyond the outermost electrode. Only then a significant probability that electrons reach the unshielded macor insulators is expected.

Further simulations showed that there is a trapping configuration using only the three innermost electrodes ($E3$, $E4$, $E5$) with the two outermost electrodes ($E1$, $E2$) on ground potential. Electrons do not leak outside the mirror stack in this configuration.

- Using a configuration with the two outermost electrodes grounded, trapping is possible while the electron target is operating.

This result clearly indicates that charging of the macor insulator is responsible for the trapping problems seen. Once charged, the macor pieces deflect the incoming ion beam, which is no longer entering the trap inside the angular acceptance of the trap.
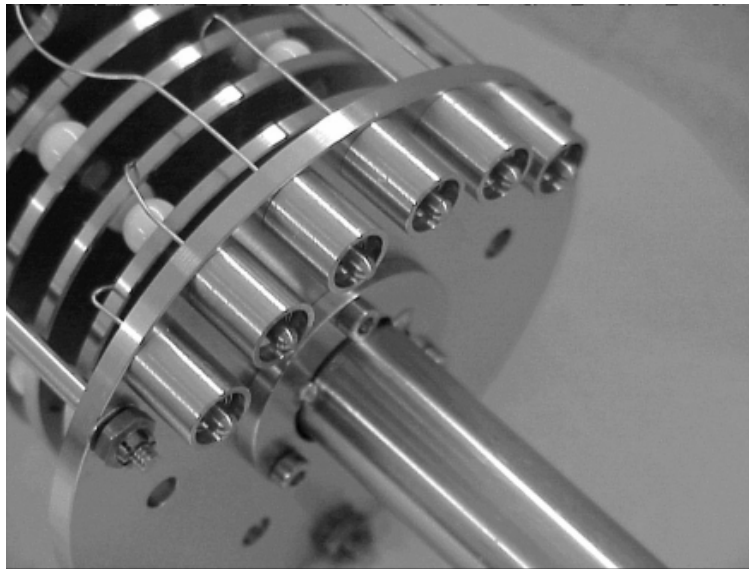
Figure 5.5: *Metallic cups shielding the macors on the mirror stack. Similar cups have been added to shield the other macor pieces. By comparing this picture of the mirror stack and the picture in figure 3.4, the changes can be seen. The drift tube can be seen on the bottom.*

To remedy this situation, a two-fold approach was chosen. The exposed macor pieces were remodeled to fit into metallic cups that shield almost completely the surface of the insulators (see figure 5.5). Additionally, a drift tube was added to the entrance mirror stack to avoid any residual influence on the incoming ion beam. On top of this shielding effort, an aperture was introduced at the support bracket of the mirror stack, together with another shielding tube between the bracket and the innermost, grounded Einzel lens electrode ($Z2$). A clamping ring inside the beam tube closes the gap between this electrode and the wall of the tube. This way, less electrons enter the mirror region, making charging less of a problem. Compare figures 5.6 and 5.7 to assess the changes made. With these changes, trapping is possible using the original mirror electrode settings while the electron target is providing electron current.

5.2.2 Electron-induced detector noise

When trapping conditions were studied in more detail using the neutral particle counts on the MCP detector outside the trap chamber on the extension of the straight section, additional background noise associated with the electron current could be seen. Again, this problem was examined without ions stored in the trap. With electron current drawn, the background rate was enhanced by a factor of 20-100.
The following observations were made:

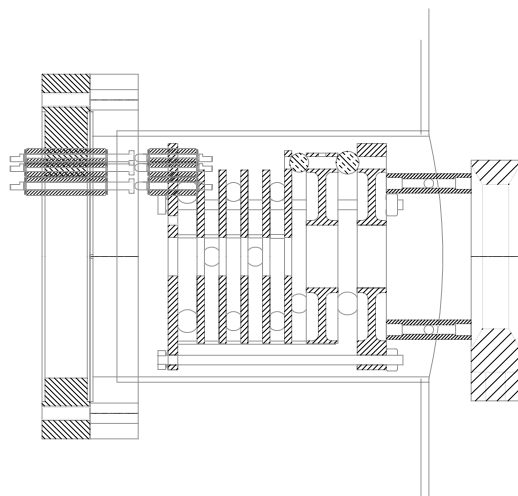- When no high voltage was supplied to the mirrors, this increase in noise was not
observed.

Figure 5.6: *Old entrance mirror design. Shown is the support bracket on the right with the mirror stack attached. This assembly is inserted into the 4" tube from inside the chamber. The pins for the high voltage connection attach to spring-loaded pistons supported from the double sided conflat on the left. From there, the wires lead to a feedthrough flange located on the 4-way cross to the left of the double sided conflat (not shown here). Note that the insulators are exposed to a certain degree.*
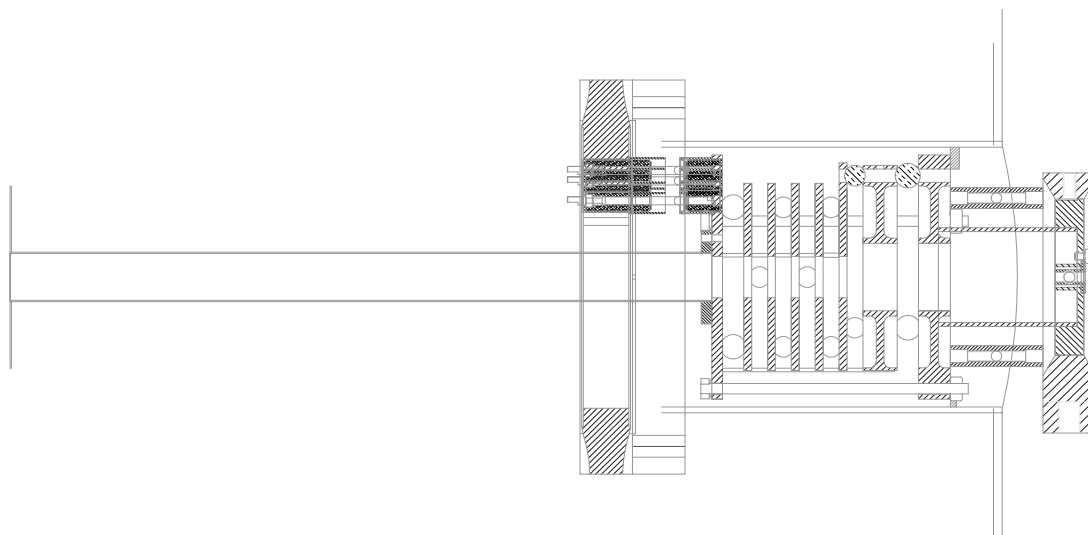

Figure 5.7: *New entrance mirror design. The different macor insulators can be seen almost completely enclosed inside metal cups. Inside the central hole of the support bracket, the aperture can be seen with the attached tube. The clamping ring is also schematically shown in front of the innermost electrode. The drift tube is long enough to reach to the entrance side of the 4-way cross to the left of the assembly shown.*

- With potential applied to the entrance mirror, a high noise level was observed, regardless of the potentials on the exit mirror. The same background rate was measured with the exit mirror on positive high voltage, on ground potential and on negative high voltage. This observation rules out charged particles leaving the trap and hitting the MCP detector.

- Even with the entrance mirror potentials on ground and the exit mirror potential on positive high voltage, the same background level was observed.

- In both cases with high noise level, moving the deflector in down position lowered the noise level significantly.

The assumption is that the mirror potentials attract stray electrons and accelerate them up to keV energies. If these fast electrons hit the metal electrodes, photons are created by bremsstrahlung. These photons can reach the MCP detector regardless of the potential of the exit mirror.
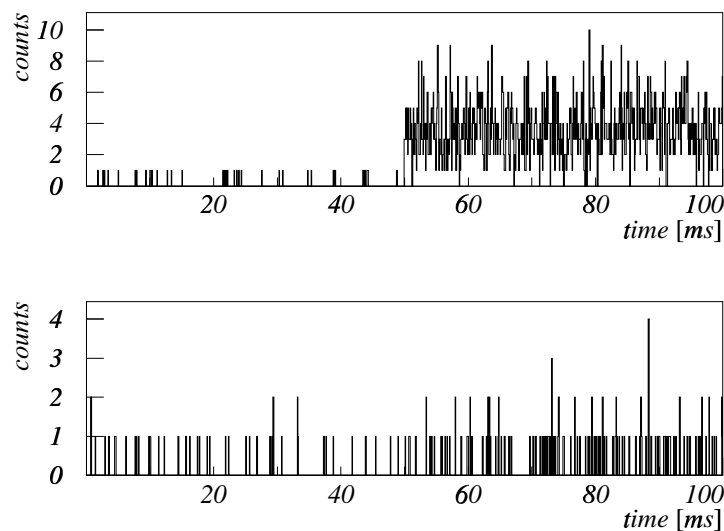
Figure 5.8: *Background level with electron beam off (0-50 ms) and 20 eV electron beam on (50-100 ms). The difference before (top) and after (bottom) installation of the shields. These data were taken with the same number of injections, deflector in up position, high voltages applied, 75 % heating power.*

Simulations by SIMION show a residual electrical field even with the above-mentioned shielding of the entrance mirror in place. If the deflector is in up position, the exit mirror also creates a residual field at the position of the electron beam. This field is smaller than the one created by the entrance mirror, so only if the entrance mirror potentials are not applied, will electrons be moving towards the exit electrodes. With

the deflector in place, it is less likely that the electrons will make their way to the exit electrodes, even more so because the residual field is screened. The deflector also forms an obstacle for the photons originating from the entrance mirror.

One solution to this problem is to try and avoid stray electrons, or at least prevent them from moving freely to problematic places. Attracting electrons to a positive electrode nearby and sucking them away does not work as expected. This can already be seen by the fact that the most positive electrode in the vicinity of the electrons is the collector, and even this does not prevent the leakage currents described in chapter 4.

Repelling electrons is much more fruitful. This can be seen when applying a negative bias to the pickup between the electron target and the exit mirror on the straight section. With the entrance mirror electrodes grounded, potentials applied to the exit mirror and the deflector in up position, a negative bias of some tens of Volts reduces the background level significantly. This way electrons can no longer reach the exit mirror. A positive bias shows no effect.

These results suggest the solution of the problem: Shielding the MCP from photons and where possible repelling electrons from the mirror regions. To achieve this, the getter modules between the electron target and the entrance mirror were connected in an insulated way to be able to bias them. A wall dividing the trap chamber was introduced and a cover separates the exit side of the trap. Figures 5.1 and 5.3 show this shields between the deflector and the exit mirror sets. The wall can be biased to repel electrons in addition to its purpose as a photon shield. The cover shields the detector from scattered photons that might enter the beamline and reach the MCP.

After installation, the noise level with electron current dropped considerably as can be seen from figure 5.8. With the shield in place, still some additional electron-induced background can be seen, but only an enhancement of about a factor of 3 is observed. It should be noted that without correction of the earth magnetic field, the noise level increases.

5.2.3 Influence of electron target potentials

It has already been mentioned that the effect of the electron target potentials on the stored ions is subtle, as it does not completely destroy the trapping condition. However, with the potential values of section 4.3.3 applied to the electron target, the storage lifetime measured with a 4.2 keV Ar^+ beam was considerably shorter than with all electron target electrodes grounded. This effect could clearly be attributed to the applied potentials, as the same results were found without electrons present for a cold cathode. To study the influence of different electrodes in an attempt to reduce the effect on the stored ion beam and optimise the lifetime, the measurements in figure 5.9 were performed. Here the trapping lifetime and the number of MCP counts for the same number of injections are shown for different electron target potentials. The respective potential combination can be derived from table 5.1. The lifetime gives an indication of trapping condition and the influence of the applied electron target potential on the stored beam, the number of MCP counts gives an idea of the quality of the initial trapping. Any influence on the beam entering the trap reflects in the number of ions stored

	Cath	Shields	Extr	Acc	Shielding	Coll
1	0	0	0	0	0	0
2	-50	-52.5	0	0	0	0
3	-50	-52.5	-31	6	0	0
4	-50	-52.5	-31	15	0	0
5	-50	-52.5	-31	15	30	0
6	-50	-52.5	-31	15	10	0
7	-50	-52.5	-31	15	10	60

Table 5.1: *Potential combinations. For the naming of the electrodes, refer to figure 4.3.*

and thus the total number of counts within a given timeframe. Only small modifications to the electron target potentials are permissible that do not change the electron beam behaviour. With negative potential applied to the cathode and the Pierce and
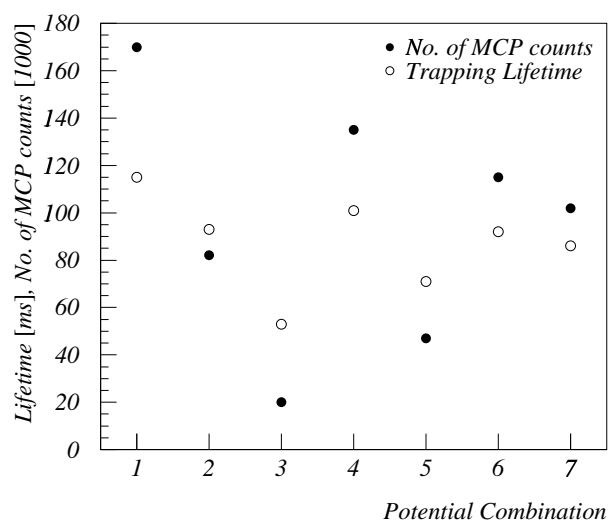
Figure 5.9: *Influence of applied electron target potentials on the ion storage of a 4.2 keV* Ar^+ *beam. The various potential combinations are given in table 5.1 above.*

side shield (combination 2), a negative effect can be seen that is even stronger with the extraction electrode also on negative potential (not shown). Applying a positive potential of 6 V to the acceleration electrode (combination 3) improves this slightly, but only when applying more positive potential (15 V, combination 4) a considerable improvement is achieved. On the collector side of the electron target, a shielding potential of 30 V (combination 5) again decreases the lifetime, while for the shielding electrode set to 10 V (combination 6) less effect is seen. With the collector set to 60 V (setting 7) only a small reduction in lifetime has to be accepted. Overall, the lifetime with electron target potentials applied according to combination 7 ('tuned' potentials) reduces from about 115 ms to about 90 ms. The influence seems to be larger on the

injected beam than on the storage condition as the number of MCP counts are more affected.

	Cath	Extr	Acc	Shielding	Coll
untuned	-50	-31	6	30	60
tuned	-50	-31	15	10	60

It is not immediately clear why storage is better in the 'tuned' configuration. The simulated electron target potential values were optimised for low residual fields in the interaction region. Because further acceleration towards the collector minimises leakage current (section 4.3.3), the interaction region where the ion beam crosses the electron beam was moved closer towards the cathode. In figure 5.10 the interaction region with equipotential lines is shown for the 'untuned' potential values. At *point A*, a field of
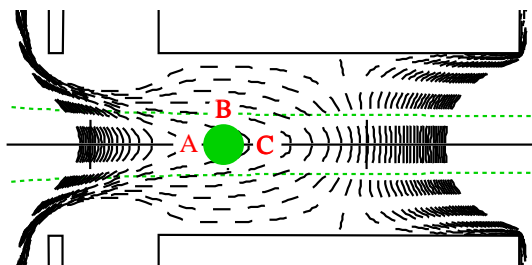
Figure 5.10: *Equipotential lines in the interaction region with simulated ('untuned') electron target potentials. Shown is the space between the acceleration electrodes to the left and the interaction electrodes. The circle marks the ion beam position and expected size of about 3 mm diameter. The electron beam is shown with dashed lines. Equipotential lines are plotted for potentials from -2.5V to 2.5V with 0.1 V spacing.*

0.1 Vcm^{-1} is directed towards the cathode (in the figure to the left) and acts on the ions. At *point B*, 0.7 - 1.0 Vcm^{-1} are directed towards the symmetry axis, at *point C* 0.4 Vcm^{-1} act towards the cathode.

With the optimised 'tuned' potentials, the influence of the residual fields on the ions is higher. The interaction region is shown for comparison in figure 5.11. At *point A*, a field of 1.8-2.0 Vcm^{-1} directed towards the collector (in the figure to the right) acts on the ions. At *point B*, 0.5-1.0 Vcm^{-1} are directed towards the symmetry axis, at *point C* 0.8 Vcm^{-1} act towards the collector.

Storage is better in 'tuned' configuration, although there is a much higher influence from the residual field on the stored beam. With these potential applied to the electron target electrodes, a reduction in trapping capability has still to be accepted. The potentials found here were used for further experiments. Since these early optimisation measurements, considerable improvements were achieved regarding the trapping lifetime, mainly due to finetuning the trap mirror settings.
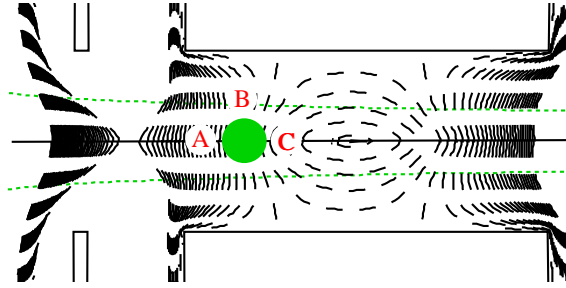
Figure 5.11: *Equipotential lines in the interaction region with optimised ('tuned') electron target potentials.*

5.2.4 Influence of electron beam modulation

For reasons outlined in section 2.4.2, the electron beam needs to be modulated for collision cross section measurements. To modulate the electron beam, only the cathode potential has to be switched to ground potential (or close to ground potential). The influence on the fields in the interaction region when changing the cathode potential is minimized by the remaining negative potentials of the shields and the extraction electrode. The switching however influences the trapping. In figure 5.12 the inverse
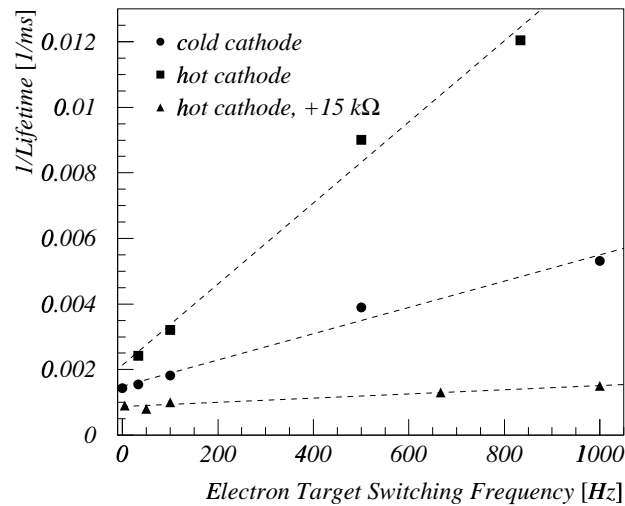
Figure 5.12: *Influence of the electron target switching frequency on the trapping lifetime. Measured with a 4.2 keV Ar$^+$ ion beam, 50 % duty cycle of switching.*

lifetime is plotted against the switching frequency of the electron beam. Switching the electron beam is clearly a loss process.

When changing the transition time of the switching from around 20 ns to 20-30 μs by

adding a 15 kΩ resistor to the circuit, this effect could be remedied. As the trapping has been optimised by the time the resistor was added, the lifetime was considerably longer than with the earlier measurements.

At this point, the necessary conditions for measurements on electron-ion collision are met: trap and electron target are working, ion storage is possible with the electron beam operating. Electron beam modulation is also implemented. In the following section, the procedure to accomplish first measurements is explained and results are discussed.

5.3 Towards first measurements

5.3.1 Cross section determination

For the measurements of this work, the electron beam is modulated all the time with a fixed frequency, not synchronised with the injection of the ion beam. This way each point in time after the injection is evenly sampled both with electron beam on and electron beam off. An example of the data obtained with the experimental scheme of
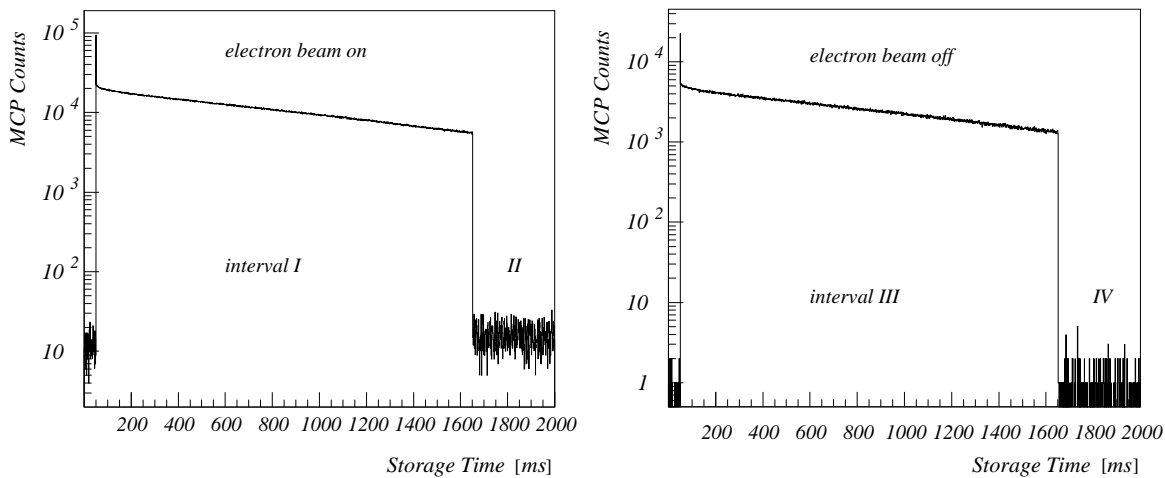
Figure 5.13: *On the left the histogram from multiscaler channel 1 is shown, where the electron beam is on, on the right channel 2 with electron beam off. The intervals II and IV where the ion beam is taken out of the trap are used for background subtraction. This example of data represents about 850 trapping cycles taken with Ar^+ and a 40 eV electron beam modulated at 100 Hz with a duty cycle of 20 %.*

figure 2.8 is shown in figure 5.13. Histogram 1 contains the data taken with electron beam on, histogram 2 data without electrons present. The number of counts in the two histograms are different due to the duty cycle of the electron beam modulation. This is corrected for in the following way: As a reference, one run is taken without modulating the electron beam, but still using the modulation signal to toggle between

the data taking channels. The correction factor is determined from the ratio of the bincounts in both histograms.

During the intervals I to IV (see figure 5.13), the following rates are probed:

$$
\begin{aligned}
R_I &= R_s + R_{b,ei} + R_{b,i} + R_{b,e} + R_{b,det} & (\,e + i\,) \\
R_{II} &= R_{b,e} + R_{b,det} & (\,e + no\ i\,) \\
R_{III} &= R_{b,i} + R_{b,det} & (\,no\ e + i\,) \\
R_{IV} &= R_{b,det} & (\,no\ e + no\ i\,)
\end{aligned}
$$

R_s denotes the signal rate of the process of interest, and $R_{b,x}$ stands for background rates originating from electrons (e), ions (i) and other electronic and detector noise (det). As the background rates without ions in the trap are small, we define the corrected rates with electron beam on, R_{sb} and with electron beam off, R_b:

$$
\begin{aligned}
R_{sb} &= R_s + R_{b,ei} + R_{b,i} = R_I - R_{II} \\
R_b &= R_{b,i} = R_{III} - R_{IV} \quad .
\end{aligned}
$$

An important task of the beam modulation method is to ensure equal conditions for the various different situations. As a combined electron-ion background $R_{b,ie}$ cannot be measured separately and thus not differentiated from a 'real' signal, the parameters of the modulation, the frequency and the duty cycle, have to be carefully optimised to reduce this background contribution. A possible local pressure increase when the electron beam is on, resulting in a higher neutral production rate could constitute a physical reason for this combined background. This is discussed in section 5.3.2.

The corrected count rate without electrons present can be written as arising from an ion beam decaying with a single exponential behaviour in the trap:

$$
R_b(t) = r_b b\ N_0\ e^{-\bar{\alpha}t} = r_b b\ N(t) \quad ,
$$

where $\bar{\alpha}$ is an effective loss rate during electron beam modulation, which needs to be fast compared to the storage lifetime. N_0 is the initial number of ions in the trap, $N_0 = N(t{=}0)$. With electrons present, an additional process leads to a higher count rate:

$$
R_{sb}(t) = r_{sb}(a + b)\ N_0\ e^{-\bar{\alpha}t} = r_{sb}(a + b)\ N(t) \quad .
$$

The factors r_b and r_{sb} describe the detector efficiency and a and b are yield constants. Only neutrals leaving the trap through the exit mirrors are counted, but this affects both signal and background events, likewise the efficiency of detection, therefore $r_b = r_{sb} = r_{eff}$. Requiring again that the modulation of the electron beam is fast compared to the storage lifetime, the number of counts in an interval Δt of histogram 1 can be written as

$$
N_{sb}^{\Delta t} = r_{sb}\ (a + b) \int_{\Delta t} N(t)dt \tag{5.1}
$$

and for the same interval in histogram 2 without the additional electron-induced process

$$N_b^{\Delta t} = r_b \, b \, \int_{\Delta t} N(t) dt \quad . \tag{5.2}$$

Without a direct measurement of the number of ions stored in the trap, this integral cannot be determined, and thus, only the ratio between signal and background rate can be derived, dividing 5.1 by 5.2.

$$\frac{N_{sb}^{\Delta t}}{N_b^{\Delta t}} = \frac{r_{sb}}{r_b} \frac{a+b}{b} = \frac{R_{sb}}{R_b} = \left(\frac{R_s}{R_b} + 1 \right) \quad . \tag{5.3}$$

According to equation 2.9, the cross section of interest can be written as

$$\sigma_s = \frac{R_s}{R_b} \sigma_b \frac{\rho_b v_i}{\rho_e v_e} \frac{l_{tr}}{l_e} = \frac{R_s}{R_b} \sigma_b \frac{1}{I_e} A_e e \rho_b v_i \frac{l_{tr}}{l_e} \quad , \tag{5.4}$$

with I_e the electron current and A_e the electron beam area. This equation can be used together with 5.3 to determine a relative cross section value for a given ion species. With the cross section for the neutral-producing background process known, an estimate for the absolute value can be achieved. Under the assumption that the neutral-producing background process is the dominant loss process in the trap, this cross section can be calculated from the trapping lifetime, leading to the following expression for the cross section of the electron-induced process

$$\sigma_s = \frac{R_s}{R_b} \frac{1}{I_e \tau} A_e e \frac{l_{tr}}{l_e} \quad \text{if assumed:} \quad \sigma_b = \frac{1}{\tau \rho_b v_i} \quad . \tag{5.5}$$

Experience from the linear trap shows that this assumption is not fully justified, as scattering losses, which do not produce counts on the MCP, are also important and contribute comparably to the lifetime [69]. It can only be used as a very rough judgement of the correct order of magnitude of the effect.

Once the number of ions in the trap $N(t)$ is accessible, this reference to the background cross section can be avoided. The integrals in equation 5.1 and 5.2 can be evaluated and the factor a describing the signal rate derived. The ratio

$$\frac{R_s(t)}{I_i(t)} = \frac{r_{eff} a N(t)}{e v_i N(t)} l_{tr} = r_{eff} \frac{a l_{tr}}{e v_i}$$

can be inserted into equation 2.3 to give an expression for the cross section, independent of ion species

$$\sigma(E) = N e^2 F \frac{v_e}{(v_i^2 + v_e^2)^{1/2}} r_{eff} \frac{a l_{tr}}{e I_e} \quad .$$

The value for the form factor F is still not known, likewise the detection efficiency r_{eff}, so only relative cross section measurements can be obtained. The animated-beam method [48, 49] overcomes the uncertainty regarding the form factor, the detector effeciency has to be assessed separately.

Another important point to mention is the fact that the longer the trapping lifetime, the easier it becomes to measure an electron-induced signal. The yield constant b is inversely proportional to the trapping lifetime without electron beam present. With smaller b, equation 5.3 can be solved for a with better significance for a given number of trapping cycles.

In the following sections first test measurements of electron-ion collisions are presented. As the experimental signal, the following quantity was defined

$$S = \frac{1}{(E/eV)^{3/2}} \left(\frac{N_{sb}^{\Delta t}}{N_b^{\Delta t}} - 1 \right) \quad . \tag{5.6}$$

This represents a parameter proportional to the cross section according to equation 5.4, if the electron current is taken as proportional to the electron energy E to the power of 3/2. In section 4.3.2, this dependency could be confirmed for the cathode current.

In a first set of tests, the combined background contribution $R_{b,ei}$ has to be assessed. With an ion that is not expected to give rise to an electron-induced signal, the combined electron-ion background can directly be tested. The influence of frequency and duty cycle of the electron beam modulation on this background need to be checked and optimal settings determined. With an ion that should give rise to a signal due to electrons, a signal has to be measured.

Once a signal is seen, the energy dependence can be measured. For each electron energy, data are taken for a large number of storage cycles. Typically, about 1000 storage cycles are recorded, resulting in a measuring time of about 30 minutes for each data point. Even longer measurement times are needed for small electron energies, due to the small electron current values encountered. To infer a cross section measurement from this, other energy-dependent effects that may fake or mask a certain energy dependence have to be excluded. The form factor F has to be proven to be independent of the electron beam energy. This can only be inferred indirectly by measuring an electron beam profile in the interaction region by scanning the electron beam through the ion beam. Among the other parameters entering the measured cross section value apart from the signal and background counts is the electron beam current I_e. Its energy dependence has to be correctly taken into account. In section 4.3.2 it was demonstrated that the leakage current does not scale with energy in the same way as the current seen behind the interaction region on the shielding electrode and the collector. How this leakage current takes part in the ion interactions needs to be clarified. This can be attempted by comparison of literature data to the measured data, determined with and without this leakage current included. Beam profile measurements also contribute to the understanding in this domain.

5.3.2 Measurements on Ar$^+$ and CO$^+$ - understanding background contributions

By using Ar$^+$ as a candidate for an ion where no electron-induced signal is expected, the effect of a possible combined electron-ion background contribution can be analysed. The assumption about this background is that it may arise due to a local pressure increase close to the electron target structure by electron-stimulated desorption. This effect is thus expected to scale with electron current. To prove that a measurement is unaffected by this background it has to be proven that it is either vanishing or small compared to the true electron signal. The conditions that need to be optimised to decrease this effect are the frequency and the duty cycle of the electron beam modulation. Ideally, one would choose a modulation frequency as high as possible. The faster the switching, the more stationary pressure conditions may be, cancelling the combined electron-ion background. Practical limitations however limit the frequency of the modulation: Firstly, there is still an effect on the storage lifetime, albeit small (see section 5.2.4), and secondly, since the switching time of the electron beam (about 20-30 μs) is discarded from the data, at high modulation frequencies a higher and higher fraction of the data taking time is lost. A good compromise was found when using 100 Hz modulation frequency. Another compromise has to be found regarding the duty cycle of the modulation. A duty cycle of 50 % is ideal to get best possible statistics, but the smaller the exposure to electrons, the better the pressure conditions. A measurement with different duty cycles at 40 eV beam energy and an electron beam modulation at 100 Hz is presented in figure 5.14. A signal can be seen that is originat-
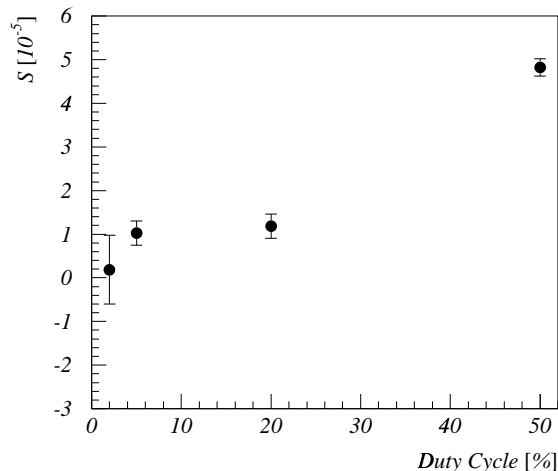
Figure 5.14: *The effect of different duty cycles on a signal on Ar$^+$. As expected, the smaller the duty cycle, the less influence on the pressure conditions due to the electrons. Measured with 40 eV electron beam at a modulation frequency of 100 Hz.*

ing from a combined electron-ion background. Only a duty cycle of 2% gives a signal that is compatible with zero. Larger duty cycles obviously affect the pressure condi-

tions, resulting in a rising signal. At small duty cycles measurement times to acquire enough statistic are longer, so for further tests, a duty cycle of 20 % was chosen as a compromise.

To assess the possible reason for the signal seen at higher duty cycles, the energy dependence was investigated. Any process due to electrons is expected to scale with electron current. As the signal is normalised to electron current, a constant value is expected when plotting it against the electron beam energy E. This is shown in figure 5.15. The Ar^+ data is compatible with a constant level of $1.6 \pm 0.2 \cdot 10^{-5}$. Any process
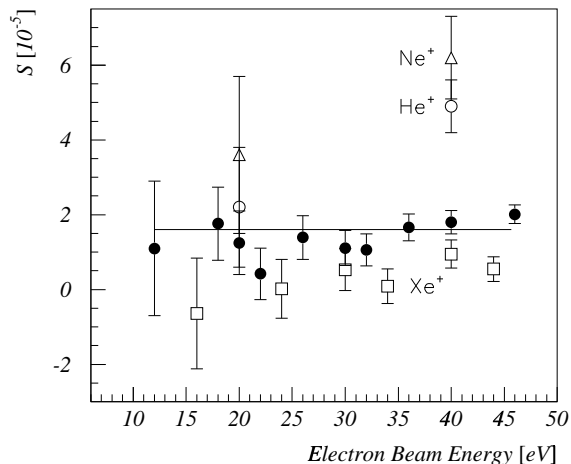
Figure 5.15: *Measurement on Ar^+ with 20% duty cycle, 100 Hz modulation. The constant fitted to the Ar^+ data corresponds to $1.6 \pm 0.2 \cdot 10^{-5}$.*

related to the ions only is not expected to depend on the electron energy and would exhibit as a $E^{-3/2}$ behaviour of S in the plot. A process of unknown nature that scales linearly with electron energy would also be consistent with the measurements. Another clear evidence for the proposed origin of the combined electron-ion background (a local pressure rise in the electron target) is the fact that when moving the electron target above the ion beam, no signal is seen with the same settings for which a signal was observed when the ions are passing through the electron target.

Such a background signal should be independent of the ion species as it is of the same nature as the ion background and thus directly proportional to it. Measurements on Xe^+ confirm this, although data taken with the lighter ions He^+ and Ne^+ deviate slightly. Only very limited data were taken with the latter two ions at an early stage of the data taking. Altogether an influence of the combined electron-ion background on about the level of $2 \cdot 10^{-5}$ in S is seen.

Using CO^+ as an ion that is expected to exhibit dissociative excitation and with the same setup, the signal in figure 5.16 is obtained. There is a plateau significantly above the Ar^+ values between electron energies of 15 eV and 50 eV. At energies smaller than 15 eV, the signal is very rapidly decreasing. At very small electron energies
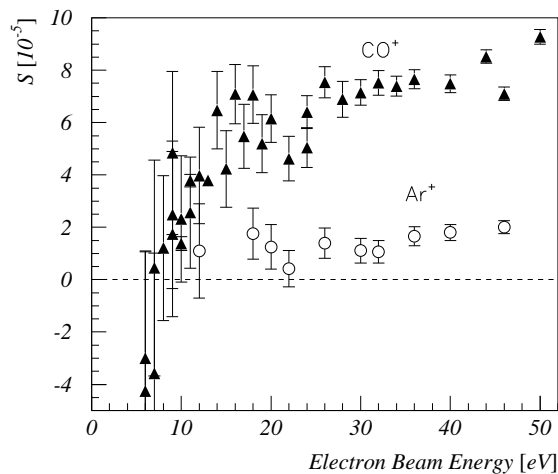
Figure 5.16: *Measurement on Ar⁺ and CO⁺.*

(6 and 7 eV) the signal is negative, but still compatible with zero. Because of the very small electron current here, these values have to be treated with extreme caution. As
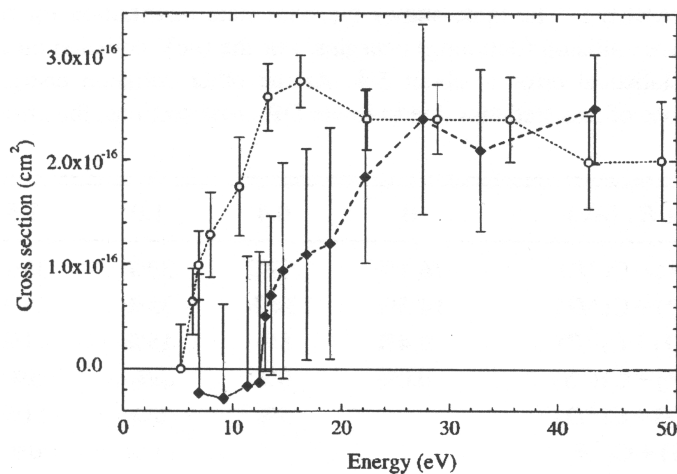

Figure 5.17: *Measurement of dissociative excitation on CO⁺, taken from [103]. The open symbols are from a single-pass experiment [104], the solid symbols from a storage ring measurement at Cryring [103].*

a comparison and simply to guide the eye of a benevolent reader, earlier measurements of dissociative excitation on CO⁺ are shown in figure 5.17. The single-pass experiment gives an onset of the measured cross section at about 5 eV. The storage ring data on cold CO⁺ were obtained after storing the ion for 5 s and give an onset between 10 and 20 eV. In our case, data were obtained at storage times between 100 and 1650 ms, so our trap measurement should be closer to the single-pass experiment in this case. A

correction due to the different work function of the cathode (see 4.3.4) has not been included. Most certainly, the data has to be shifted by about 2 eV towards smaller energies, with an estimated uncertainty of about 0.5 eV.
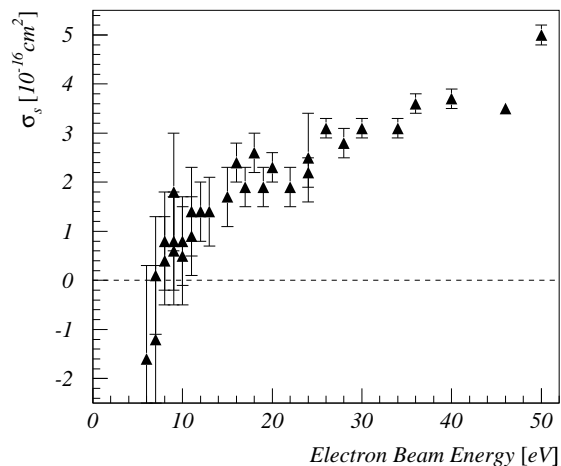
Figure 5.18: *CO^+ cross section estimate using the trapping lifetime as a way to eliminate the background cross section.*

Using the method suggested earlier to utilise the trapping lifetime to get a judgement of the order of magnitude of the effect, the cross section thus determined from equation 5.5 is shown in figure 5.18. A fairly similar behaviour to figure 5.16 shows up due to the fairly constant trapping lifetimes during the data taking. Only the lifetime for 50 eV is slightly shorter, artificially increasing the value for σ_s. The magnitude of the cross section fits the literature data shown in figure 5.17 remarkably (and unexpectedly) well. The different trapping lifetimes of Ar^+ and CO^+, shown in figure 5.19 cannot explain the different signal behaviour: The lifetime for Ar^+ is only about 30% longer than the lifetime of CO^+. The signal for CO^+ is significantly above a 30% enhancement of the Ar^+-signal and can thus be attributed to a different effect, arising from electron-induced collisions.

According to equation 3.3 in section 3.2.3, the lifetime due to neutral-producing background processes is proportional to $\sqrt{m}$, with m being the ion mass. Thus, an increase in lifetime of about 20% is expected for Ar^+ with respect to CO^+. The fact that the measured difference is consistently larger indicates the influence of another contribution to the lifetime. Scattering losses are assumed to be more important for light ions, so this finding is consistent with expectation. With higher ion masses, the lifetime becomes larger, making measurements easier.

Summarising this section, there is a combined electron-ion background possibly created by additional neutral-producing restgas collisions when the electron beam increases the local pressure inside the electron target region. The background signal observed scales with electron current and should be independent of the ion species. To verify the last
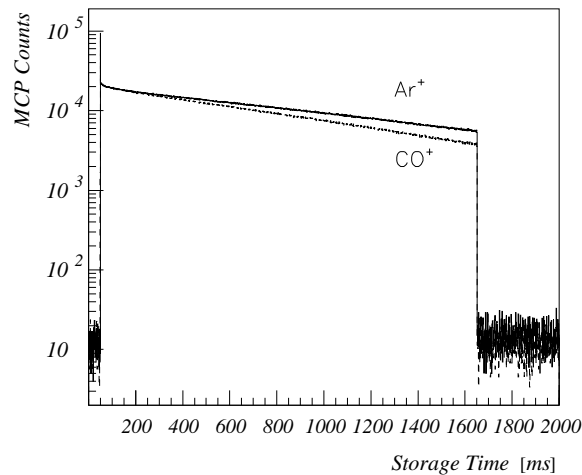
Figure 5.19: *Trapping lifetimes of Ar^+ (τ=1.3 s) and CO^+ (τ=1.0 s), measured with a 40 eV electron beam. The CO^+ data are slightly scaled to give the same initial number of trapped ions after injection.*

statement, some more measurements are needed. A measurement on CO^+ shows a different behaviour giving a larger signal at high electron energies than Ar^+ and a decrease with smaller energies. The magnitude of the cross section estimated comes close to expected values from the literature.

5.3.3 Measurements on C^- and B^- - first detachment measurements

Preliminary measurements on detachment processes from negative ions can be seen in figure 5.20 for C^- and B^-, respectively. For each ion, the quantity S is plotted on the left. On the right, the lifetime was used to estimate an absolute value for the cross section. For C^-, an earlier measurement with a crossed-beam apparatus [105] suggests a value of about $1.7 \cdot 10^{-15}$ cm^2 for energies between 10 and 25 eV, slowly decreasing with energy. At 50 eV, a value of $1.3 \cdot 10^{-15}$ cm^2 is reported. In contrast to this, our measurements show an increase with energy, with the values of the cross section in the right order of magnitude. For B^-, hardly any signal could be measured. Values between about $9 \cdot 10^{-15}$ cm^2 for 10 eV and $3 \cdot 10^{-15}$ cm^2 for 50 eV are reported from a storage ring experiment [106]. The reason for the difficulties can be seen in figure 5.21. Only very short lifetimes could be achieved for B^-.

Despite these discrepancies, a detachment signal can be seen, at least for the C^- measurement.

By already showing measurements of cross sections one question is immediately posed: Are there any other dependencies that could fake a similar energy characteristic or mask an existing one? Such an effect can only stem from the electrons and can only change an existing electron-induced signal, as the flat measurement of Ar^+ testifies,
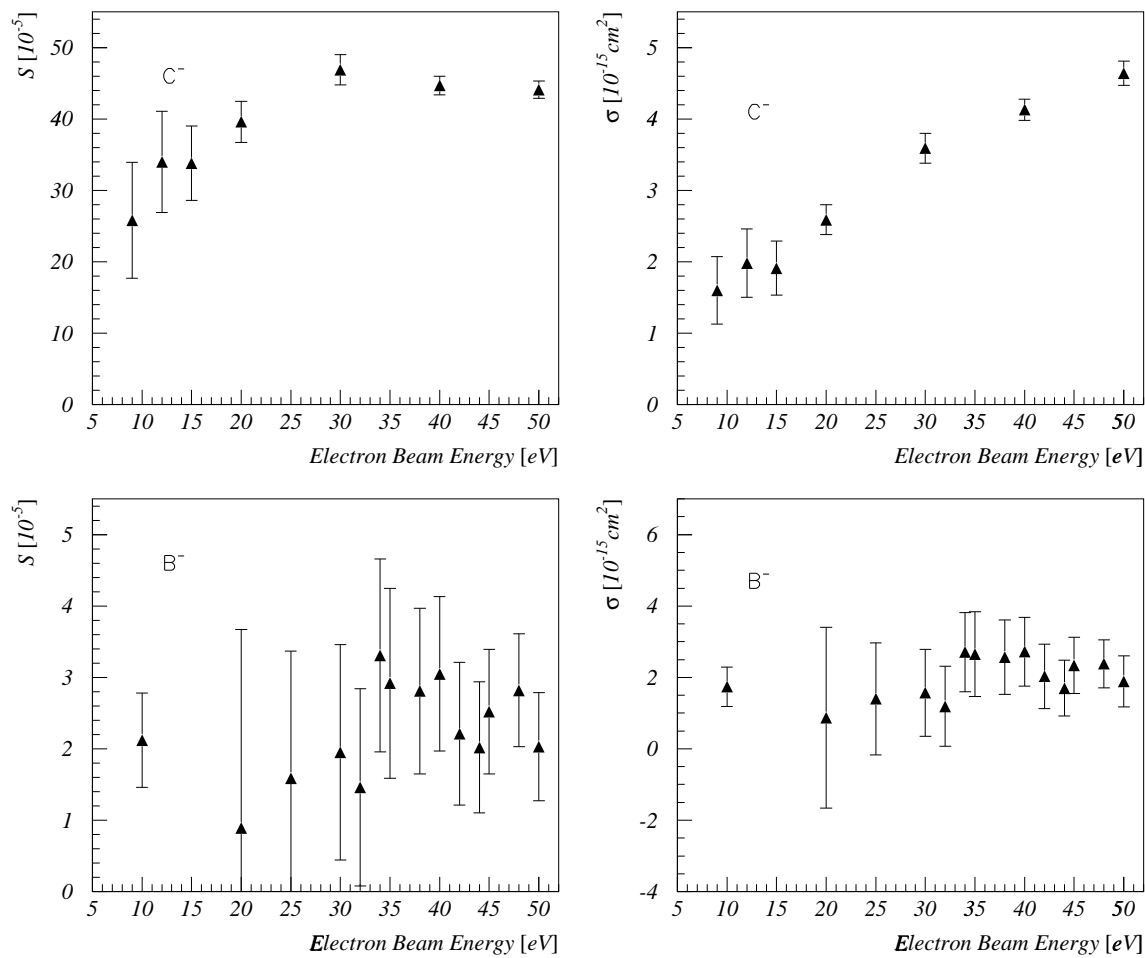
Figure 5.20: *Measurements on C^- and B^-.*

where the electrons have no direct effect on the ion. It has to be shown that the form factor describing the overlap between both electron and ion beam stays constant with energy. This can in principle be experimentally confirmed by measuring the electron beam profile, scanning the electron beam through a thin ion beam. An example of such a measurement is given in figure 5.22. It can be seen that a very wide ion beam was trapped, as the extreme positions where trapping was still possible are only 8 mm apart. With a gap between the interaction electrodes of only 13 mm, an ion beam width of 5 mm has to be assumed. To assess the electron beam profile, a mirror configuration which results in a smaller ion beam has to be found. Therefore, no further measurements at different electron energies were performed at this stage.
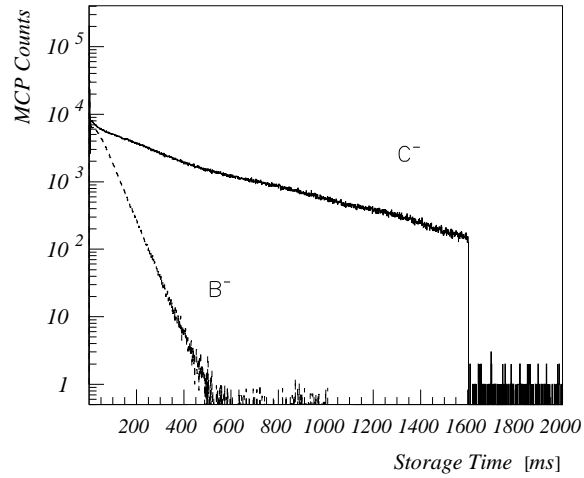
Figure 5.21: *Trapping lifetimes of C^- (τ=450 ms) and B^- (τ=50 ms), measured with a 40 eV electron beam. The B^- data are slightly scaled to give the same initial number of trapped ions after injection.*
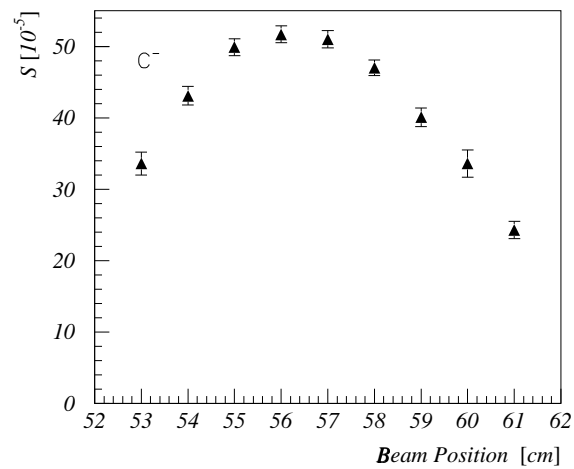
Figure 5.22: *Measurements on C^- at 40 eV electron energy, varying the electron beam position.*

5.3.4   Detachment measurements on C_2^- - verifying energy dependencies

According to equation 5.4, the electron current has to be taken correctly into account for a cross section determination. An online current measurement has not been realised for the modulated electron beam, so we rely on test measurements on a dc beam. Here we have to pick up one of the findings of these tests, namely the occurrence of leakage currents. Although we believe that it originates from secondary electrons and not from a beam profile that fundamentally differs from the simulation, we still have to take this into account and see its influence. The electron current scaling that needs to be done to arrive at a signal proportional to the cross section has so far been done by simply using $I_e(E) = E^{3/2}$ with E the electron energy (equation 5.6). This dependency was confirmed in section 4.3.2, figure 4.14 for the current seen flowing from the cathode. However, the effective collector current deviates from the Child-Langmuir law. This current that is collected behind the interaction electrode surely has passed the interaction region, whereas the leakage current seen on other electrodes might not. To quantitatively assess the changes due to a scaling of the observed signal with this current instead of simply using the 3/2 power law and thus the cathode current, an approximation of the form $y = ax^b$ was used to fit the data in the right plot of figure 4.14.

The effect can be seen on measurements for the detachment reactions $C_2^- \rightarrow C_2^0 + 2e^-$ and $C_2^- \rightarrow C^0 + C^0 + 2e^-$. By using the $E^{3/2}$-scaling, the cathode current was used in the left plot of figure 5.23. The result of the above mentioned analytical approximation
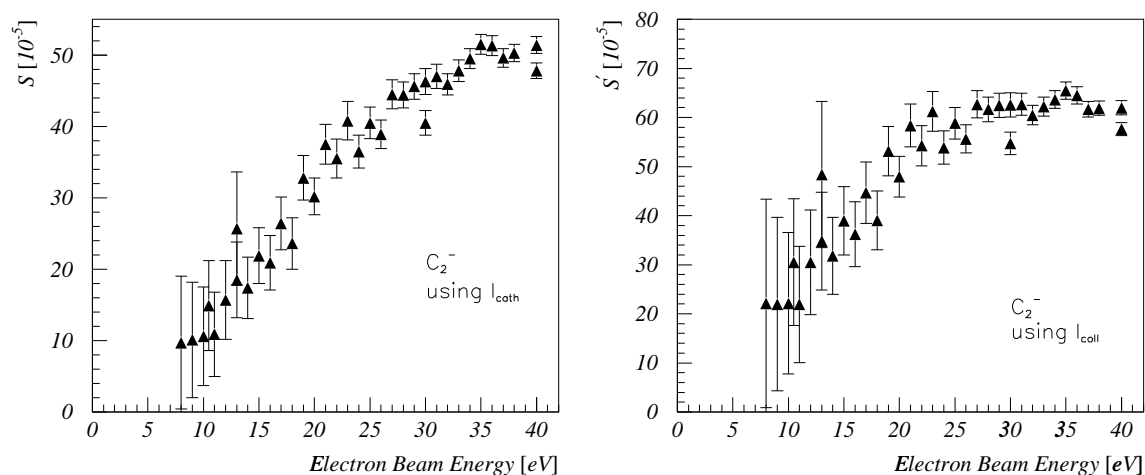

Figure 5.23: *Measurement on C_2^-. On the left, the current was taken into account by using a 3/2 power law to scale with the cathode current, on the right, a correction was made to effectively use the current seen on the shielding electrode and the collector.*

(a=19.243, b=0.396) was used in the right plot to correct the signal to the effective

collector current:

$$S' = \frac{100}{a \; (E/eV)^b} \; S \quad .$$

Firstly it has to be noted that the magnitude of the signal is much larger than the background signal seen on Ar^+, clearly indicating an electron-induced process. Secondly, even with the correction of using the current collected behind the interaction region only and not the cathode current (which is quite dramatic at low energies), a real signal rising with energy can be seen. By acknowledging this, we can compare to literature data of this reaction and try to establish which current scaling has to be used.

The effect of different fractions of current being responsible for the signal at different energies is basically the same as the already discussed effect of a possible change in form factor with electron energy. With the broad ion beam in our measurement it seem highly unlikely that current that reached the collector has not passed the interaction region. A possible scenario that still accounts for this might be the electron beam being bent up or down by a not properly corrected magnetic stray field, hitting and bouncing off the interaction electrode and reaching the collector, avoiding the ion beam all the way. The fact that the electron beam can bounce off from metal surfaces was seen when steering the electron beam horizontally with a magnetic field when the deflector was in down position. At very extreme settings, a rise in collector current was seen after an initial drop (see section 4.3.5). However, a magnetic field strong enough to deflect the electron beam that dramatically is impossible when the fields are corrected (see discussions in the same section), and even if this was not the case, with the given broad ion beam the above mentioned scenario is extremely unlikely. Nonetheless, further beam profile measurements should be undertaken to confirm these considerations.

In figure 5.24, the measurement on C_2^- is compared to data taken at the Astrid storage ring [107]. The pure detachment channel (final C_2^0) dominates and has a threshold at about 7 eV, about 2 times the electron affinity of 3.27 eV. The cross section for the detachment plus dissociation channel leading to $C^0 + C^0$ is about one order of magnitude smaller, while the cross section for the dissociative channels are about 3 orders of magnitude smaller; see also section 2.2.

Till now, no comparison to data has been made, so the calibration of the electron beam energy is not precisely known. Due to the work function difference between the cathode and the titanium electrodes a shift of 2 to 2.5 eV towards smaller energies is likely. The contribution due to the ion motion and some residual field in the interaction region are smaller in size and opposite in sign. The net effect is largest at high electron beam energy as the latter effect scales with electron energy, but at a level below about 0.4 eV. This small effect was not considered here, as the uncertainty of the work function difference is larger for the moment being. The trap data was shifted by 2 eV towards smaller electron energy to account for the work function difference and scaled at an electron energy of 18 eV to the Astrid data. The two possible electron current normalisations are shown: on the left, a normalisation to the cathode current was accomplished by using the $E^{3/2}$ dependence on the electron energy, while on the right a correction to take only the effective collector current into account was applied.
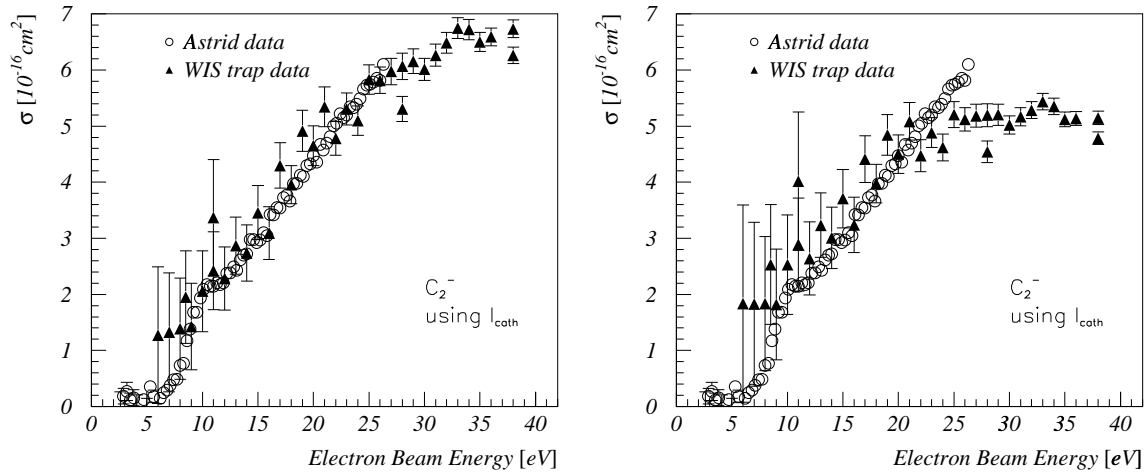
Figure 5.24: *Comparison between $C_2^- + e^- \rightarrow C_2^0 + 2e^-$ and $C_2^- + e^- \rightarrow C^0 + C^0 + 2e^-$ data taken at the Astrid storage ring ([107], open symbols) and first measurements in the Weizmann Institute trap (filled symbols) for the different electron current normalisations. On the left, a normalisation to the cathode current is performed on the trap data, on the right, a normalisation to the effective collector current. The trap data was scaled at an electron energy of 18 eV to the Astrid data.*

The Astrid data fits better to the trap data normalised with the cathode current, giving another indication of the harmlessness of the leakage currents observed.

Similarly to the estimation in the previous section, the trapping lifetime can be used to assess the magnitude of the cross section measured. Cross section values calculated according to equation 5.5 are shown in figure 5.25. In this case, the values obtained do not fit the expected order of magnitude, showing yet again the poor man's character of this approach. As an indication that other effects on trapping lifetime have a large influence on these estimations, the distinctive odd-even effect above electron energies of about 25 eV can be used. Data were taken sampling even E going up and odd E going down in energy. This long-time drift of observed lifetimes is probably associated with the problems seen in the trapping of C_2^-. The decay of ions in the trap as monitored by the neutral counts did not follow an exponential decay, see figure 5.26. This variation of trapping times leading to this stepwise decay was not observed for earlier runs with this ion. As some electronics components failed in due course (high voltage resistor and mirror hv switch), this effect is probably of external nature. The steps are seen at the same times after injection for each run that exhibits this behaviour. Some minor variation in the mirror potentials can change the trapping configuration and affect the lifetime. Owing to the modulation technique, the signal is unaffected by the lifetime conditions, if only they are similar for the runs compared. To estimate an absolute number for the cross section magnitude, this data cannot be used without corrections. The lifetime used for figure 5.25 was derived from a fit to the trapping times used for the evaluation of the signal, resulting in an average lifetime. The maximal lifetime ob-
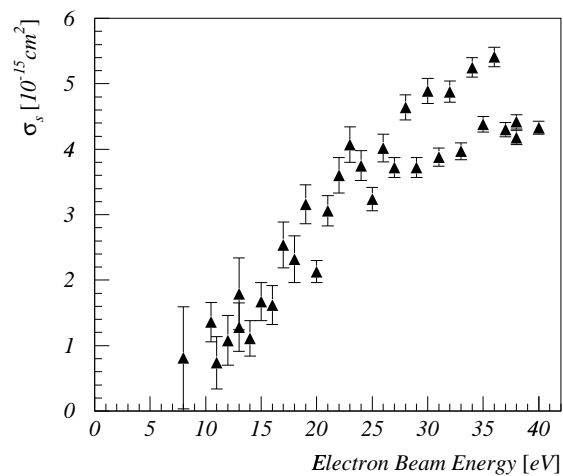
Figure 5.25: *Estimation of an absolute cross C_2^- detachment cross section using the trapping lifetime as a way to eliminate the background cross section.*
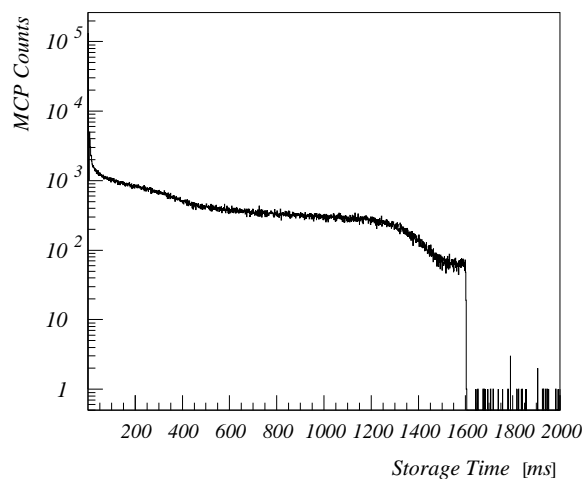

Figure 5.26: *Storage conditions for C_2^-. The observed shape is probably due to external effects.*

103

served can be taken as a lower limit for a lifetime determined by the neutral-producing background process. With this an estimation of the cross section gives values in the higher 10^{-16}cm^2, much closer to the literature data.

The measurements on C$_2^-$ can be compared with storage ring data. A reasonable agreement can be achieved when using the cathode current taken from test measurements on the electron target, supporting the proposed origin of the leakage current. A final answer in this domain suffers from beam profile measurements with better resolution of the electron beam. This could also give an estimate of the form factor and its (in)dependence on electron energy.

Estimates on the absolute cross section values are by nature very crude, as they rely on a determination of the neutral-producing background process on the basis of the trapping lifetime. Still, values calculated come close to the literature data, indicating the correctness of the measurements.

Chapter 6

Perspectives and Outlook

In the course of this work, first measurements of electron-ion collisions on stored ion beams were performed. To achieve this, a low-energy electron beam dedicated for use in an existing electrostatic ion beam trap was designed and built. An important design criterion was not to use magnetic confinement to produce the electron beam. The designated electron energies range from about 5 eV up to several tens of eV. The results of this work can be summarised as following:

- Test measurements show that the electron beam is operating and producing currents according to simulated values. Electron densities are between $\sim 2 \cdot 10^5 \text{cm}^{-3}$ at 5 eV electron energy and $\sim 2 \cdot 10^6 \text{cm}^{-3}$ for a 50 eV electron beam. A possible explanation for observed leakage currents could be derived. These currents constitute a considerable fraction of the current extracted from the cathode, especially at low electron energies.

- With proper correction of the earth magnetic field, electron beam energies as low as 5 eV can be achieved. Comparing measured residual fields with applied correction to simulations, no adverse effect is expected. Small current values, however, make measurements at these electron energies quite difficult.

- After preparatory work for the installation the electron target was placed inside a new bent electrostatic ion trap. Tests on the electron target were performed showing the possibility of operating an electron beam utilising a fairly large thermionic cathode in ultra high vacuum conditions ($7 \cdot 10^{-11}$ Torr).

- Several modifications were needed to solve charging problems before an electron beam could be operated while ions are still stored inside the trap.

- Preliminary data were obtained for the detachment processes of C_2^- and comparisons to earlier storage ring or single-pass merged or crossed beam measurements were drawn with some success.

Despite these achievements, which show that the principle of measuring electron-induced processes on trapped ion beams works, improvements are still needed in many fields. A few important problems to be addressed are:

- Further tests are desirable to verify the proposed origin of the leakage currents (secondary electrons backtracking from the collector). For this, comparisons to known cross sections can be used as well as beam profile measurements once an intense thin ion beam can be stored with high efficiency.

- The main uncertainty for the electron beam lies in the correct determination of the work function correction. Theoretical predictions are contradicted by measurements. A hypothesis explaining the discrepancies has been formulated and a possible way to measure this offset by monitoring the perveance and the beam profile has been suggested by attaching simulated dependencies. A precise beam profile measurement will also be needed in the future to assess this question.

- For the ion trapping, more efficient trapping conditions with better lifetimes need to be found with the deflector down, both for storage in the straight and in the bent mode. With a thinner beam, another option regarding diagnostics is given by measuring beam profiles more precisely. There are indications however that lifetimes alone do not influence the signal to background ratio. With different trap settings resulting in different lifetimes, the same signal to background ratio was obtained at the same pressure. This indicates that beam losses could be reduced by changing the mirror settings and thus the acceptance of the trap. The measurement of electron-induced neutrals is against the background of pressure-induced neutrals. Therefore, currently the pressure limits the signal to be measured against the background.

- Another effect that needs better understanding is the origin of the combined electron-ion background. This background sets a lower limit for the magnitude of measurable cross sections.

Additionally to tackling these problems, next measurements are planned on comparing cross sections of small negative carbon clusters. For a comparison of different ion species, small modifications and additions to the experimental approach are needed. A normalisation to the ion current has to be done directly, not indirectly by assuming or calculating a cross section for the neutral-producing background process. This cross section may be different for different ion species, and at the moment being, a calculation of the cross section by using the trapping lifetime is too uncertain due to the effect many other factors have on the lifetime. To get a signal directly proportional to the ion current or the number of ions in the trap, the pickup signal can be utilised. For this, the ions need to be kept bunched. The possibility to counter diffusion has already been demonstrated with the rf bunching technique described in section 3.3.2.
The ultimate goal is then to move on to even larger molecules and clusters. Not only due to intrinsic advantages of longer trapping lifetimes with heavy molecules, but first and foremost to benefit from the unique advantage of this approach in offering possibilities to explore electron collisions with stored, internally cold heavy molecular ions.

Bibliography

[1] F. L. Walls, and G. H. Dunn, Geophys. Res. 79, 1911 (1974)

R. A. Heppner, F. L. Walls, W. T. Armstrong, and G .H. Dunn, Phys. Rev. A 13, 1000 (1976)

R. D. DuBois, J. B. Jeffries, and G. H. Dunn, Phys. Rev. A 17, 1314 (1978)

[2] D. Habs et al., Nucl. Instr. and Meth. B 43, 370 (1989)

[3] S. P. Møller, in: S. T. Corneliussen (ed.), Proceedings of the 1993 Particle Accelerator Conference, Washington, DC, p. 1741, (1993)

[4] K. Abrahamsson et al., Nucl. Instr. and Meth. B 79, 269 (1993)

[5] M. Lange, PhD thesis, Universität Heidelberg, 2001

[6] Proceedings of the 1995 Workshop on Dissociative Recombination, eds. D. Zajfman, J. B. A. Mitchell, D. Schwalm and B. R. Rowe, World Scientific, Singapore (1996)

[7] Proceedings of the 1999 Workshop on Dissociative Recombination, eds. M. Larsson, J. B. A. Mitchell, I. F. Schneider, World Scientific, Singapore (2000)

[8] D. R. Bates, Phys. Rev. 78, 492-493 (1950)

[9] J. M. Bardsley and M. A. Biondi, Adv. At. Mol. Phys. 6, 1-57 (1970)

[10] A. Giusti, J. Phys. B: Atom. Molec. Phys. 13, 3867-3894 (1980)

[11] M. Born and J. R. Oppenheimer, Ann. Phys. 84, 457 (1927)

[12] J. M. Bardsley, J. Phys. B 1, 365-380 (1968)

[13] P. Forck, M. Grieser, D. Habs, A. Lampert, R. Repnow, D. Schwalm, A. Wolf, and D. Zajfman, Phys. Rev. Lett. 70, 4, 426-429 (1993)

[14] M. Larsson, H. Danared, J. R. Mowat, P.Sigray, G. Sundström, L. Broström, A. Filevich, A. Källberg, S. Mannervik, K. G. Rensfelt, and S. Datz, Phys. Rev. Lett. 70, 4, 430-433 (1993)

[15] C. Strömholm, J. Semaniak, S. Rosen, H. Danared, S. Datz, W. van der Zande, and M. Larsson, Phys. Rev. A 54, 4, 3086-3094 (1996)

[16] S. Krohn, M. Lange, M. Grieser, L. Knoll, H. Kreckel, J. Levin, R. Repnow, D. Schwalm, R. Wester, P. Witte, A. Wolf, and D. Zajfman, Phys. Rev. Lett. 86, 18, 4005-4008 (2001)

[17] T. Tanabe, I. Katayama, N. Inoue, K. Chida, Y. Arakaki, T. Watanabe, M. Yoshizawa, M. Saito, Y. Haruyama, K. Hosono, T. Honma, K. Noda, S. Ohtani, and H. Takagi, Phys. Rev. A 49, R1531 (1994)

[18] B. K. Sarpal, J. Tennyson, and L. A. Morgan, J. Phys. B 25, 5943-5953 (1994)

[19] S. L. Gubermann, Phys. Rev. A 49, 6, R4277-4280 (1994)

[20] G. H. Dunn and N. Djurić, in Novel Aspects of Electron-Molecule Collisions, edited by K. H. Becker, p. 241, World Scientific, Singapore, (1998)

[21] A. E. Orel, and K. C. Kulander, Phys. Rev. A 54, 6, 4992-4996 (1996)

[22] M. Larsson, M. Carlson, H. Danared, L. Broström, S. Mannervik, and G. Sundström, J. Phys. B: At. Mol. Opt. Phys. 27, 1397-1406 (1994)

[23] W. J. van der Zande, J. Semaniak, V. Zengin, G. Sundström, S. Rosen, C. Strömholm, S. Datz, H. Danared, and M. Larsson, Phys. Rev. A 54, 6, 5010-5018 (1996)

[24] B. K. Sarpal and J. Tennysin, Mon. Not. R. Astron. Soc. 263, 909-912 (1993)

[25] S. Krohn, Z. Amitay, A. Baer, D. Zajfman, M. Lange, L. Knoll, J. Levin, D. Schwalm, R. Wester, and A. Wolf, Phys. Rev. A 62, 03271-03781 (2000)

[26] L.H. Andersen, P Hvelplund, D. Kella, P.H. Moklert, H. B. Pedersen, H. T. Schmidt, and L. Vejby-Christensen, J. Phys. B: At. Mol. Opt. Phys. 29, L643-L649 (1996)

[27] H. B. Pedersen, N. Djurić, M. J. Jensen, C. P. Safvan, L. Vejby-Christensen, and L. H. Andersen, Phys. Rev. Lett. 81, 24, 5302-5305 (1998)

[28] H. B. Pedersen, N. Djurić, M. J. Jensen, D. Kella, C. P. Safvan, H. T. Schmidt, L. Vejby-Christensen, and L. H. Andersen, Phys. Rev. A 60, 4, 2882-2899 (1999)

[29] E. A. Solov'ev, Sov. Phys. JETP 45, 1089 (1977)

[30] B. M. Smirnov and M. I. Chibisov, Sov. Phys. JETP 22, 585 (1966)

[31] V. N. Ostrovsky and K. Taulbjerg, J. Phys. B 29, 2573 (1996)

[32] A. K. Kazansky and K. Taulbjerg, J. Phys. B 29, 4465 (1996)

[33] J. T. Lin, T. F. Jiang, and C. D. Lin, J. Phys. B 29, 6175 (1996)

[34] M. S. Pindzola, Phys. Rev. A 54, 3671 (1996)

[35] F. Robicheaux, Phys. Rev. Lett. 82, 707 (1999)

[36] F. Robicheaux, R. P. Wood, and C. H. Greene, Phys. Rev. A 49, 1866 (1994)

[37] R. F. Curl and R. E. Smalley, Science 242, 1017, 1988

[38] H. Kroto, Science 242, 1139, 1988

[39] K. W. Hinkle, J. J. Keady, and P. F. Bernath, Science 241, 1319, 1988

[40] P. F. Bernath, K. W. Hinkle, and J. J. Keady, Science 244, 562, 1989

[41] A. Van Orden and R. J. Saykally, Chem. Rev. 98, 2313-2357, 1998

[42] R. Bouyer, F. Roussel, P. Monchicourt, M. Perdix, and P. Pradel, J. Chem. Phys. 100, 8912-8919, 1994

[43] M. Foltin, O. Echt, P. Scheier, B. Dünser, R. Wörgötter, D. Muigg, S. Matt, and T. D. Märk, J. Chem. Phys. 107, 6246, 1997

[44] B. Boudaiffa, P. Cloutier, D. Hunting, M. A. Huels, and L. Sanche, Science 287, 1658-1660, March 2000

[45] K. Hieda, Int. J. Radiat. Biol. 66, 561, 1994

[46] B. D. Michael et al, in: A. F. Fucarelli and J. D. Zimbrick, eds. Radiation Damage in DNA: Structure/Function Relationships at Early Times, 251-258, Batelle, Columbus, OH, 1995

[47] M.F.A. Harrison in: Methods of Experimental Physics Vol. 7B, pp. 95 ed. W.L. Fite and V. Bedersen, Academic Press, New York, 1968

[48] P. Defrance, F. Brouillard, W. Claeys, and G. Van Wassenhove J. Phys. B: At. Mol. Phys. 14, 103, 1981

[49] A. Müller, K. Tinschert, C. Achenbach, E. Salzborn, and R. Becker Nucl. Instrum. and Methods in Phys. Res. B10/11, 204, 1985

[50] Physica Scripta T 59, (1995)

[51] F. M. Penning, Physica (Amsterdam) 3, 873 (1936)

[52] W. Paul, W. Oberghaus and E. Fischer, Forschungsber. Wirtsch.-Verkehrsminist. Nordrhein-Westfalen 415, 1 (1958)

[53] W. Paul, Rev. Mod. Phys. 62, 531 (1990)

[54] H. Straubel, Naturwissenschaften 18, 506 (1955)

[55] N. Yu, W. Nagourney, and H. Dehmelt J. Appl. Phys. 69 (6), 3779 (1991)

[56] D. Gerlich, and S. Horning, Chem. Rev. 92, 1509 (1992)

[57] K. H. Kingdon, Phys. Rev. 21, 408 (1923)

[58] R. Blümel, Phys. Rev. A. 51, R30 (1995)

[59] D. Gerlich, Physica Scripta T59, 256 (1995)

[60] G. H. Dunn, Physica Scripta T59, 249 (1995)

[61] B. Hochadel, F. Albrecht, M. Grieser, D. Habs, D. Schwalm, E. Szmola, and A. Wolf Nucl. Instr. and Methods in Phys. Res. A 343, 401, 1994

[62] S. P. Møller, NIM A 394, 281 (1997)

[63] T. Tanabe, K. Chida, K. Noda, I. Watanabe, Proceedings of EPAC, Vienna, Austria 2000

[64] C. P. Welsch, A. Schempp, Proceedings of the 2001 Particle Accelerator Conference, Chicago, USA

[65] D. Zajfman, O. Heber, L. Vejby-Christensen, I. Ben-Itzhak, M. Rappaport, R. Fishman, and M. Dahan, Phys. Rev. A 55, 1577 (1997)

[66] H. T. Schmidt, H. Cederquist, J. Jensen, A. Fardi, NIM B 173, 523-527 (2001) Proceedings of the 2001 Particle Accelerator Conference, Chicago, USA

[67] A. Yariv, in Quantum Electronics, 3rd ed. John Wiley, New York, 1989, p. 142.

[68] M. Dahan, R. Fishman, O. Heber, M. Rappaport, N. Altstein, W. J. van der Zande, and D. Zajfman, Rev. Sci. Instrum. 69, 76 (1998)

[69] H. B. Pedersen, D. Strasser, O. Heber, M. L. Rappaport, and D. Zajfman, Phys. Rev. A, 65, 042703 (2001)

[70] SIMION V.6.0 Ion Source Software

[71] H. B. Pedersen, private communication

[72] R. Wester, K. G. Bhushan, N. Altstein, D. Zajfman, O. Heber, and M. L. Rappaport, J. Chem. Phys. 110 (24), 11830 (1999)

[73] K. G. Bhushan, H. B. Pedersen, N. Altstein, O. Heber, M. L. Rappaport, and D. Zajfman, Phys. Rev. A 62, 12504 (2000)

[74] D. Strasser, K. G. Bhushan, H. B. Pedersen, R. Wester, O. Heber, A. Lafosse, M. L. Rappaport, N. Altstein, and D. Zajfman, Phys. Rev. A 61, 60705 (2000)

[75] A. Wolf K. G. Bhushan, I. Ben-Itzhak, N. Altstein, O. Heber, M. L. Rappaport, and D. Zajfman, Phys. Rev. A 59, 267 (1999)

[76] L. Knoll, K. G. Bhushan, N. Altstein, O. Heber, M. L. Rappaport, and D. Zajfman, Phys. Rev. A 60, 1710 (1999)

[77] A. Naaman, K. G. Bhushan, H. B. Pedersen, N. Altstein, O. Heber, M. L. Rappaport, R. Moalem, and D. Zajfman, J. Chem. Phys. 113 (11), 4662 (2000)

[78] S. Ring, H. B. Pedersen, O. Heber, M. L. Rappaport, P. D. Witte, K. G. Bhushan, N. Altstein, Y. Rudich, I. Sagi, and D. Zajfman, Analytical Chemistry 72 (17), 4041 (2000)

[79] H. B. Pedersen, D. Strasser, S. Ring, O. Heber, M. L. Rappaport, Y. Rudich, I. Sagi, and D. Zajfman Phys. Rev. Lett. 87, 055001 (2001)

[80] H. B. Pedersen, D. Strasser, B. Amarant, O. Heber, M. L. Rappaport, and D. Zajfman, Phys. Rev. A 65, 042704 (2001)

[81] M. L. Rappaport, private communication

[82] H. B. Pedersen, private communication

[83] F.-K. Men, B. L. Clothier and J. L. Erskine, Rev. Sci. Instrum. 64 (7) 1883, July 1993

[84] G. Barking, Master Thesis, Heidelberg University, 1996

[85] J. L. Cronin, IEEE PROC., Vol. 128, Pt. I, No. 1, Feb 1981

[86] Technical Bulletin 117, Spectra-Mat Inc.

[87] Landolf-Börnstein, Springer 1959, 6. Auflage II. Teil, 6. Band, Elektrische Eigenschaften, p. 920

[88] W. B. Herrmannsfeldt, Electron Trajectory Program, SLAC-226, Stanford 1979

[89] Solution of **Ma**xwell equations by the **F**inite **I**ntegration **A**lgorithm, CST - Gesellschaft für Computer-Simulationstechnik GmbH

[90] A. Sommerfeld, H. Bethe, Elektronentheorie der Metalle, Springer Verlag, Heidelberg, 1967

[91] P. Kirstein, G. Kino, W. Waters, Space-Charge Flow, Mc Graw-Hill, New York, 1967

[92] J. R. Pierce, J. Appl. Phys. 11, 548, 1940

[93] J . R. Pierce, Theory and design of electron beams, Van Nostrand, New York, 1954

[94] H. Vogel, Gerthsen Physik, 19. Auflage, Springer Verlag, Berlin, 1997

[95] J. L. Cronin, Microwave Journal, September 1979

[96] K. Gunther, Heatwave, private communication

[97] R. Kollath, in: Encyclopedia of Physics, ed. by S. Flügge, Vol XXI, Springer Verlag Berlin, 1956

[98] R. L. Petry, Phys. Rev. 26, 1925

[99] R. Warnecke, J. Phys. Radium 7, 270, 1936

[100] H. Bruining, Philips techn. Rev. 3, 80, 1938

[101] V. S. Fomenko, in: Handbook of Thermionic Properties, G. V. Samsonov, ed., Plenum Press Data Division, New York, 1996

[102] W. Espe, Materialien der UHV-Werkstoffkunde, Bd III, Dt. Verl. der Wiss. , Berlin

[103] S. Rosén, R. Peverall, M. Larsson, A. Le Padellec, J. Semaniak, Å. Larson, C. Strömholm, W.J. van der Zande, H. Danared, and G.H. Dunn, Phys. Rev. A 57, 6, 4462 (1998)

[104] J.B.A. Mitchell and H. Hus, J. Phys. B 18, 547 (1985)

[105] B. Peart, R. Forrest and K. T. Dolder, J. Phys. B: Atom. Molec. Phys. 12, 5, 847 (1979)

[106] L. H. Andersen, M. J. Jensen, H. B. Pedersen, and L. Vejby-Christensen, Phys. Rev. A 58, 4, 2819 (1998)

[107] H.B. Pedersen, N. Djurić, M.L. Jensen, D. Kella, C.P. Safvan. H.T. Schmidt, L. Vejby-Christensen, and L.H. Andersen Phys. Rev. A 60, 4, 2882 (1999)

Acknowledgements